



NATIONAL AND KAPODISTRIAN UNIVERSITY OF ATHENS

MASTER'S THESIS

«Crustal and upper mantle structure of the broader Greek region using receiver functions and seismic anisotropy»

Ioannis N. Fountoulakis

Section of Geophysics-Geothermics
Department of Geology and Geoenvironment
School of Science

Supervisor

Assistant Professor George Kaviris

Examining Committee

Assistant Professor George Kaviris (National and Kapodistrian University of Athens)

Professor Panayotis Papadimitriou (National and Kapodistrian University of Athens)

Research Director George Drakatos (National Observatory of Athens)

Acknowledgements

The present Thesis constitutes the end of a long and constructive journey as master student in the Department of Geology and Geoenvironment. This paragraph is a small tribute to everyone who stood beside me and supported me all this time in order to make this thesis a tangible reality.

In particular I would like to express my appreciation to my supervisor Dr. George Kaviris that made all this possible and showed me the path for my first steps as a scientist, with his wise advices and discussions. A great acknowledgement to Professor Panayotis Papadimitriou for all the beneficial discussions and support the last two years. Special thanks to Dr. George Drakatos for his time and eagerness to be a part of this effort. In addition, I would like to thank Assistant Professor Ioannis Kassaras, Associate Professor Vassiliki Kouskouna, Professor Nicholas Voulgaris and Assistant Professor John Alexopoulos for sharing their expertise and knowledge throughout the Master's lessons.

My gratitude also goes to my colleagues Giannis Spingos and Christos Millas for all the experiences that we shared together these two years (the best is yet to come!). Dr. Andreas Karakonstantis, I really appreciate your guidance and all our fruitful discussions.

Phillip and Kassandra thank you for the motivational support. Your friendship is a valuable gift to me.

Varvara, I am so privileged to have someone like you. Thanks for your patience and attention.

The most special thanks go to my family that gave me their unconditional love and support through all this process. I couldn't have done it without you.

Table of Contents

Abstract	5
Περίληψη	6
Chapter 1: Hellenic system-A useful overview	7
• 1.1 Introduction.....	7
• 1.2 The Hellenic Subduction zone-Aegean Sea.....	8
• 1.3 Slab tear in the Aegean?	9
• 1.4 North Anatolian Fault (NAF).....	10
• 1.5 Kefalonia Transform Fault (KTF)	11
• 1.6 Crustal and Upper Mantle structure.....	12
Chapter 2: Seismic Anisotropy	13
• 2.1 Linear elasticity and wave propagation	13
2.1.1 Wave propagation in anisotropic media.....	16
• 2.2 Seismic anisotropy	18
2.2.1 Introduction	18
2.2.2 Causes of anisotropy.....	19
• 2.3 Where the anisotropy occurs?.....	21
2.3.1 Crustal anisotropy	21
2.3.2 Tectonic settings and SWS interpretation.....	25
• 2.4 Methodologies	29
2.4.1 Introduction	29
2.4.2 Multi-event techniques	30
2.4.3 Single event techniques	30
2.4.4 Comparison of the measurement methods.....	33
• 2.5 SplitLab	34
2.5.1 Ranking Shear-Wave Splitting measurements	36
• 2.6 Results	37
• 2.7 Discussion.....	45
Chapter 3: P-Receiver Functions	53
• 3.1 Introduction	53
• 3.2 Receiver Functions theory	54

3.2.1 Rotation-Deconvolution	54
3.2.2 Depth evaluation	57
• 3.3 Data selection and main processing	59
• 3.4 Results	65
3.4.1 Stations quality	65
3.4.2 Ps arrival times	66
3.4.3 Discussion	77
Conclusions	86
References	87

Abstract

Greece is one of the most geodynamical interesting regions worldwide, with a plethora of available geological features. The present study aims to examine parts of these geodynamical features using the Shear-Wave Splitting phenomenon and the Receiver Functions methodology.

SKS and PKS splitting parameters were determined in the broader Greek region using data from 45 stations belonging to the Hellenic Unified Seismological Network and the Kandilli Observatory and Earthquake Research Institute Network, utilizing teleseismic events that occurred between 2010 and 2017. The shear-wave splitting parameters have been determined using the Minimum Energy Method that was considered the optimal, within the SplitLab software. In general, the obtained results confirm the existence of anisotropic zonation in the Hellenic subduction system, with alternating trench normal and parallel directions. The zonation is interpreted with the existence of upper and lower olivine fabric layering in the subduction zone. Two possible cases of toroidal flow have been identified at the edges of the subduction zone, implying the existence of tears that allow the inflow of asthenospheric material in the mantle wedge. High number of “Null” measurements determined in the KZN and XOR stations indicate a possible anisotropic transition zone between the fore-arc and back-arc areas. SKS and PKS splitting measurements are jointly interpreted, given that they yield similar results in most cases.

Receiver Functions technique was applied in 49 stations of the Hellenic Unified Seismological Network using the same teleseismic events catalogue (2010 - 2017). Iterative and Waterlevel deconvolution was applied in order to remove the source effects from the teleseismic signal. The H-k stacking method was utilized for the Moho depths determination. Iterative deconvolution yielded more reliable results, but the methods were jointly interpreted. The results confirm the existence of a thick crust beneath the Hellenides which is decreasing gradually in the Aegean Sea. Negative Ps conversions were observed locally in the vicinity of the subduction area, especially in the Crete island, sign of possible serpentinization. In addition, the determined from the H-k stacking high V_p/V_s ratios in western Greece indicate partial melting in the broader region.

Περίληψη

Η Ελλάδα αποτελεί μια από τις πιο ενδιαφέρουσες γεωδυναμικά χώρες σε παγκόσμιο επίπεδο, με μια πληθώρα γεωλογικών στοιχείων. Η παρούσα εργασία προσπαθεί να εξετάσει σε βάθος το γεωδυναμικό πλαίσιο του ελλαδικού χώρου, χρησιμοποιώντας για τον σκοπό αυτόν τόσο το φαινόμενο της σχάσης των εγκαρσίων κυμάτων όσο και την μεθοδολογία των συναρτήσεων δέκτη.

Οι παράμετροι σεισμικής ανισοτροπίας των φάσεων SKS και PKS προσδιορίστηκαν στον ευρύτερο ελλαδικό χώρο, χρησιμοποιώντας δεδομένα από 45 σταθμούς του Ενοποιημένου Εθνικού Δικτύου Σεισμογράφων της Ελλάδας και του δικτύου του Παρατηρητηρίου Kandilli της Τουρκίας. Ο κατάλογος των δεδομένων περιελάμβανε τηλεσεισμούς για το χρονικό διάστημα 2010 έως 2017. Οι παράμετροι σχάσης των εγκαρσίων κυμάτων προσδιορίστηκαν με τη μέθοδο της Ελάχιστης Ενέργειας, η οποία θεωρήθηκε η πλέον αξιόπιστη, μέσω του πακέτου λογισμικού Splitlab. Γενικότερα, τα αποτελέσματα της μελέτης σεισμικής ανισοτροπίας επιβεβαιώνουν την ύπαρξη ζωνών ανισοτροπίας στον ελλαδικό χώρο, με εναλλαγή παράλληλων και κάθετων προς την τάφρο διευθύνσεων. Οι ζώνες ερμηνεύονται με την ύπαρξη ενός ανώτερου και ενός κατώτερου στρώματος ολιβίνη στην υποβύθιση. Δύο πιθανές περιπτώσεις τυρβώδους ροής έχουν ανιχνευτεί στα άκρα της ζώνης υποβύθισης, που συνεπάγονται την πιθανή ύπαρξη κενών στην πλάκα που επιτρέπουν στο υλικό να εισέρχεται μέσα στην μανδουακή σφήνα. Υψηλός αριθμός μηδενικών μετρήσεων ανισοτροπίας εντοπίστηκε στους σταθμούς KZN και XOR, οι οποίες ερμηνεύθηκαν με την πιθανή ύπαρξη μεταβατικής ζώνης μεταξύ της εμπροσθοτάφρου και της οπισθοτάφρου. Οι μετρήσεις των φάσεων SKS και PKS ερμηνεύονται από κοινού, δεδομένου ότι παρέχουν παρόμοιες μετρήσεις στις περισσότερες περιπτώσεις.

Η τεχνική των συναρτήσεων δέκτη εφαρμόστηκε σε 49 σταθμούς του Ενοποιημένου Εθνικού Δικτύου Σεισμογράφων με ανάλυση τηλεσεισμών για το χρονικό διάστημα 2010 έως 2017. Δύο διαφορετικές μεθοδολογίες αποσυνέλιξης (Iterative, Waterlevel) εφαρμόστηκαν για την αφαίρεση της επίδρασης της πηγής και του σταθμού στο σεισμικό σήμα. Επίσης, εφαρμόστηκε η μεθοδολογία H-k για τον προσδιορισμό του βάθους της ασυνέχειας Moho κάτω από κάθε σταθμό μελέτης. Τα πιο αξιόπιστα αποτελέσματα προέκυψαν από την επαναληπτική αποσυνέλιξη (Iterative), αλλά και οι δύο μεθοδολογίες παρείχαν αξιόπιστα αποτελέσματα. Τα αποτελέσματα επιβεβαιώνουν την ύπαρξη μεγάλου πάχους φλοιού κάτω από τις Ελληνίδες, το οποίο μειώνεται σταδιακά μέχρι το Αιγαίο Πέλαγος. Αρνητικοί παλμοί φάσεων Ps παρατηρήθηκαν τοπικά κοντά στην ζώνη υποβύθισης και κυρίως σε σταθμούς στην Κρήτη. Επιπλέον, οι παρατηρούμενοι από την μέθοδο H-k λόγοι V_p/V_s προσδιορίζουν την πιθανή ύπαρξη μερικής τήξης σε τμήμα της δυτικής Ελλάδος.

Chapter 1: Hellenic system-A useful overview

1.1 Introduction

The area of Greece constitutes a remarkable physical and geological laboratory, with different and at the same time complex tectonic settings. The main geomorphological features of Greece and adjacent areas have been identified decades ago (e.g. Agarwal et al. 1976; Makropoulos and Burton 1984) and they include (1) the Mediterranean Ridge which extends from the Ionian Sea to Cyprus, (2) the Hellenic Trench (or Trough), (3) the Hellenic volcanic arc and (4) the Northern Aegean Sea.

The active kinematics of the Hellenic system, which is a part of the Alpine-Himalayan Mountain Belt, is dominated by two phenomena, the retreat of the subducting African plate and the westward movement of the Anatolian plate along the north Anatolian fault (NAF) (e.g. Pichon and Angelier 1979; Jolivet 2001). Essentially, the right-lateral NAF bounds the Anatolian and the prominent Aegean microplate (e.g. McKenzie 1972). The Aegean-Western Anatolia region is undergoing extensional deformation, given the existence of normal faults and the corresponding focal mechanisms (e.g. Papadimitriou and Sykes 2001; Kiratzi and Louvari 2003; Karakostas et al. 2003; Voulgaris et al. 2004; Kreemer et al. 2004; Kassaras and Kapetanidis 2018; Papadimitriou et al. 2018).

In addition, the Hellenic subduction system can be distinguished into two segments with different subduction rates. The latter are separated from each other, close to the island of Kefalonia, in a region that is dominated by another important tectonic feature, the Kefalonia Transform Zone (KTZ). These segments are often characterized as northern and southern Hellenides (e.g. Royden and Papanikolaou 2011). The basic features of the Greek modern tectonics are presented in Figure 1.

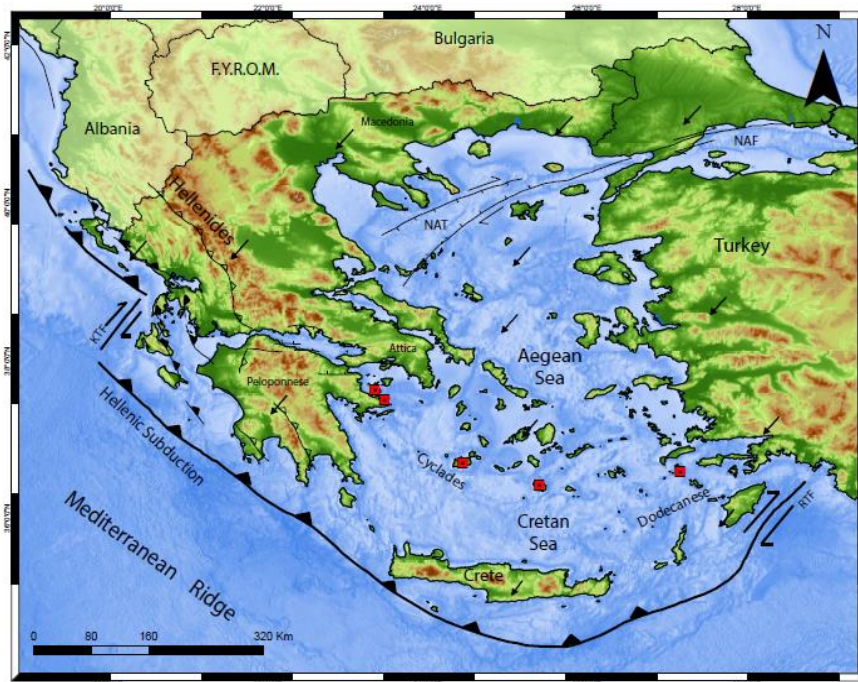


Figure 1: Schematic map of the tectonic settings of the broader Greek region based on Royden and Papanikolaou (2011). Black arrows represent the overall direction of the Aegean and Anatolian plate movement modeled in the absolute reference frame system GSRM v2.1 (Kreemer et al. 2014). Red squares indicate the most important centers in the volcanic arc.

1.2 The Hellenic Subduction zone-Aegean Sea

The well-defined subduction of the African plate under the Crete trench is highlighted by the existence of active seismic and volcanic zones that come as a direct consequence of the subduction mechanism. It is worth noting that a period of intense activity occurred in the Santorini region during 2011-2012 (Papadimitriou et al. 2015). In general, Greece is characterized by very high seismicity (Kouskouna and Sakkas 2013; Stucchi et al. 2013). The subducting plate is characterized by a Benioff zone that reaches ~150 km depth (Papazachos et al., 2000), with an angle of subduction of about 16° and a down-dip extension in the slab (Papazachos et al. 2005). Direct consequence is the shallow and intermediate-depth seismicity that reaches approximately 180 km in the Central Aegean (<http://dggs1.geol.uoa.gr/>). The slab geometry can be emerged through the seismicity but also through seismic tomography studies. Tomographic studies (e.g. Drakatos and Drakopoulos 1991; Piromallo and Morelli 2003; Salaün et al. 2012; Karakonstantis 2017) reveal a fast velocity (or cold) body that can be interpreted as the Hellenic subducting slab (Fig. 2).

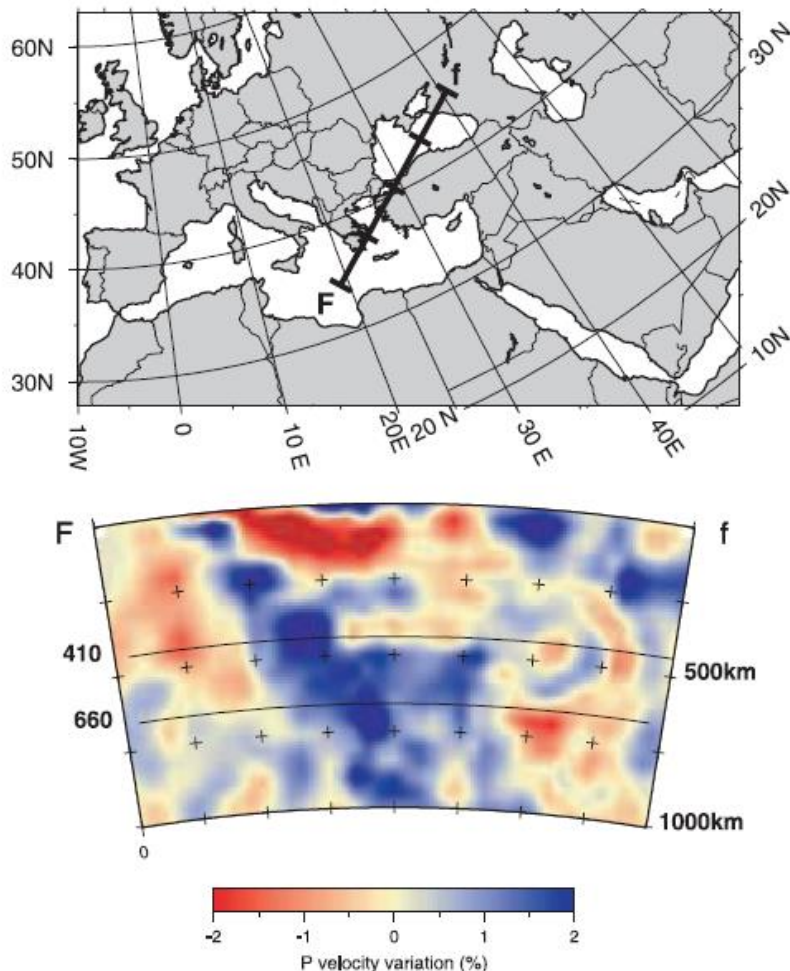


Figure 2: Tomographic section, including the Hellenic subduction zone, after Piromallo and Morelli (2003) revealing a body with fast velocities.

According to Royden and Papanikolaou (2011) the formation of the Hellenic arc close to its current shape was initiated approximately in the Jurassic-Late Cretaceous. In this period NE dipping subduction along the Hellenic arc was dominant, producing a stacking of series of thrusts that have been tectonically emplaced in the continent's interior (e.g. Faccenna et al. 2003). A major tectonic event during the Eocene was the subduction of the Pindos Ocean beneath the arc, as evidenced by ophiolitic and sedimentary formations (Papanikolaou 2009; Royden and Papanikolaou 2011). Following, in Oligocene time, the external carbonate platform of Hellenides subducted, with some exception, such as the Arna unit and Mani basement that have been exposed in the surface by tectonic windows (e.g. Papanikolaou 2009). The advance of the subduction in the southern part of the Hellenides resulted to the entrance of the Ionian oceanic lithosphere in the subduction.

The formation of the Aegean sea in the Early Oligocene is a direct effect of the retreat of the subducting African slab beneath Eurasia (Jolivet and Brun 2010). In addition, this episode led to the exhumation-creation of the high pressure (HP) and low temperature (LT) Cycladic metamorphic unit of Blueschists (e.g. Jolivet et al. 2003; Jolivet and Brun 2010).

Geodetic studies in the Aegean region provide valuable information regarding the plate kinematics and the existing extension in the back-arc. GPS studies (e.g. Reilinger et al. 2006; Hollenstein et al. 2008) indicate the occurrence of a counterclockwise rotation in the Eastern Mediterranean relative to Eurasia. The values of the velocity field increase towards the Crete trench, in a reference frame fixed to Eurasia, implying the occurrence of extension in the Aegean system. The convergence rate in the southern part of the subduction zone reaches ~35 mm/yr.

1.3 Slab tear in the Aegean?

Slab tearing is a well-documented process that involves the creation of gaps in the subducting lithosphere and causes localized mantle upwelling. These gaps lead to the development of segmented subduction zones with a possible horizontal movement, in the case where differential rollback velocity exists (Rosenbaum et al. 2008 and references within). Slab tearing is also present in the Hellenic trench (Pichon and Angelier 1979; Royden and Papanikolaou 2011; Jolivet et al. 2015; Bocchini et al. 2018). Govers and Wortel (2005) connected the gaps with the existence of STEP faults (Subduction-Transform-Edge-Propagator or tear fault) that bound the Hellenic trench, to the west (Kefalonia Fault Zone) and to the east (eastern Aegean region). These faults (STEP faults) are strike-slip transform faults that produce tearing in the subducted plate lithosphere (Nijholt and Govers 2015).

The existence of slab tearing in the eastern Aegean forms two segments that constitute the Aegean and the Cyprus trenches. Tomographic models verify the tear in the broader region (e.g. Piromallo and Morelli 2003; Berk Biryol et al. 2011; Salaün et al. 2012), while a NE-SW STEP model geometry has been suggested for the Pliny and Strabo trenches (Govers and Wortel 2005; Berk Biryol et al. 2011; Govers and Fichtner 2016). The suggestion is under dispute because the slab below western Turkey is considered to be still connected at depth with the subducted slab differing from a classic STEP model (Jolivet et al. 2013). Bocchini et al. (2018) concluded from a seismicity point of view that there is a clear NW dipping subducting slab in the area of Rhodes and rejects the NE-SW STEP fault model in the broader region (Fig. 3).

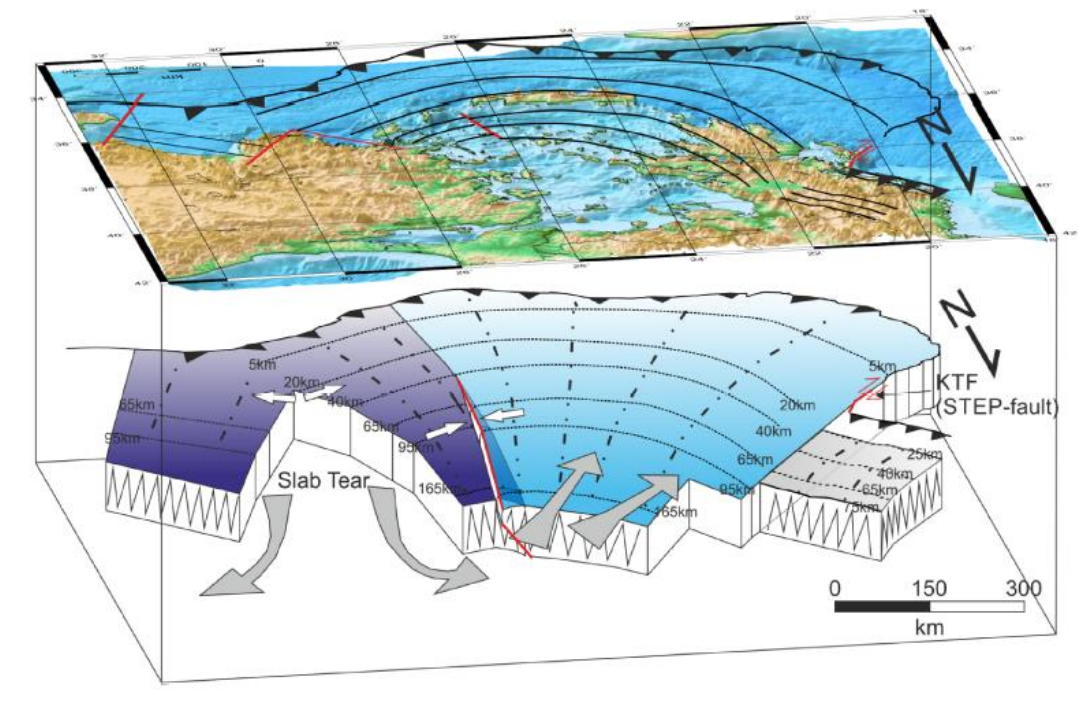


Figure 3: 3-D sketch summarizing the findings of Bocchini et al. (2018). The light blue represents the western segment of the subduction zone and the dark blue the eastern. The white motions indicate relative motion and the grey arrows the mantle flow. The KTF and the Slab tear in the eastern part is also presented.

1.4 North Anatolian Fault (NAF)

The most characteristic geodynamic feature in the Aegean-Anatolian region is the North Anatolian Fault (NAF). The NAF constitutes the upper boundary of the Anatolian plate and is characterized by a right lateral strike-slip motion (McKenzie 1972; Jackson and McKenzie 1984; Şengör et al. 2005). The kinematic role of the NAF is very important given that it accommodates the westward motion of the Anatolian plate according to geodetic data. In addition, the observed velocity is increasing towards the Hellenic trench relative to stable Eurasia (e.g. Reilinger et al. 2006; Hollenstein et al. 2008). The NAF enters the region of the North Aegean approximately at the time of the Messinian Salinity Crisis (Armijo et al. 1999) and since then it is the center of intense tectonic activity. In the Aegean the NAF is imprinted in the North Aegean Trough (Papanikolaou et al. 2002). There is an extensive bibliographical support regarding the existence of a displacement transportation from the NAF to the west part of the Hellenic trench with the so-called Center Hellenic Shear Zone (CHSZ), a specific shear zone that extends from central Turkey to the Ionian Sea (Papanikolaou and Royden 2007; Royden and Papanikolaou 2011).

1.5 Kefalonia Transform Fault (KTF)

The Kefalonia Transform Fault contains two major fault segments, the Lefkada and the Kefalonia segments. These segments are characterized by dextral strike-slip motion (Louvari et al. 1999,). The KTF also separates two geodynamical phenomena, the continental collision to the north (Apulian microplate-Hellenic foreland) and the oceanic subduction to the south. The KTF slip-rate varies from 7 to 30 mm/yr (e.g. Hollenstein et al. 2008). Suckale et al. (2009) suggests that the KTF is a vertical tear along the oceanic and continental lithosphere. In addition, Govers and Wortel (2005) characterize the KTF as a STEP-fault. The KTF has caused a significant number of earthquakes in the Central Ionian Islands (e.g. Kouskouna et al. 1993; Tselentis et al. 1997; Tzanis et al. 2000; Papadimitriou 2002; Karakostas et al. 2015)

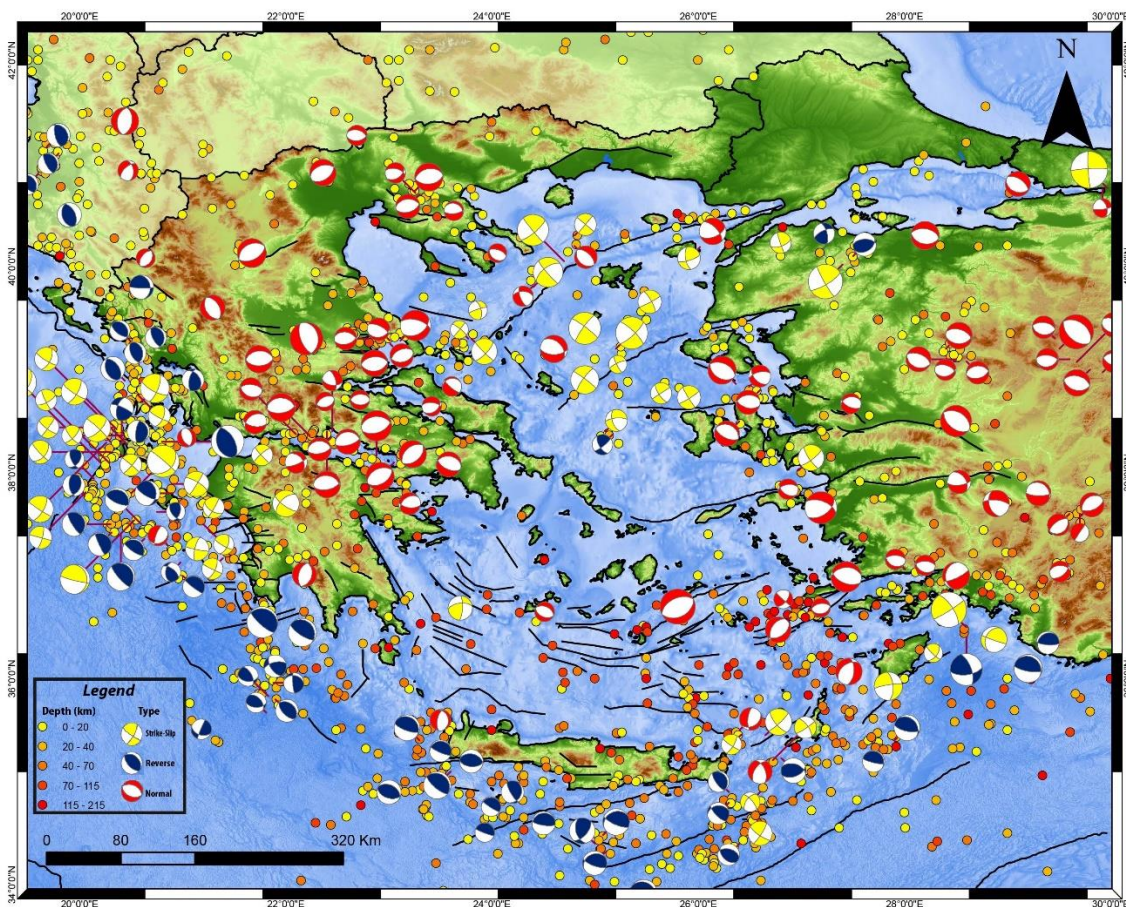


Figure 4: Focal mechanisms spatial distribution by the Seismological Laboratory of the National and Kapodistrian University of Athens (<http://www.geophysics.geol.uoa.gr>) and by Kiratzi and Louvari (2003) and distribution of epicenters of events with $M_w > 5.5$ from Makropoulos et al. (2012).

1.6 Crustal and Upper Mantle structure

The crustal and upper mantle structure can be approached by various geophysical methodologies, such as active/passive source reflection and refraction data, body and surface wave tomographic studies, gravity surveys etc. Despite of the accountable bibliographical references in this subject, the detailed characteristics, including geometry, of the mantle and the crustal structure is an open question.

There is a plethora of available and published crustal models that are based on different types of geophysical methods. More specifically for the Greek region, the crustal thickness for the thin continental domain is approximately 25 km for the Aegean Sea and about 15 km for the Cretan sea. For the thicker part (northern Hellenides) the crustal thickness can reach 50 km (Faccenna et al. 2014 and references within). Examining in more detail the Greek region, the observed thinning in the Aegean Sea is attributed to the extensional regime in the back arc area (Karagianni et al. 2005). More specifically, Karagianni et al. (2005) observed from inversion of Rayleigh waves that the crustal thickness in the Aegean Sea is less than 30 km and in the Hellenides mountains is approximately 40-46 km. Similar results are obtained by the Pn anisotropic tomography. Mutlu and Karabulut (2011) estimated the Moho depths for the Aegean Sea from 28 to 32 km, with a relative thicker crust in the northern Aegean (Fig. 5). In the same study the authors suggested that the Aegean sea is deforming coherently and the driving force for the observed kinematic behavior is the mantle flow, taking into account GPS, Pn anisotropy and SKS directions.

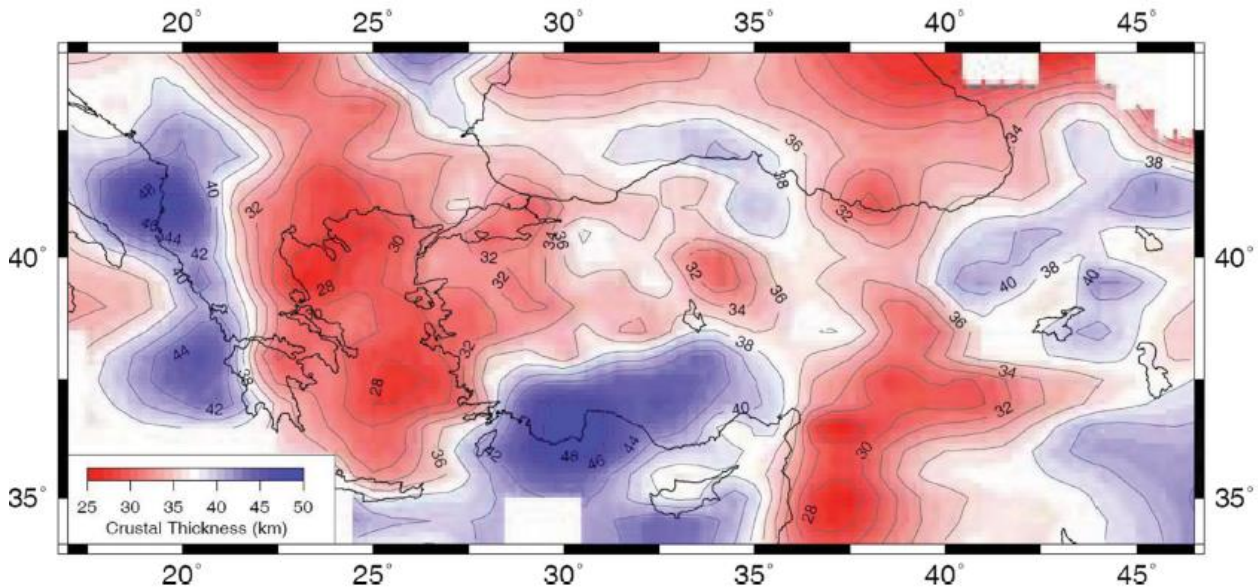


Figure 5: Crustal thickness map from the broader Greek and Turkey region by Mutlu and Karabulut (2011).

Chapter 2: Seismic Anisotropy

2.1 Linear elasticity and wave propagation

The most vital part in the field of Seismology is the analysis of ground motions produced by energy sources in the Earth's interior. Ground motion is transient and the medium returns to its initial state, except of the energy source vicinity. Vibrations involve small elastic deformations in response to applied stress. In order to identify, with mathematical equations, the relationship between deformation and stress, the elasticity theory is applied. Basic principles of this theory, related to the present thesis applications, are following described. This paragraph is basically based on Lay & Wallace (1995), Shearer (1999) and Stein & Wysession (2003).

The development of the elasticity theory follows a solid mechanics approach. The most useful concept in the study of solids is that of a continuum medium, in which matter is viewed as being continuously distributed in space. Simple laws of physics can be applied to this type of macroscopic view, allowing useful explanations to seismological phenomena. Whenever forces are applied to a continuum medium, every point of the body is influenced. These forces can be either internal (body forces) or external (contact forces). Body forces are proportional to the volume of the material and contact forces depend on the surface area. For a body on which external forces are applied, the internal forces tend to resist to the deformation. As a result, the body will return to its initial shape and volume, once the application of external forces is terminated. The medium is characterized as elastic, in the case where the recovery to its initial shape, when external forces are no longer applied, is perfect. In order to thoroughly describe the elasticity theory, two important quantities are introduced, the stress and the strain.

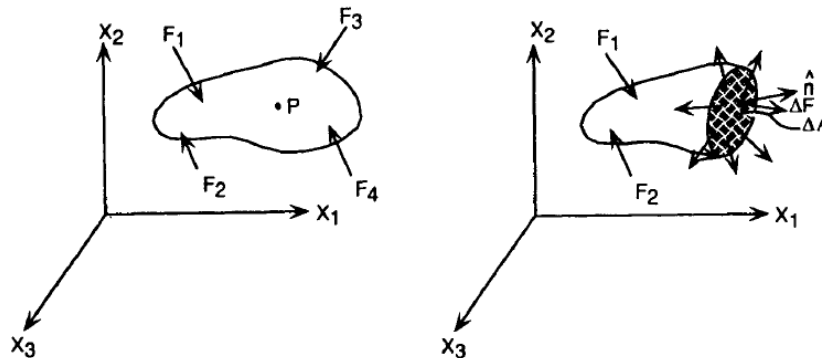


Figure 6: Continuum medium acted upon with external forces (Left). Theoretical plane that passes through an internal point P with normal n (Right) and internal forces that balance medium's equilibrium (Lay and Wallace, 1995).

The state of stress has physical dimensions of force per unit area and corresponds to action of part of the medium upon the other. For example there is a specific point P (Fig. 6), on a plane that passed through the medium. Dividing the plane into area elements, it is possible to imagine an infinitesimal small cube, each side having an infinitesimal small surface δS , with a small force \vec{F} acting on the element. The acting traction \vec{T} can be decomposed into its stress components, normal σ_n and tangential σ_h to this surface (Fig. 7). Thus, we define the stress vector or the traction vector:

$$T(n) = \lim_{\delta S \rightarrow 0} \frac{\delta F}{\delta S}$$

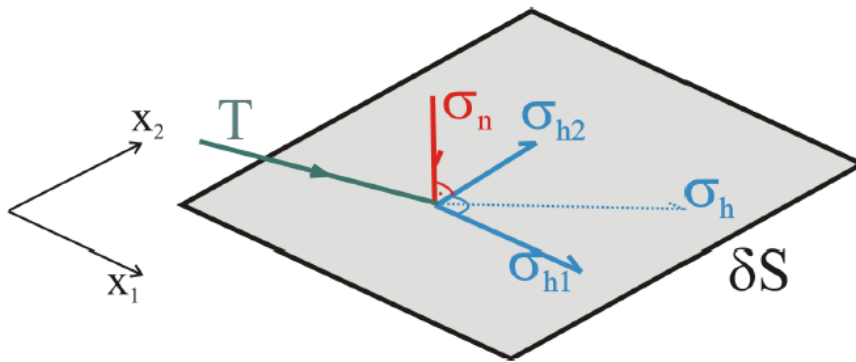


Figure 7: Components of stress acting on a surface. Any traction can be divided into its components normal and tangential to the surface (Wüstefeld 2007).

Stress is described by σ_{ij} , with the first index corresponding to the direction of the normal to the plane being acted on by the force and the second one indicating the direction of the force. Thus, nine terms are required in order to completely represent the internal force distribution. The components with the same indices are normal stresses, while the different indices imply shear stresses. If the body is in equilibrium, the sum of the forces that are applied on it, and the sum of the moments, must be zero. Keeping that in mind, a symmetry is expressed:

$$\sigma_{ij} = \sigma_{ji}$$

Thus, a stress tensor σ_{ij} is defined that describes the state of stress at any point P of this medium with six independent parameters due to that symmetry:

$$\sigma_{ij} = \begin{pmatrix} \sigma_{11} & \sigma_{12} & \sigma_{13} \\ \sigma_{21} & \sigma_{22} & \sigma_{23} \\ \sigma_{31} & \sigma_{32} & \sigma_{33} \end{pmatrix} = \begin{pmatrix} \sigma_{11} & \sigma_{12} & \sigma_{13} \\ \sigma_{12} & \sigma_{22} & \sigma_{23} \\ \sigma_{13} & \sigma_{32} & \sigma_{33} \end{pmatrix}, \quad \text{with } i, j=1, 2, 3$$

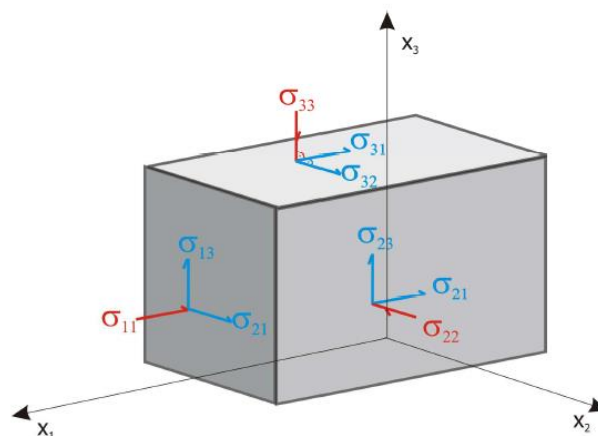


Figure 8: Complete representation of stresses acting on a block (Wüstefeld 2007).

The elastic medium deforms, when it undergoes a stress field. This deformation is called strain, ε , and can also be described by a three-dimensional strain tensor with the same type of symmetry, as described in stress:

$$\varepsilon_{ij} = \varepsilon_{ji}$$

$$\varepsilon_{ij} = \begin{pmatrix} \varepsilon_{11} & \varepsilon_{12} & \varepsilon_{13} \\ \varepsilon_{21} & \varepsilon_{22} & \varepsilon_{23} \\ \varepsilon_{31} & \varepsilon_{32} & \varepsilon_{33} \end{pmatrix} = \begin{pmatrix} \varepsilon_{11} & \varepsilon_{12} & \varepsilon_{13} \\ \varepsilon_{12} & \varepsilon_{22} & \varepsilon_{23} \\ \varepsilon_{13} & \varepsilon_{32} & \varepsilon_{33} \end{pmatrix}, \quad \text{with } i, j = 1, 2, 3$$

The mathematical connection between stress and strain originates from Hooke's law, according to which small magnitude and short duration stresses are characterized by linear proportionality between stress and strain. In its general form, it can be written as:

$$\sigma_{ij} = C_{ijkl} \varepsilon_{kl} \quad \text{with } i, j, k, l = 1, 2, 3$$

The constants C_{ijkl} are called *elastic moduli* and they define the properties of the medium. It is a third-order tensor with 81 terms that links the applied stress to the resulting deformation of the medium. Taking into account the above-mentioned symmetry considerations, the number of independent parameters are reduced from 81 to 36 ($C_{ijkl} = C_{jikl} = C_{ijlk} = C_{jilk}$). An additional symmetry relation ($C_{ijkl} = C_{klij}$), as consideration of a strain energy density function, further reduces the independent parameters to 21. If these 21 parameters vary with direction, the medium is called anisotropic. The medium is characterized as isotropic if its properties are not dependent on the direction. For an isotropic medium, the elastic moduli have only two independent parameters, the Lamé constants (λ and μ):

$$C_{ijkl} = \lambda \delta_{ij} \delta_{kl} + \mu (\delta_{ik} \delta_{jl} + \delta_{il} \delta_{jk}),$$

The Kronecker delta function (δ_{ij}) is used. The Kronecker delta is a function of two variables, usually non-negative integers. The function is 1 if the variables are equal, and 0 in any other case:

$$\delta_{ij} = \begin{cases} 0 & \text{if } i \neq j \\ 1 & \text{if } i = j \end{cases}$$

It is worth noting that the constant μ , i.e. the *shear modulus*, describes the resistance to shear stress. The second Lamé constant, λ , is most significant in combination with other terms defining another five elastic moduli that have physical attributes in terms of λ and μ , including the E (Young's moduli), k (bulk modulus), and ν (Poisson ratio). In terms of stress and strain the Hooke's law can be written using the Lamé constants as:

$$\varepsilon_{ij} = \frac{-\lambda \delta_{ij}}{2\mu(3\lambda + 2\mu)} \sigma_{kk} + \frac{1}{2\mu} \sigma_{ij}$$

Following these considerations, C_{ijkl} can be represented by:

$$C_{mn} = \begin{pmatrix} C_{1111} & C_{1122} & C_{1133} & C_{1123} & C_{1113} & C_{1112} \\ C_{2211} & C_{2222} & C_{2233} & C_{2223} & C_{2213} & C_{2212} \\ C_{3311} & C_{3322} & C_{3333} & C_{3323} & C_{3313} & C_{3312} \\ C_{2311} & C_{2322} & C_{2333} & C_{2323} & C_{2313} & C_{2312} \\ C_{1311} & C_{1322} & C_{1333} & C_{1323} & C_{1313} & C_{1312} \\ C_{1211} & C_{1222} & C_{1233} & C_{1223} & C_{1213} & C_{1212} \end{pmatrix}$$

For isotropic material it can be also represented using the Lamé constants:

$$C_{mn} = \begin{pmatrix} \lambda + 2\mu & \lambda & \lambda & 0 & 0 & 0 \\ \lambda & \lambda + 2\mu & \lambda & 0 & 0 & 0 \\ \lambda & \lambda & \lambda + 2\mu & 0 & 0 & 0 \\ 0 & 0 & 0 & \mu & 0 & 0 \\ 0 & 0 & 0 & 0 & \mu & 0 \\ 0 & 0 & 0 & 0 & 0 & \mu \end{pmatrix}$$

2.1.1 Wave propagation in anisotropic media

Although isotropy is considered as a satisfactory approximation to study the earth's interior, in reality earth presents significantly anisotropic behavior. Let us consider a wavefront that expands from a point source in an anisotropic homogenous medium. The wavefront is not spherical, given that velocity varies with the angle of the ray. This means that the ray is not perpendicular to the wavefront. The ray represents the group velocity of the wave, whereas the V is the phase velocity of the wavefront in a perpendicular direction to the wavefront. The phase and the group velocity are different for a wave that propagates through an anisotropic medium (Fig. 9).

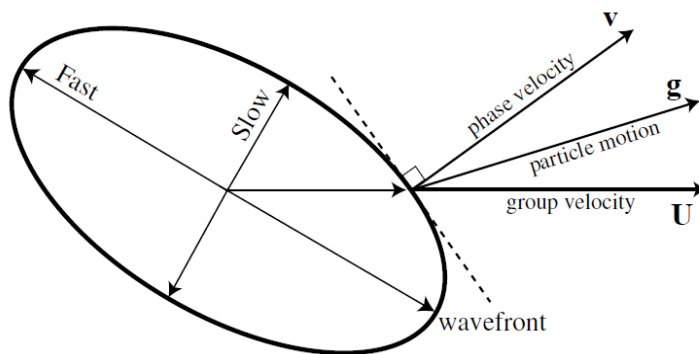


Figure 9: Wavefront produced by a point source in an anisotropic material. The phase velocity, the group velocity and the particle motion point to a different direction for a quasi-compressional wave (except along a symmetry plane where they coincide) (Shearer 1999).

The independent elastic constants in the C_{ijkl} matrix, as previously mentioned, are 21 in most cases. This number can be reduced, if additional symmetries exist. For example, crystals with orthorhombic symmetry have nine elastic constants or with hexagonal five constants.

Given that $e_{kl} = \frac{1}{2}(\theta_k u_l + \theta_l u_k)$, the general equation that connects stress and strain can be written as:

$$\sigma_{ij} = C_{ijkl} \theta_l u_k \quad (2.1)$$

Using the expression (2.1) the momentum equation is changing form:

$$\rho \ddot{u}_i = (\nabla \cdot \sigma)_i = \theta_j \sigma_{ij} = \theta_j (C_{ijkl} \theta_l u_k) = C_{ijkl} \theta_j \theta_l u_k \quad (2.2),$$

where we assume that C_{ijkl} is constant within a homogenous layer.

It is also assumed that there is a plane-wave solution for the displacement u of the form:

$$u = g e^{-i\omega(t-sX)} \quad (2.3),$$

where:

s : slowness vector (k/ω).

X : the position vector

g : polarization vector

Substituting (2.3) into (2.2):

$$\rho g_i = g_k C_{ijkl} s_j s_l \quad (2.4)$$

Defining the density-normalized elastic tensor and $s = \frac{\hat{s}}{c}$, where \hat{s} the unit slowness vector, c the phase velocity and ρ the density:

$$\Gamma_{ijkl} = \frac{C_{ijkl}}{\rho}$$

$$(\Gamma_{ijkl} \hat{s}_j \hat{s}_l - c^2 \delta_{ik}) g_k = 0$$

Additionally:

$$M_{ik} = \Gamma_{ijkl} \hat{s}_j \hat{s}_l$$

$$(M_{ik} - c^2 \delta_{ik}) g_k = 0 \quad (2.5)$$

The equation (2.5) is the eigenvalue equation, for which are three solutions for c^2 in a given direction \hat{s} exist. In anisotropic media, there are three separate second-order equations, one for P waves and two types of S waves (SV and SH). For an anisotropic medium there are, for any direction, three eigenvalues. The eigenvectors specify the polarization of the wave, namely quasi-P, fast and slow S-waves.

2.2 Seismic anisotropy

2.2.1 Introduction

Anisotropy is the dependence of a physical quantity by the direction, which implies different properties in different directions. In consequence, seismic anisotropy is a term used in seismology to describe the directional dependence of the velocity of seismic waves in a medium (rock) within the Earth. For mathematical and modelling convenience the earth is often assumed to be isotropic. Even in the cases where the results of these assumptions are adequate, that does not mean that phenomena such as seismic anisotropy should be ignored. The tradeoff between anisotropic and isotropic structures is complicated and should be carefully examined, given that anisotropic structures can have characteristics, such as travel times, that can be similar to the ones of different types of isotropic structures. For example, a solid layer composed by different isotropic layers can behave as an anisotropic solid, or an anisotropic medium can easily be modeled like a stack of distinct isotropic layers. For this reason, the interpretation of seismic anisotropy should be accompanied by a plurality of seismological evidences.

The early evidence of the seismic anisotropy phenomenon was implied by the observations of discrepancies between dispersion of Love and Rayleigh waves (Anderson 1961) and by azimuthal dependence of oceanic Pn velocities (Hess 1964). Following these first publications and with the publication of a great number of studies, the presence of seismic anisotropy was established. The most obvious exhibitions of seismic anisotropy is (Anderson 1989):

- Radial anisotropy: Apparent discrepancies between Love and Rayleigh waves.
- Azimuthal anisotropy: Azimuth dependence of the arrival times or velocities of seismic waves at a given distance of an event.
- Shear wave birefringence: Two S-waves that arrive in different times at the station, with different polarization directions.

The “Shear wave birefringence” effect is the optical analog of the seismological “Shear wave splitting”. The study of this phenomenon was first investigated in connection with the light, given that in the early scientific years there was no distinction between the light and the seismic waves. Nowadays, it has been established that when a shear wave propagates through an anisotropic medium, the component polarized parallel to the fast direction begins to lead the orthogonal component (Fig. 10) (Savage 1999). This phenomenon is termed as “Shear Wave Splitting” (from now on SWS) and the routine SWS measurements yield estimations of the polarization of the fast wave (φ) and of the time delay (δt) between the fast and the slow waves.

In the present master thesis, we will focus on the upper mantle anisotropy as it will be examined in detail in the next chapters. The presence-validity of the anisotropy in the upper mantle is not simple, taking into account that many seismological topics depend on it, such as the thickness of the oceanic lithosphere and the deep penetrations of the slabs.

Shear wave splitting in anisotropic media

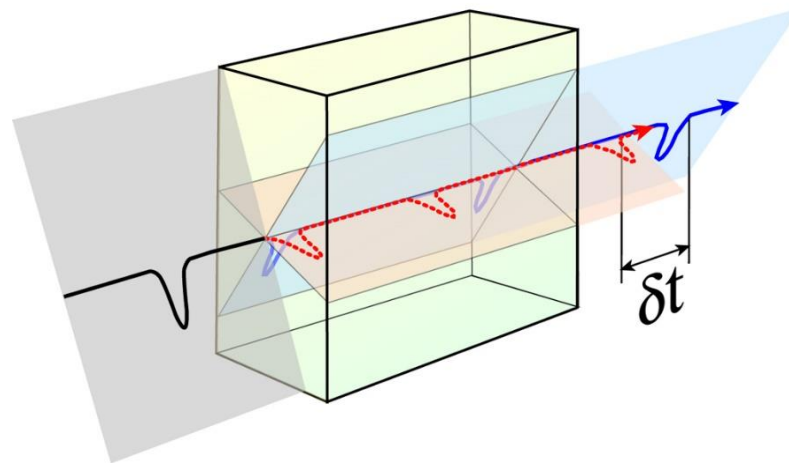


Figure 10: Shear wave splitting phenomenon in an anisotropic medium (Courtesy of Ed. Garnero).

2.2.2 Causes of anisotropy

Among the possible causes of anisotropy, only few of them have dominated the international bibliography. Backus (1962) suggested that the effect of anisotropy can be created by “stacking” isotropic layers with different elastic constants by observing seismic anisotropy in P wave velocities. However, this interpretation has not fully explained the anisotropic phenomena in the crust and the mantle. The two basic theories for the seismic anisotropy phenomenon in the lithosphere and in the asthenosphere are the crystalline anisotropy (e.g. Nicolas and Christensen 1987) and the fluid-melt filled cracks (e.g. Crampin and Chastin 2003).

Crystalline anisotropy or Lattice Preferred Orientation (LPO) or Crystal Preferred Orientation (CPO), is the orientation of the initially random oriented minerals under certain temperature and pressure conditions (e.g. Nicolas and Christensen 1987; Tommasi et al. 1999). Generally, minerals can be described by elastic tensors. In order to simplify their geometry we accept specific symmetry systems. All crystals belong to one of the nine possible symmetry systems but in seismic anisotropy studies orthorhombic and hexagonal symmetry are mostly considered, due to observations of these systems in mantle-derived rocks. The Olivine and Orthopyroxene belong to the orthorhombic category with nine independent elastic constants to completely define their elastic properties. The fastest compressional wave velocity direction in Olivine and Orthopyroxene is the crystallographic [100] or a and the slowest [010] or b (Fig. 11) (Nicolas and Christensen 1987).

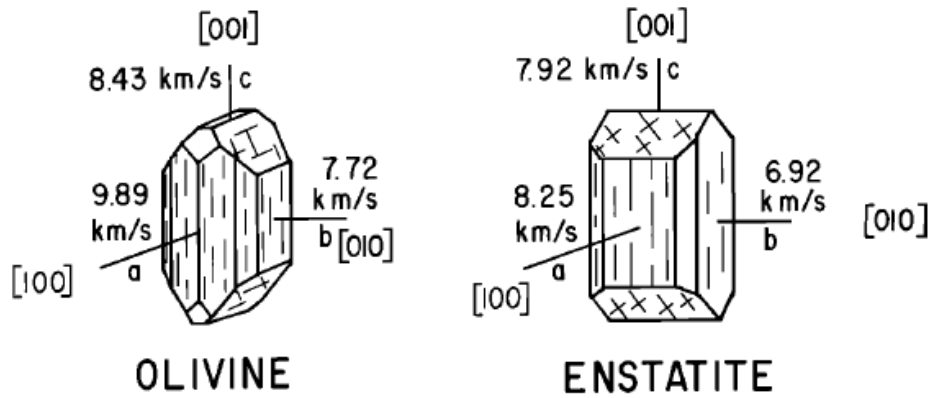


Figure 11: Compressional wave velocities in km/sec in the crystallographic axes of olivine and enstatite (Nicolas and Christensen 1987).

There is a clear but complicated correlation between the deformation and the LPO (e.g. Savage 1999; Tommasi et al. 1999) that has occupied the scientific community. Two deformation types are important regarding the upper mantle conditions, where the Olivine is the abundant mineral and the LPO is the probable cause of anisotropy (e.g. Mainprice 2007), the diffusion creep and the dislocation creep. Diffusion creep is solid-stated diffusion between grain boundaries or across a crystal lattice, whereas dislocation creep is the motion of crystalline dislocation within grains. The latter causes preferred mineral orientation and therefore anisotropy. Dislocation creep is require in order to produce LPO, whereas diffusion creep wipes out any pre-existing petrological fabric (and the LPO of course) (Karato and Wu 1993). The connection between LPO and the deformation (changes in stress and strain) will be explained in detail in the next chapter.

Another theory that attempts to explain the seismic anisotropy phenomenon is the Shape-Preferred Orientation (SPO). The presence of this phenomenon in the lower crust and in the lowermost mantle is thought to be a significant cause of anisotropy. It results from the preferred orientation of structures such us faults, microfractures or compositional lamellae, making the otherwise isotropic medium to behave as anisotropic for wavelengths significantly larger than the spacing interval of the structure (Backus 1962). Especially in the lowermost mantle, SPO involves a great variety of structures from tubular inclusions to sheets and to anastomosing (Moore et al. 2004) (Fig. 12).

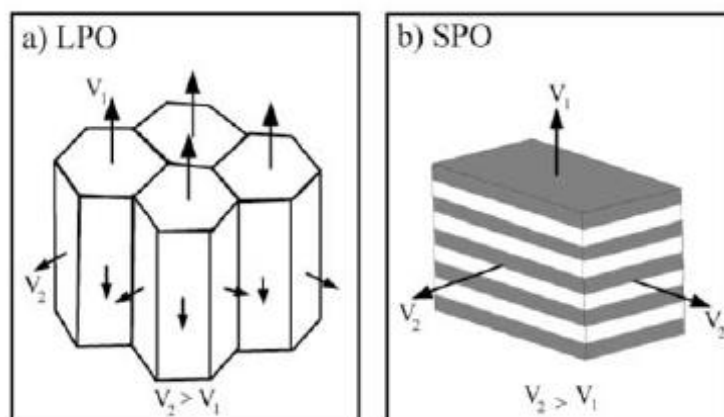


Figure 12: Different origins of anisotropy (Moore et al. 2004).

2.3 Where the anisotropy occurs?

2.3.1 Crustal anisotropy

The majority of the crustal anisotropy is caused by cracks and microcracks in the upper 10-15 km of the crust (Kaneshima et al. 1988). These microfractures are generally randomly oriented but they tend to close perpendicular to the maximum principal stress direction σ_1 . The fast S-wave polarization plane (φ) is considered to be parallel to the maximum horizontal stress component σ_H (e.g. Crampin and Chastin 2003). The resulting anisotropy from periodic thin layers is called PTL (with a vertical symmetry axis) (e.g. Helbig 1984) and the anisotropy in the upper crust that is attributed to fluid-filled cracks, aligned according to regional stress, EDA (e.g. Crampin 1978). The average δt values range between 0.04 s and 0.20 s, but there are case in the vicinity of active faults where time delays of ~ 0.5 s have been identified (Savage et al. 1990). Due to the fact that pressure is increasing with the depth, the microcracks are closing (pressures greater than 200-300 MPa and depths >15 km) (e.g. Kern 1990).

Lower crust anisotropy is dominated by finely layered horizontal strata due to the interactions of reflections and transmissions through thin layers. Time delay values up to 0.1 s-0.3 s may be explained by the lower crust anisotropy that follows hexagonal symmetry (Savage 1998). Thus, these delay times are too small to be examined in the SKS study cases, where δt is quite larger, and they are usually ignored. A significant fact is that crustal anisotropy is used as a forecasting tool for ruptures and volcanic eruptions (e.g. Bianco et al. 1999; Crampin et al. 1999).

2.3.1.1 Upper mantle anisotropy

The anisotropy in the upper mantle is connected with the presence of minerals. Thus, it is important to have a solid knowledge of the petrological state in the upper mantle. Basic source of information about this topic is the study by Mainprice (2007). The upper mantle (until 410 km depth) is mainly composed by highly anisotropic phases: olivine, enstatite (orthopyroxene) and diopside (clinopyroxene). Another volumetrically important phase, yet with isotropic behavior, is garnet. Olivine presents strong V_p anisotropy, of about 25%, and maximum V_s anisotropy of about 18% at ambient conditions for mantle composition of Fo90. The anisotropic state of the olivine is slightly changing with the variation of temperature and pressure (e.g. Abramson et al. 1997). The V_p and V_s anisotropy of the Orthopyroxene is of smaller magnitude and depends on the chemical participation percentages.

The highly volumetrically density of the olivine in the upper mantle enables this mineral to become the primary contributor of anisotropy. Through petrological experiments, it is possible to approach the behavior of the olivine aggregates in the upper mantle and to determine the relationship between the deformation and the LPO of the olivine. As mentioned earlier, the first experimental studies revealed that the fast axis of olivine (a axis) tends to align with the maximum shear directions for large strains (Zhang and Karato 1995). The latter implies that the measured fast wave polarization, reflects the direction of the maximum shear stress under the station. Nevertheless, the above view changed dramatically when new experiments unveiled different behaviors of the olivine aggregates. Jung and Karato (2001) showed that when olivine samples contain large amount of water into the crystal structure and they are deformed at high stresses and low temperatures, the fast

polarization direction tends to flip 90° away from the flow direction. This phenomenon was named “B-type” olivine fabric.

In addition, five types of olivine fabrics have been determined by experimental studies (e.g. Jung et al. 2006; Karato et al. 2008), i.e. the A-,B-,C-,D- and E-type of olivine fabric. The distribution of these fabrics in the upper mantle are highly disputed due to the poor population of the samples. Ismaïl and Mainprice (1998) showed that the most peridotite samples are A- and D-type. This conclusion disagrees with the work from Karato (2008), who claims that the asthenosphere is dominated by E- and C-types of olivine. These studies connect the olivine fabric type with the stress, temperature and water content conditions. In addition, transition between types are possible, such as from A-type to B-type at ~ 3 GPa (Jung et al. 2009). Of course, all these suggestions are partly theoretical and are based on laboratory experiments. Regarding the interpretation of shear wave splitting measurements, the A-type fabric assumption seems to remain the dominant factor of the connection between seismic anisotropy and the various tectonic settings (e.g. Long and Silver 2009), whereas the B-type is considered to be limited in the subduction zones (Karato 2008).

2.3.1.2 Lower mantle and transition zone

The mineralogy compositions in the lower mantle and in the transition zones is even more complicated compared with the upper mantle, due to the modelling difficulties performing experiments at the pressures close to the lower mantle conditions. Theoretically the petrology of the transition zone is dominated by garnet, majorite, wadsleyite, ringwoodite, calcium rich perovskite, clinopyroxene and in the lower mantle by perovskite, magnesiowüstite and possibly minor amount of SiO₂ (Mainprice 2007). There is not a fully explained theory about the development of LPO in the transition zone with very little experimental data. However, Tommasi et al. (2004) has simulated the development of LPO by the wadsleyite. Beneath the transition zone (except D'') there is not anisotropic contribution by the lower mantle due to diffusion creep mechanism (e.g. Karato et al. 1995).

Unlike the lower mantle the D''' region is characterized by high anisotropical properties. SPO and also LPO models have been suggested (e.g. Kendall and Silver 1998). The SPO approach is based on the existence of a material on the lowermost mantle with elastic properties that contrast with the surrounding matrix (in the form of partial melt). Models that invoke LPO are referring to the dislocation creep deformation with the existence of minerals such as perovskite, ferropericlase, and post-perovskite that generally have very large intrinsic shear wave anisotropy. Nevertheless, the LPO theories and the accompanied data are still incomplete.

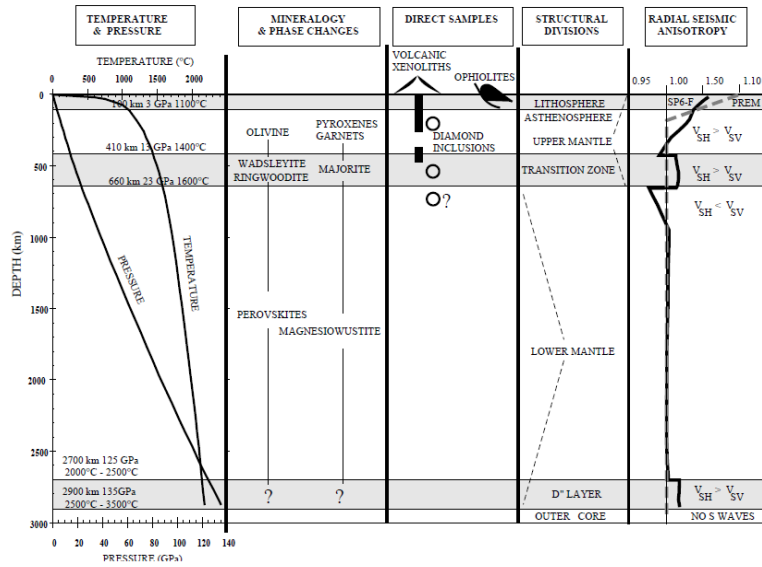


Figure 13: Physical and mineral variations in the earth's interior that contribute to anisotropy (Mainprice 2007)

2.3.1.3 Seismic Phases-Characterizing the anisotropy

There are many phases that are used in order to infer the anisotropic behavior of the mantle. The most popular are the so-called core phases, such as SKS and PKS. Core phases demonstrate several advantages compared to others that propagate in the Earth's interior. First of all, as it is implied by the nomenclature, the SKS phase is an S wave that is traversing the core as P wave which is converted again to S in the core to mantle boundary (CMB). This conversion controls the polarization, given that the observed anisotropy is strictly restricted on the receiver side (CMB-surface). In addition, the SKS-PKS waves are propagating nearly vertical through the upper mantle and, as a result, the incidence angle is within the shear wave window and, thus, the identification of them in the seismograms is much easier (Fig. 14).

SKS and PKS phases are always interpreted in terms of the receiver side anisotropy, due to CMB conversion. More specifically, shear-wave splitting results refer to the upper mantle anisotropy, given that any potential contribution from the lower mantle and from the crust is minor and can be ignored. However, there is an increasingly documented volume of evidences that support the contribution from the lower mantle, by the identification of splitting discrepancies between SKS-SKKS waves and deep S waves (e.g. Niu and Perez 2004; Long 2009).

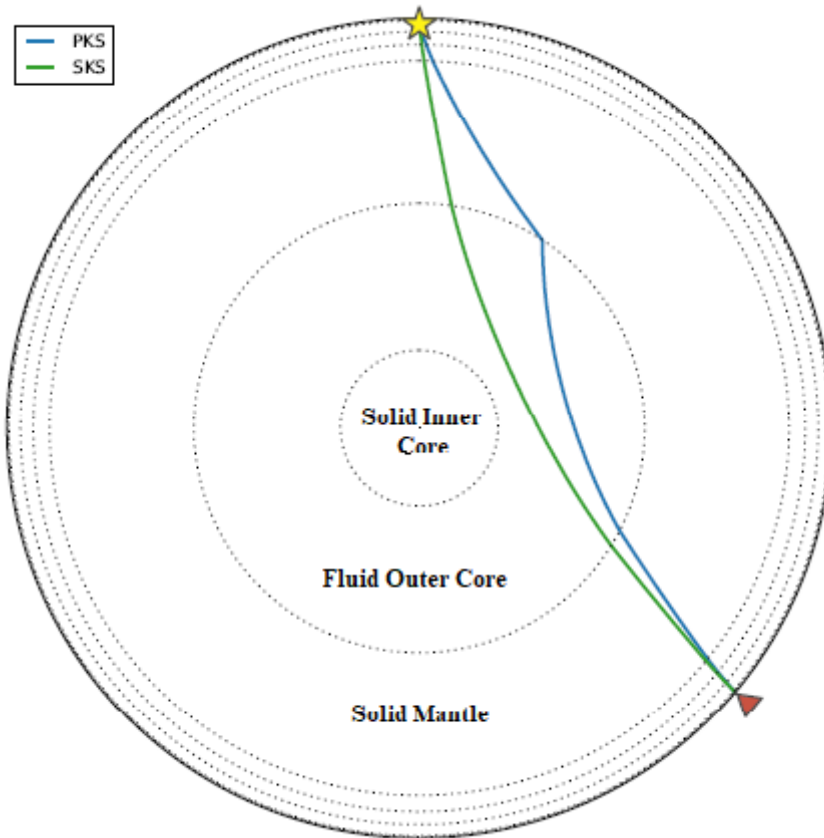


Figure 14: SKS and PKS phases propagating through the earth's interior, at epicentral distances of 130° . The star represents the hypocenter, whereas the triangle the seismic station.

2.3.1.4 Complex anisotropy

Complex anisotropy is an important phenomenon in SWS, due to variations in the internal structures. The presence of complex anisotropy is closely related with the existence of multiple anisotropic layers, dipping symmetry axes and lateral anisotropic variations. As it was described previously, the most common case of anisotropy is the so-called “simple anisotropy”, in contrast to the complex anisotropy cases that are harder to identify.

The determination of complex anisotropy is complicated and is based on multiple different observations on the analyzed data. Variations of apparent splitting parameters with backazimuth have been long recognized as a key factor regarding the complex anisotropy identification. For the case of multiple layers, the backazimuthal variation is characterized by a periodic variation on both φ and δt measurements with a $\pi/2$ periodicity (Silver and Savage 1994) (Fig. 15). A dipping axis of symmetry will form a π periodicity in case of transverse isotropy-hexagonal symmetry (Chevrot 2000). Complicated variations of splitting parameters with the backazimuth are a valuable diagnostic tool for complex anisotropy in depth, given that in these cases the average splitting parameters cannot be simply related to the mantle flow directions. Other elements that lead to possible complex anisotropy are the frequency dependence of splitting measurements, the lateral variations over short length scales and the discrepancies among different measurement methods.

All these diagnostic tools require dense seismological networks and years of available data in order to obtain descent backazimuth coverage. Keeping that in mind, in most cases data limitations preclude the complex anisotropy determination. The analyst should be extremely careful and cautious about any type of interpretations that include complex anisotropy.

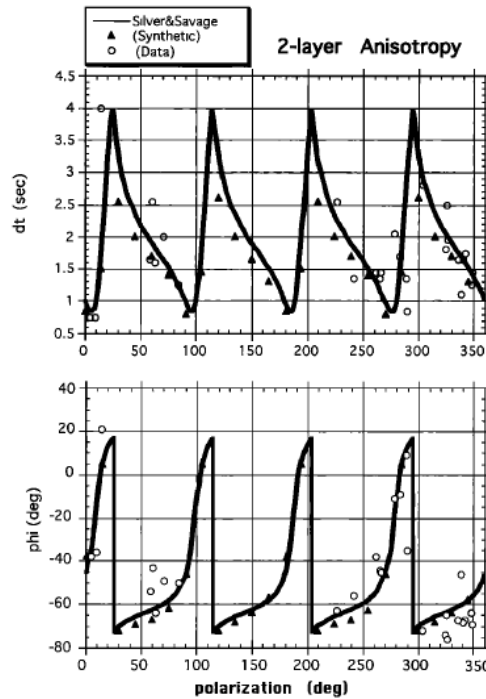


Figure 15: Values of ϕ and δt from synthetic seismograms. The solid line is the theoretical curve for a two-layered case anisotropy (Savage 1999).

2.3.2 Tectonic settings and SWS interpretation

2.3.2.1 Subduction Zones

Seismic anisotropy constitutes a powerful tool in the analysis and the interpretation of mantle dynamics in subduction zones, due to the undoubted relation between the mantle flow-deformation and the splitting directions. In contrast with other seismological tools such as seismic tomography, seismic anisotropy is able to reveal on-going dynamic processes regarding mantle structures. For decades, shear-wave splitting studies consisted a popular application in the subduction zones, revealing from the early years that interpretations with the use of simple two-dimensional flow field models are very weak and more advanced three-dimensional models are required.

Most splitting studies in subduction zones are utilizing SKS phases, which are very sensitive to the sub-slab, slab and wedge anisotropy (e.g. Abt et al. 2010; Baccheschi et al. 2011). On the other hand, local S phases originated by slab quakes and source-side shear-wave splitting are commonly used (e.g. Soto et al. 2009; Evangelidis 2017), aiming to isolate wedge and sub-slab anisotropy, respectively. The main advantage of the shear-wave splitting methods in these geodynamical issues is the straightforward connection with the anisotropic theory, leaving aside complicated inversion techniques. However, a major problem in the shear-wave splitting technique is the limited depth

resolution due to the path-integrated results, given that a sole SKS measurement contains additional anisotropic information from the lower mantle and the crust.

Shear-wave splitting results in the subduction zones and especially in the mantle wedges are quite complex. Many subduction systems are dominated by either trench-parallel or by trench-perpendicular fast directions (e.g. Long and Silver 2008). In general, shear wave splitting patterns in the mantle wedges present large time-delay values (0.1s-1.5s) and spatial variations (Long and Wirth 2013). Additional complications are the existence of transitions from trench-parallel to trench-perpendicular fast directions and vice-versa in the vicinity of the arc and further in the back arc (e.g. Levin et al. 2004; Long and van der Hilst 2006). Sub-slab contribution to the observed splitting is also very important. Sub-slab anisotropic signal can be isolated by anisotropic corrections, wedge anisotropy corrections for the SKS phases or receiver corrections for the direct S waves (source-side). Both techniques have possible errors due to imperfect corrections. The results for the sub-slab anisotropy are also complicated and the fast splitting directions are either dominantly trench-perpendicular or trench-parallel and with large ranges of average sub-slab time delays (e.g. Long 2013 and references within). Except from the wedge and sub-slab contribution, the slab itself contributes to the observed splitting measurements. Theories about fossil anisotropy and aligned serpentized cracks dominate the efforts for interpretation, but arguments based on SKS phases are indirect and contain errors (Faccenda et al. 2008). Combination of local S splitting and anisotropic receiver function results may yield more stable conclusions (Fig. 16).

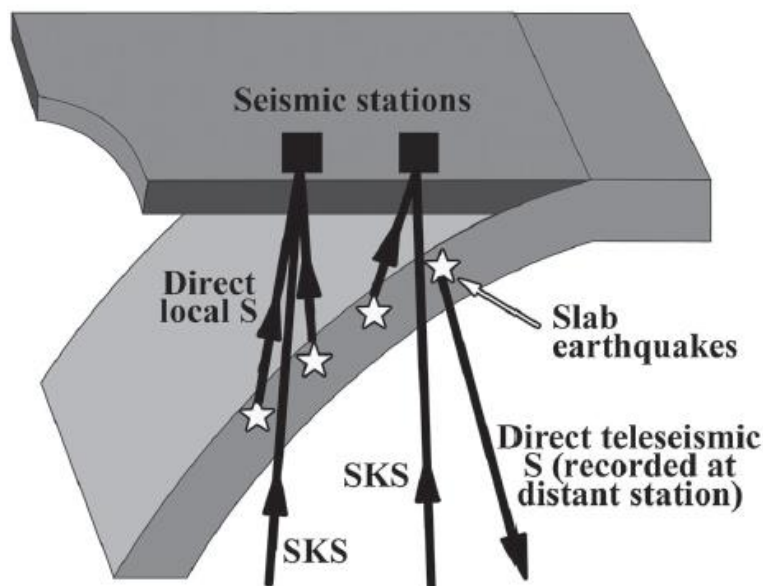


Figure 16: Sketch of seismic ray paths commonly used in the shear wave splitting studies in the subduction zones including SKS phases, local S waves and direct teleseismic phases (Long and Silver, 2009).

In addition, the assumptions about the different types of olivine fabrics play an important role in the shear wave splitting interpretations in subduction zones. The olivine fabric types have been already mentioned in detail, so the basic types for the interpretation in the subduction zones will be briefly restated. The most important type of olivine fabric in subduction dynamics is the B-type. The fast axes of olivine tend to align in the shear plane but 90° away from the shear direction, so the relationship between the fast direction axes and the mantle flow is changing by 90° (Jung and Karato 2001). The C- and E-type of fabric possible dominate the mantle wedge and the sub-slab (Karato et al. 2008), with no differences with the expected fast directions compared to the A-type (Fig. 17). The presence of water in the subducting slab is considered vital for the fabric types, due to the hydrous minerals that release water into the wedge in high temperature and pressure conditions. Also,

serpentine minerals, such as antigorite, are considered relevant to the seismic anisotropy interpretation, given that they have strong intrinsic single crystal anisotropies (e.g. Katayama et al. 2009).

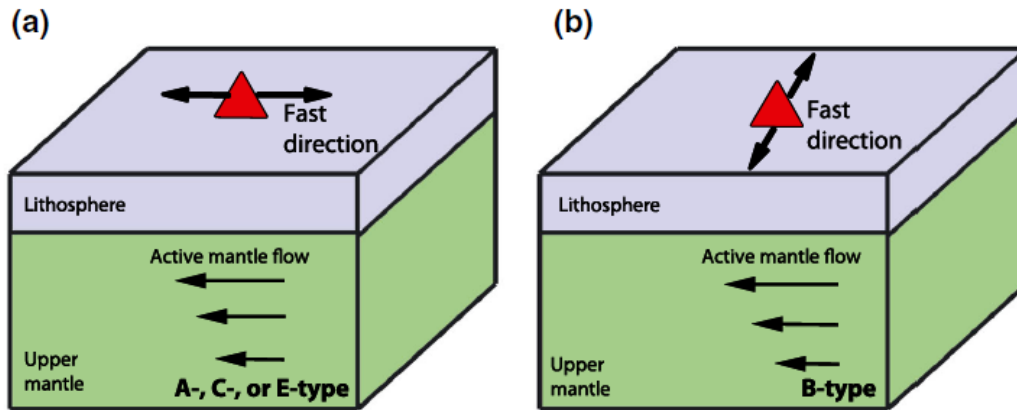


Figure 17: Cartoon sketch that presents the effect of each type of olivine fabric in the fast directions interpretation (Long and Becker 2010).

2.3.2.2 Conceptual models

Based on seismological observations, mineral physics and geodynamical modelling, a large number of conceptual models have been synthesized in order to interpret the SWS results in the subduction zones. Three conceptual models, that try to explain the fast directions beneath the slabs, exist. The first one is the “trench-parallel flow” model by Russo and Silver (1994) that has been applied in several subduction systems, like the Calabria (e.g. Baccheschi et al. 2008) and Scotia (e.g. Müller et al. 2008). The trench-parallel sub-slab flow model requires a high degree of mechanical decoupling between the slab and the mantle and a barrier to entrain mantle flow at depth. Exceptions to this model can be associated with local sub-slab decoupling reflecting a 2-D flow or to the slab geometry (Long and Silver 2009). Numerical modelling by Faccenda and Capitanio (2013), demonstrates a toroidal flow around the slab edge that results to a deep anisotropic layer with trench parallel fast directions beneath a layer of entrained sub-slab flow. This model is very similar to the one proposed by Russo and Silver (1994) and can explain the trench parallel SKS splitting near the edges of retreating slabs.

The second model is the “pressure-induced B-type fabric” (Jung et al. 2009), presented in Figure 18. This model assumes that the upper mantle in depths greater than 90 km should be dominated by B-type fabric of olivine, rather than the commonly assumed A-type. This model implies that subduction systems that exhibit trench-normal fast directions might reflect trench-parallel flow. The last and more recent model, proposed by Song and Kawakatsu (2013) invokes a layer of suboceanic asthenosphere entrained beneath subducting slabs, with the suboceanic asthenosphere being characterized by strong radial and weaker azimuthal anisotropy. All three models have advantages and disadvantages and probably none of these describes fully the sub-slab behavior.

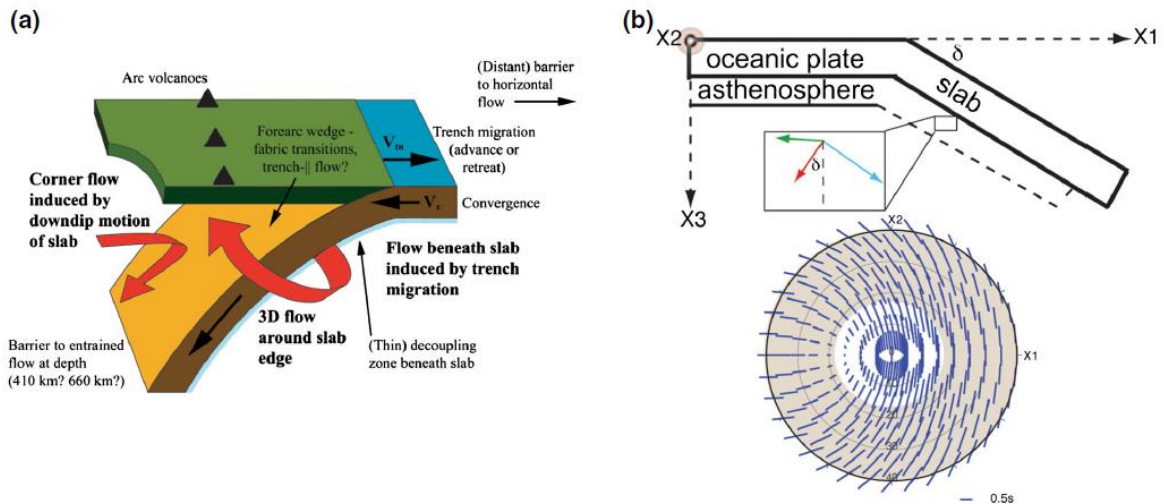


Figure 18: Cartoon sketch of the two plausible models for the sub-slab anisotropy. (a) The trench migration controlled model (Long and Silver 2008) that explains trench parallel sub-slab fast directions. (b) Model by Song and Kawakatsu (2013) that proposes an orthorhombic symmetry for the oceanic asthenosphere.

The anisotropy within the slab can be categorized in two main models. The first is the “frozen lithospheric anisotropy” and the second one is the “serpentinized fault model”. In the first case the anisotropic structure is created due to horizontal shear, as the lithosphere moves over the asthenosphere. The lithosphere moves away from the spreading centers and cools with mechanical rigid results. The anisotropic structure contains past deformation, “frozen” into the subducting plate. If this hypotheses are valid, the frozen anisotropy geometry has to reflect fossil spreading directions at the time the lithosphere was formed (Forsyth 1975). The second model is an alternative interpretation effort by Faccenda et al. (2008) that proposed a modification of the anisotropy by hydration and faulting in the downgoing slab. They suggest a combination of LPO and SPO of highly anisotropic serpentinite minerals with trench parallel fast axis and up to 1s time-delay of SKS phases. In contrast to the above proposed anisotropy models in the sub-slab and the slab, the conceptual models for the mantle wedge are numerous and detailed analysis of each one is beyond the scope of this thesis. Long and Wirth (2013) concluded that there is not a solid model that can fully explain the observed anisotropy in the mantle wedge and competing factors, such as downdip, motion of the slab, trench migration, slab morphology and mantle flow play vital role in the fast directions of splitting.

2.3.2.3 Continental Regions

Another significant issue is the anisotropic conditions and their interpretation through the SWS results in continental regions. There are two major constraints that seek solution with the SWS analysis in the stable continental regions. The first one is the existence and operation of a mechanical asthenosphere and the second one is the role of lithospheric mantle in orogenic deformation. The connection between the shear-wave splitting directions and the deformation is uncontroversial, but the exact parameters of this relations remain until today unsolved.

The observable patterns of seismic anisotropy in continental regions vary, but certain hypotheses towards their interpretation are widely accepted. Many continental regions demonstrate anisotropy that is closely related with surficial geological structures (Barruol et al. 1997), fact that supports the existence of coherent lithospheric and sublithospheric deformation. Compatible with the above observations are the closely related to the local Absolute Plate Motions (APM) seismic anisotropy patterns (e.g. Vinnik et al. 1989), implying that seismic anisotropy is sublithospheric with motion

transmission from the mantle to the top of the lithosphere. The approach regarding the lithospheric and sublithospheric origin of the anisotropy is supported by many studies (e.g. Behn et al. 2004; Walker et al. 2004).

A plethora of models have been proposed to interpret the complexity and variance of seismic anisotropy patterns in continental regions. However, most continental regions exhibit a possible couple or partial coupled conditions between the lithosphere and the sublithospheric mantle (Fouch and Rondenay 2006).

2.4 Methodologies

2.4.1 Introduction

There are two groups of techniques for estimating the parameters φ and dt of the shear wave splitting analysis regarding upper mantle anisotropy studies. The first group concerns the simultaneous analysis of seismic events, belonging to a selected dataset, with various azimuths (Vinnik et al. 1989; Chevrot 2000). The second group includes methodologies that determine these parameters on a per-event basis (Bowman and Ando 1987; Silver and Chan 1991; Menke and Levin 2003). The last type of shear-wave splitting techniques will be presented in detail, given that it will be applied to the present master thesis (Fig. 19).

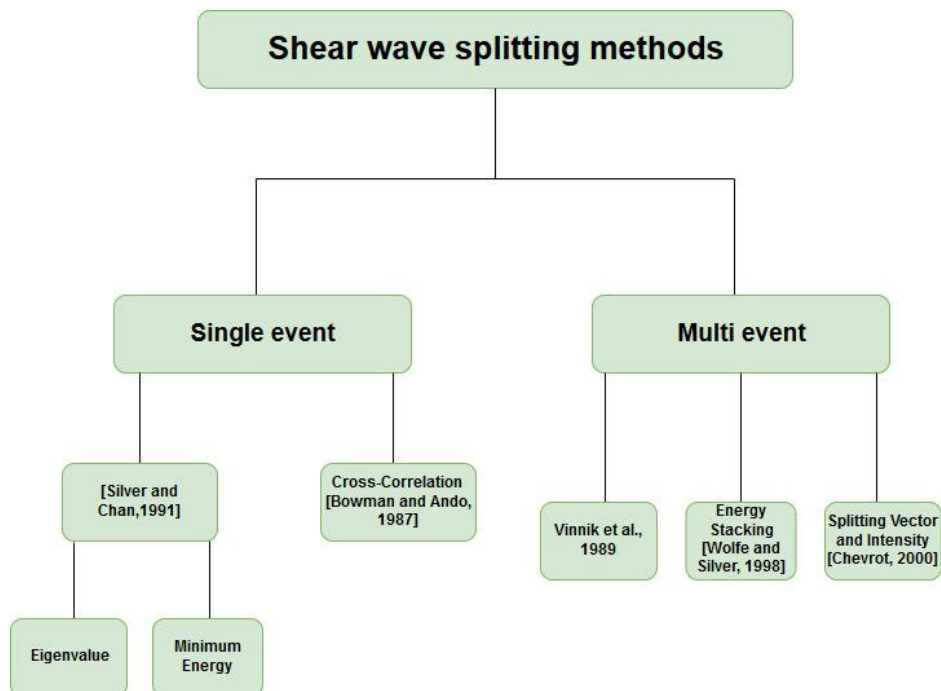


Figure 19: Two main branches of shear-wave splitting methods modified by Wüstefeld (2007).

2.4.2 Multi-event techniques

Vinnik et al. (1989) proposed to stack the normalized transverse components of every record per station with azimuth-dependent weights, in order to evaluate the shear-wave splitting parameters. Based on the latter methodology, Chevrot (2000) introduced the splitting vector (or multichannel method), as alternative to the single event techniques. This method measures the splitting intensity, S , which is given projecting the transverse components on the radial components derivatives. If the azimuthal dependence of the splitting intensity (referred to as the splitting vector) is measured, the best fitting splitting parameters (φ, dt) can be retrieved by fitting a $\sin(2b)$ curve to the splitting vector. The splitting intensity measurements can be stacked in azimuthal bins. Main disadvantage of this method is the required broad range of azimuthal coverage.

In addition, Wolfe and Silver (1998) proposed a stacking method for shear-wave splitting analysis. For every set of splitting parameters, the energy $E_t(\varphi, dt)$ on the transverse component is computed, as described by Silver and Chan (1991). The $E_t(\varphi, dt)$ stacking gives a global energy value for every station, whose minimum value provides the optimal splitting parameters. Nevertheless, the method assumes single layer anisotropy. Thus, complex anisotropy structures cannot be defined.

2.4.3 Single event techniques

2.4.3.1 The Transverse Component Minimization Method

The minimum energy method is one of the most popular splitting measurement methods for single event data. Below, the methodology described by Silver and Chan (1991) is presented.

The shear wave in a homogenous and isotropic medium can be written as vector function:

$$u(\omega) = Aw(\omega) \exp[-i\omega T_0] \quad (2.6)$$

where:

ω = angular frequency

$u(\omega)$ = isotropic shear wave vector

$A(\omega) = w(\omega) \hat{A}(\omega)$ complex amplitude vector

$w(\omega)$ = norm of the amplitude with angular frequency ω

T_0 = shear wave arrival time

In order to represent the shear-wave direction and orientation, a right-handed set of orthogonal vectors $[\hat{p}\hat{a}\hat{b}]$ is defined:

\hat{b} = propagation vector

\hat{p} = polarisation vector pointing in the direction of the shear-wave displacement

\hat{a} = null vector $\hat{b} \times \hat{p} = \hat{a}$

Silver and Chan (1991) assume that waves displace in the same direction \hat{p} . As a result, the complex amplitude vector $A(\omega) = w(\omega) \hat{A}(\omega)$ can be approximated by replacing $\hat{A}(\omega)$ with \hat{p} for all frequencies. So (2.6) is rewritten as:

$$u(\omega) = w(\omega) \exp[-i\omega T_0] \hat{p} \quad (2.7)$$

For an anisotropic medium we have to define a different coordinate system $[\hat{f}\hat{s}\hat{b}]$, utilizing the fast \hat{f} and the slow \hat{s} directions (orthogonal to each other), with respect to the propagation direction \hat{b} . Moreover, \hat{f} and \hat{s} are eigenvectors of a polarisation tensor V (Christoffel matrix) defined by the equation $V_{il} = c_{ijkl} b_j b_k$. Solving the eigenvalue problem that comes from this matrix, it gives the \hat{f} and \hat{s} as eigenvectors corresponding to the direction of particle displacement for the split wave. The eigenvalues are the shear velocities in every direction.

In order to produce a split wave from the un-split shear wave (2.7), the splitting operator must be applied. The operator $\Gamma(\varphi, dt)$ rotates and time shifts the shear wave and it is a function of the splitting parameters. It is defined as:

$$\Gamma(\varphi, dt) \equiv \exp\left(\frac{i\omega dt}{2}\right) \hat{f}\hat{f} + \exp(-i\omega dt/2) \hat{s}\hat{s} \quad (2.8)$$

Also the time difference tensor is defined as:

$$dT = dt/2(\hat{f}\hat{f} - \hat{s}\hat{s}) \quad (2.9)$$

The compact splitting operator:

$$\Gamma(\varphi, dt) = \exp[-i\omega dT(\varphi, dt)] \quad (2.10)$$

Applying the splitting operator to a shear-wave, we obtain a split-wave:

$$u_s(\omega, t) = \Gamma(\varphi, dt)u(\omega, t) \quad (2.11)$$

The most straightforward way to find the splitting parameters is to correct for the anisotropy and choose the pair that more clearly returns the split wave (2.11) to the un-split one (2.7). Applying the inverse splitting operator (Γ^{-1}), the splitting effects are removed from the split wave:

$$u(\omega, t) = \Gamma^{-1}(\varphi, dt)u_s(\omega, t) \quad (2.12)$$

The best pair is selected by calculating the covariance matrix of the two orthogonal fast and slow components in the splitting coordinate system. The covariance matrix is used to find the inverse splitting operators. In the anisotropic cases (all real data), the covariance matrix has two non-zero eigenvalues λ_1, λ_2 , while in isotropic cases the matrix has only one non-zero eigenvalue λ_1 . The first eigenvalue λ_1 describes how well the two split waves match after the splitting correction. The particle motion graph illustrates this phenomenon. When the fast and slow components are out of phase the particle motion is elliptical and when they are in phase the particle motion is linear. Also,

λ_1 is maximum when the particle motion is linear. The covariance c_{ij} of two orthogonal components of ground motion is defined as:

$$c_{ij}(\varphi, dt) = \int_{-\infty}^{\infty} u_i(t)u_j(t - \delta t)dt \text{ with } i, j = 1, 2 \text{ for lag } dt \text{ (2.13)}$$

The optimal pair (φ, dt) will be defined via a grid search, so that the covariance matrix \mathbf{c} is singular. In the presence of anisotropy, the matrix \mathbf{c} cannot be singular, but the closest value to singular is obtained. The second eigenvalue, λ_2 , of \mathbf{c} is used to determine the pair of φ and dt that best reverses the effects of splitting. The pair that produces the smallest λ_2 is the one that optimally matches the waveforms and the particle motion becomes as linear as possible.

A special case of this methodology can be applied if the isotropic polarization vector ($\hat{\mathbf{p}}$) is known, as it is the case for SKS and SKKS phases. In these cases, the amount of energy on the corrected transverse component is measured, producing a contour plot of transverse component energy for all the possible pairs (φ, dt) . The best fitting parameters correspond to the minimum on this plot and the formal errors of the measurements are estimated using an F test formulation. The energy on the corrected transverse component can be determined by:

$$E_t = \int_{-\infty}^{+\infty} \tilde{u}_t^2(t) dt \text{ (2.14)}$$

In this case the energy (E_t) can be minimized instead of λ_2 on the corrected transverse component. The time domain expressions for the transverse and the radial component are defined by the equations:

$$u_t(t) = -\frac{1}{2} \left[w \left(t + \frac{\delta t}{2} \right) - w \left(t - \frac{\delta t}{2} \right) \right] \sin(2\varphi) \text{ (2.15)}$$

$$u_r(t) = w \left(t + \frac{\delta t}{2} \right) \cos^2 \varphi + w \left(t - \frac{\delta t}{2} \right) \sin^2 \varphi \text{ (2.16)}$$

The Transverse Component Minimization Method in most cases results to the eigenvalue method, when the minimization of the second eigenvalue λ_2 is considered. In the special case of minimizing equation (2.14), the method is called Minimum Energy.

2.4.3.2 The cross-correlation method

The cross-correlation method follows the basic principles as the minimum energy method. It uses a grid search approach in order to identify the optimal anisotropic pair (φ, dt) for each event. More specifically, the seismograms-components (depending on the ray coordinate system) are rotated and time shifted. Bowman and Ando (1987) rotated the seismograms from 0° to 90° at 5° intervals but SplitLab rotates from -90° to 90° with 1° interval. Following, the pair that produces the maximum cross-correlation coefficient is considering the splitting measurement. Cross-correlation is the measurement of the similarity of two series as a function of the displacement of one relative to the other. For continuous functions f and g , the cross-correlation is defined as:

$$(f * g)(\tau) = \int_{-\infty}^{\infty} f^*(t)g(t + \tau) dt$$

Where f^* denotes the complex conjugate of f and τ where is the displacement, also known as lag. The main goal is to maximize the cross-correlation between the corrected horizontal components, which is mathematically equivalent to maximizing the determinant of the time domain covariance matrix (e.g. Silver and Chan 1991). These parameters maximize the similarity between the two pulse shapes of the corrected components. Moreover, the “corrected” particle motion is being considered to identify the most appropriate time shift. In most cases the “corrected” particle motion is more linear than the original. The cross-correlation method was first applied in studies by Fukao (1984) and Bowman and Ando (1987).

2.4.3.3 The cross-convolution method

Menke and Levin (2003) proposed the cross-convolution method in order to address the complex anisotropy problem. In contrast to other shear-wave splitting measurement methods that rely on the assumption of a single anisotropic layer with horizontal axis of symmetry, the cross-convolution method is also suitable in the case where shear waves propagate through multiple regions of diverse anisotropic properties, with different dipping axes of anisotropic symmetry. The computations in this technique concern the convolution of the observed radial and tangential component seismograms with the impulse responses predicted by a hypothetical Earth model. Then the model is modified in order to minimize the misfit between observed and predicted seismograms. Based on both synthetic and real data, Menke and Levin (2003) emphasized the similarity of the results with the ones obtained by other single event methods, in the presence of a single horizontal anisotropy layer and the superiority of the cross-convolution method for the determination of the complex anisotropy.

2.4.4 Comparison of the measurement methods

Each of the above-described methods follows a different procedure in order to determine the splitting parameters. It is self-evident that in theory all these techniques should yield identical, or at least similar, estimations. But in most cases of analyzing real data, the dependence on the anisotropic structures and the quality of the data have as a result different measurement methods to yield different splitting parameters. This phenomenon has been investigated by many researchers for completely different datasets (e.g. Long and van der Hilst 2006; Vecsey et al. 2008).

Long and van der Hilst (2006) compared the transverse component minimization, cross-correlation and multichannel methods for SKS phases and direct S waves for two stations in Japan with different anisotropic behavior. They concluded that the transverse component minimization and the cross-correlation methods usually more likely disagree in the presence of complex anisotropy.

Vecsey et al. (2008) compared splitting parameter results for both synthetic and real SKS data, obtained using the transverse component minimization, the cross-correlation and the eigenvalue methods. They suggested the use of the transverse component minimization method for SKS splitting analysis, mentioning that it is more stable and robust for noisy data. In addition, Long and van der Hilst (2006) observed that the minimum energy method is more sensitive in the presence of complex anisotropy beneath a station. The ideal, is a simultaneous application of various methods in order to increase the confidence and to avoid problems posed by phases whose incoming polarization directions are near the null directions (e.g. Levin et al. 2004). The latter was adopted in the present thesis.

2.5 SplitLab

SplitLab is a graphical user interface for the determination of shear wave splitting parameters, focused in the analysis of teleseismic events. It was developed by Wüstefeld et al. (2008) in Matlab and its main goal is the analysis and interpretation of the continuously growing seismological datasets for seismic anisotropy studies. The program is designed and tested for SKS phases but, as mentioned by the authors, shear wave splitting analysis of other phases (such as PKS, SKKS etc.) is also performed.

SplitLab follows a specific workflow that includes: (1) Project Configuration, (2) seismogram visual inspection and shear wave splitting procedure and (3) outputs and statistical analysis. In the first step (1), a SplitLab analysis project is created, setting the basic parameters for the analysis such as earthquake catalog, stations information, path for the SAC input waveforms and output file. For each station a separate Project is created. The second step (2) is executed on the seismogram viewer module, where visual inspection of the seismograms to be analyzed is included. The waveforms can be processed using a plethora of available tools, such as rotation, filtering, spectrogram and particle motion analysis. The rotation is performed in the three-dimensional ray system LQT, as presented in Figure 20. The three-dimensional rotation uses a transformation matrix to change the output vectors from the ZEN to LQT system. These tools aim to assist the user to define the appropriate time window for the shear wave splitting analysis (Fig. 21). The arrival time of each selected phase is indicated, using the matTaup toolbox (www.ess.washington.edu/SEIS/FMI/matTaup.htm).

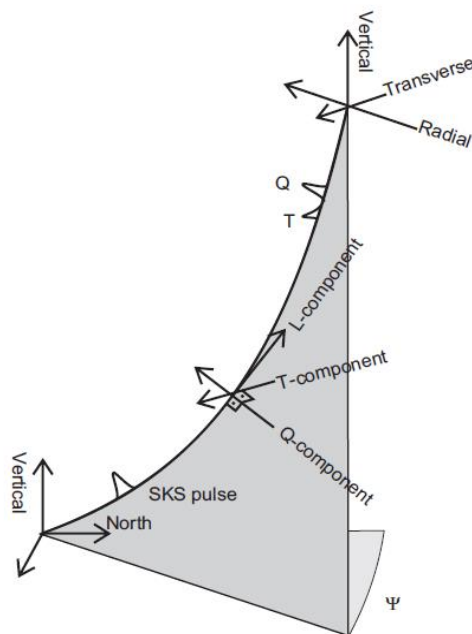


Figure 20: LQT ray coordinate system. The L-component is aligned with the direction of the P wave propagation (ray pointing from earthquake to station), the Q component is aligned with the direction of the SV wave propagation (pointing towards earthquake) and the T-component is perpendicular to the ray plane and is aligned in the direction of the SH phase movement (Wüstefeld et al. 2008).

The original seismograms are tapered, detrended and filtered. Next the waveforms are cut in the selected time window. After this selection, SplitLab performs simultaneously shear wave splitting measurements with three different methods, i.e. the Minimum Energy (SC), the Eigenvalue (EV) and the Rotation-Correlation (RC) methods. Following, the results of the fast shear-wave polarization direction and the time delay between the two split shear-waves are displayed in a diagnostic plot (Fig. 22) allowing the user to quickly evaluate them and to assign specific quality characterization.

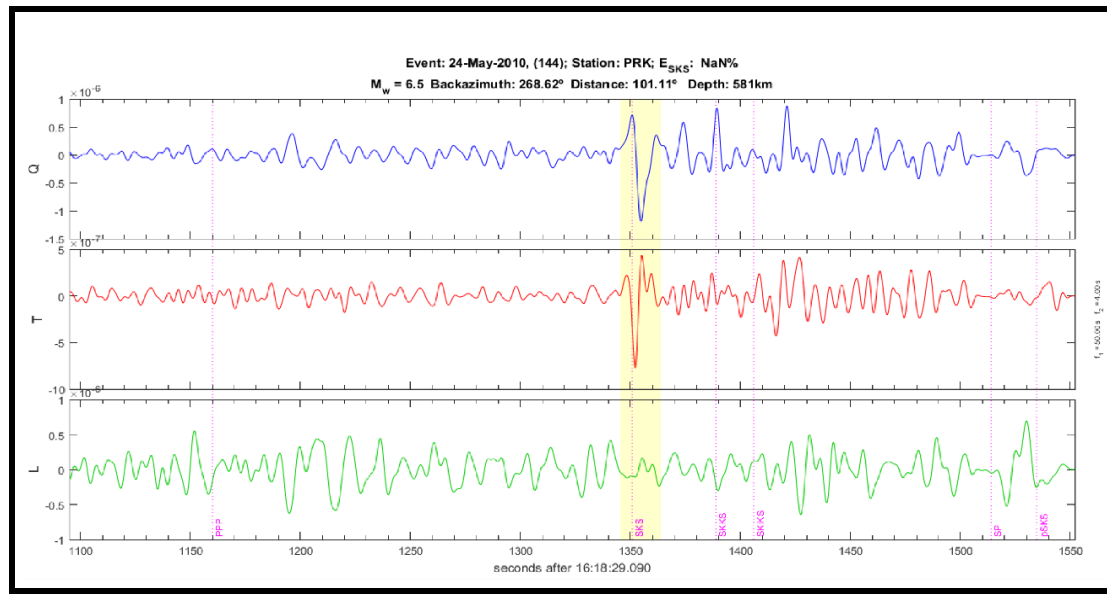


Figure 21: The seismograph viewer module displaying three component seismograms. The selected window is presented with the yellow color and the theoretical arrival times for each phase with dashed pink lines. The header provides details for the event and the station.

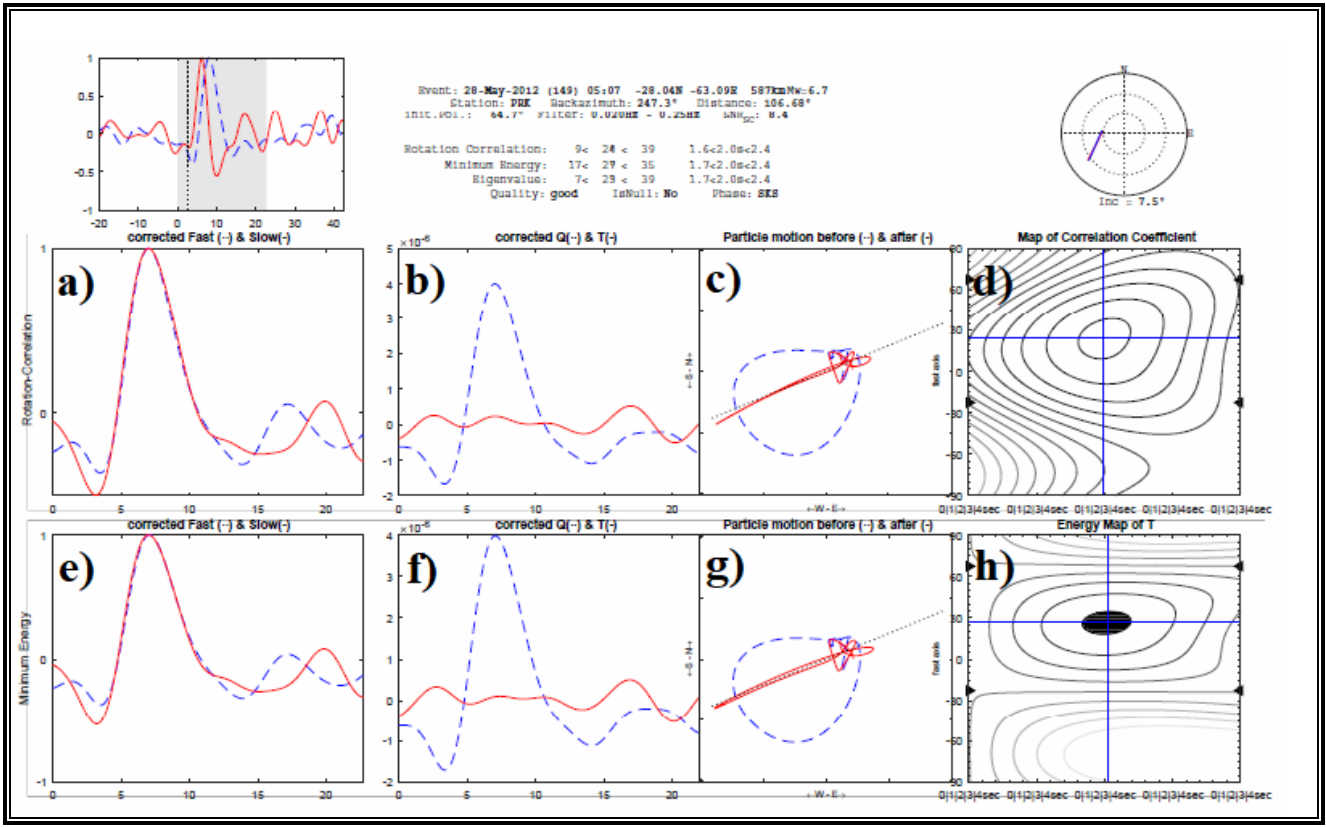


Figure 22: Diagnostic plot of a single measurement. The center panel displays the RC results: a) components of fast and slow directions after time-delay correction, b) radial (Q, solid) and transverse (T, dashed) component after RC correction, c) particle motion before (dashed) and after (solid) the correction, d) map of Correlation Coefficient. The lower panel displays results for the SC method: e) SC fast and slow components after the correction, f) radial and transverse component after the correction, g) particle motion before and after the correction, h) map of minimum energy values in the transverse component. In the upper right panel a stereoplot of the result is presented and in the upper left the Q (solid) and T (dashed) components before anisotropy corrections. The header provides details for the event and the splitting results for the three methods.

2.5.1 Ranking Shear-Wave Splitting measurements

Specific rules have been adopted in order to guarantee the reliability of the splitting measurements in the semi-automatic procedure of quality ranking based on bibliography and on the expert's personal experience. Splitlab offers three different ranking categories, “good”, “fair” and “poor” results. Based on the studies *Making Reliable Shear-wave Splitting Measurements* (Liu and Gao 2013) and *Null detection and weak anisotropy in shear-wave splitting* (Wüstefeld and Bokelmann 2007) a set of criteria was applied in the present thesis for each ranking category. “Good” quality measurements have all the following characteristics:

- Outstanding SKS-PKS arrival on both the original radial and transverse component.
- Effectively removed all the energy in the transverse component after the splitting (time-delay) correction.
- Elliptical particle motion of the original and linear or close to linear particle motion of the corrected waveforms.

- Well-defined minimum on the contour map for the minimum energy and for the eigenvalue method.
- Consistency of the results obtained for the same event-station pair, obtained by the SC, RC and EV methods ($\Delta\Phi < 20^\circ$ and $\Delta dt < 0.8$ s).
- Event-station pairs with Signal to noise ratio (SNR) > 5 on the radial component (Restivo and Helffrich 1999).

If any of the above criteria is not fulfilled, for example the SKS arrival is not so clear or there is no well-defined minimum, the measurement is downgraded from “Good” to “Fair”. “Fair” quality results have sufficiently lower quality compared to the “Good” measurements and the consistency between the three methods is decreasing ($\Delta\Phi < 30^\circ$ and $\Delta dt < 1.2$ s). Both “Good” and “Fair” results are used in the interpretation of the results. If more than two of the above criteria are not fulfilled the measurement is characterized as “Poor” and is not used in the interpretation. It should be mentioned that in certain cases the evaluation of the results is subjective, given that it evolves the seismologist’s personal judgment.

2.6 Results

The SWS analysis procedure had as a result 898 high quality (“good” + “fair”) φ and dt , including null pairs, from more than 19000 waveforms that were analyzed for the previously mentioned time-period (2010-2017) (Fig. 23), with an overall 4.6 % of success. In more detail, the analysis resulted to 696 and 202 accepted pairs for the SKS and PKS phases, respectively. This difference in the number of accepted pairs can be explained by the dataset availability, given that the available earthquakes within the PKS window were significantly less. In addition, 118 null measurements were identified based on the applied criteria (no signal in the T component and null RC value). For each station, the circular median and the mean value were calculated for the fast polarization (φ) and the delay time (dt) values respectively, using the Circular Statistics Toolbox (Berens 2009). In addition, the Standard deviation (Std) and the error of the results were also calculated. The detailed results of this procedure are presented in Table 1 (SKS phases) and Table 2 (PKS phases). Furthermore, mean SKS and PKS splitting results are displayed for each station (Fig. 24), along with the main tectonic features of the area.

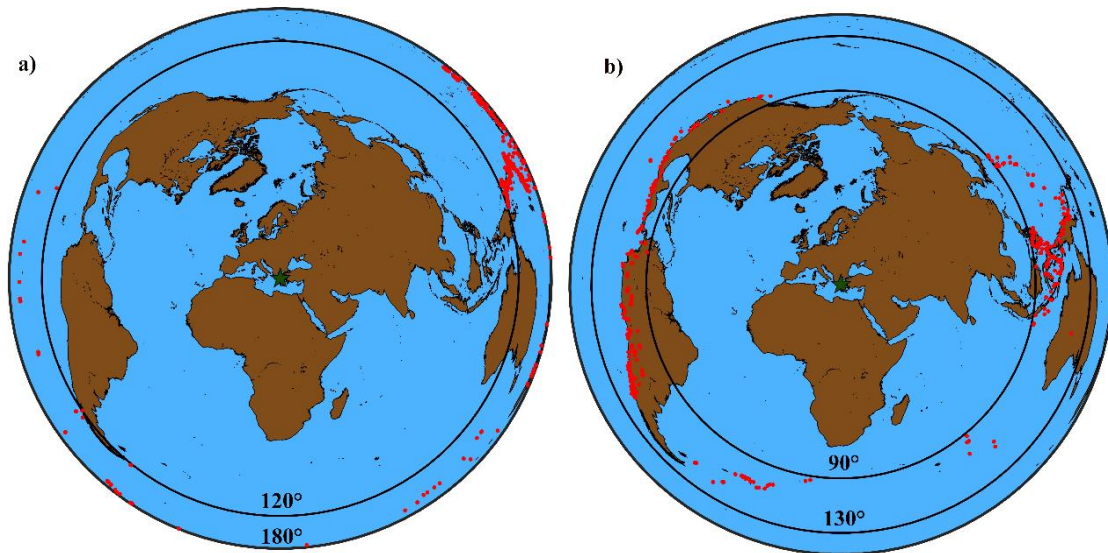


Figure 23: Seismic events epicenter distribution for the PKS (a) and for the SKS (b) phases.

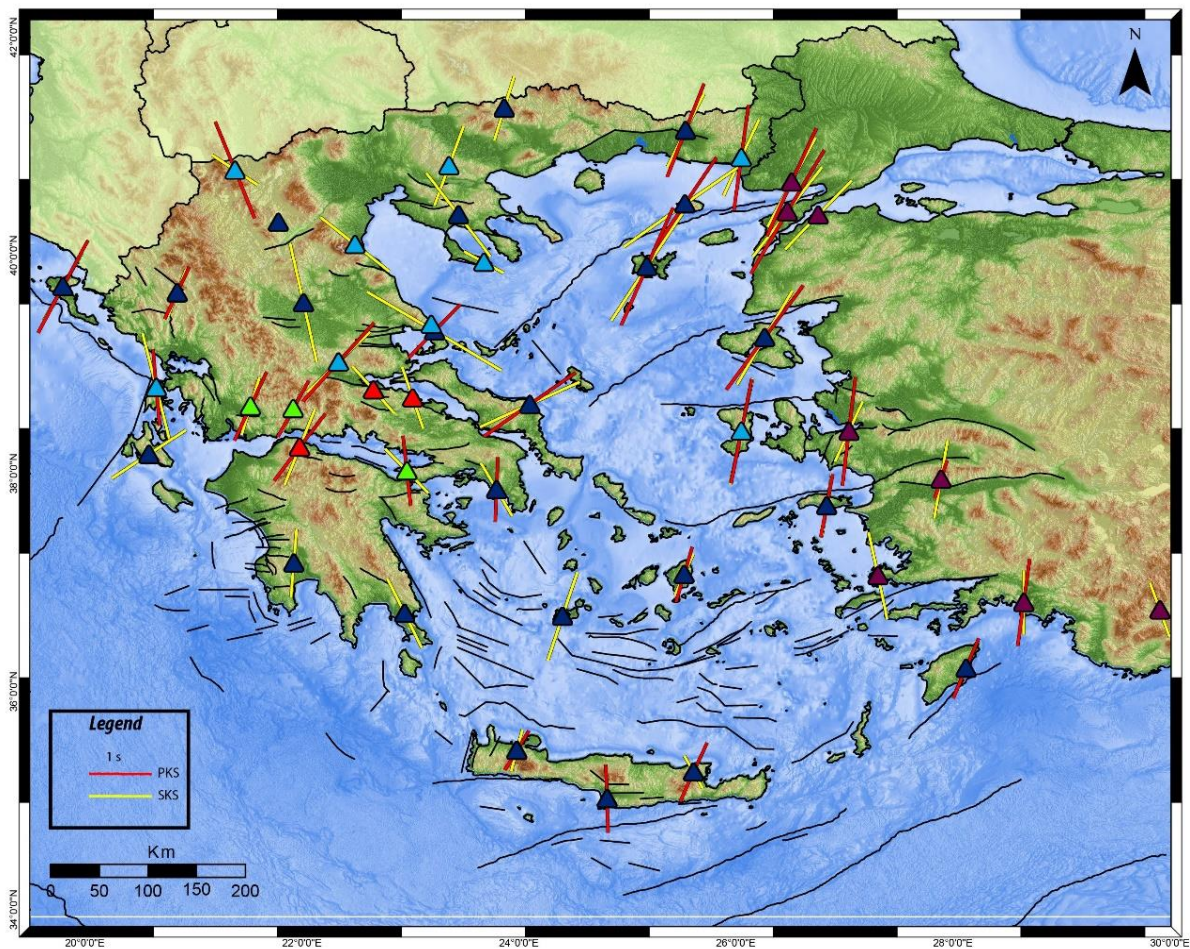


Figure 24: Station-averaged splitting results from the SWS analysis. The mean values at each station are represented with yellow (SKS) and red bars (PKS) and indicate the fast direction (ϕ), whereas the length of the bar that is proportional to the calculated average time delay (dt). Main tectonic features of the Greek region by Ganas et al. (2013).

A major issue in SWS studies is the low number of the produced results, due to the limited data availability, effect of permanent networks absence for a long time-period in an area under study. An alternative to acquire a basic knowledge about the anisotropic behavior of a region, is to utilize data from temporary stations. Thus, in most cases the determined SWS results are few and the interpretation of them is not safe. Based on this view, we analyze recordings by permanent stations in the Greek region with adequate operational time, i.e. at least four years. The latter led to the determination of a satisfactory number of splitting pairs for the selected stations. Figure 25 present the Std and error variations with the number of the results for each station for the SKS and PKS phases, respectively. For the SKS phases, scattering of both Std and error values is observed for stations with low number of results. In the cases of stations where more than 15 SWS measurements have been obtained, the respective values are concentrated in a narrower range, implying a connection between the number of results and the Std-errors values. This observation is not valid for the PKS results, probable due to the limited number of results.

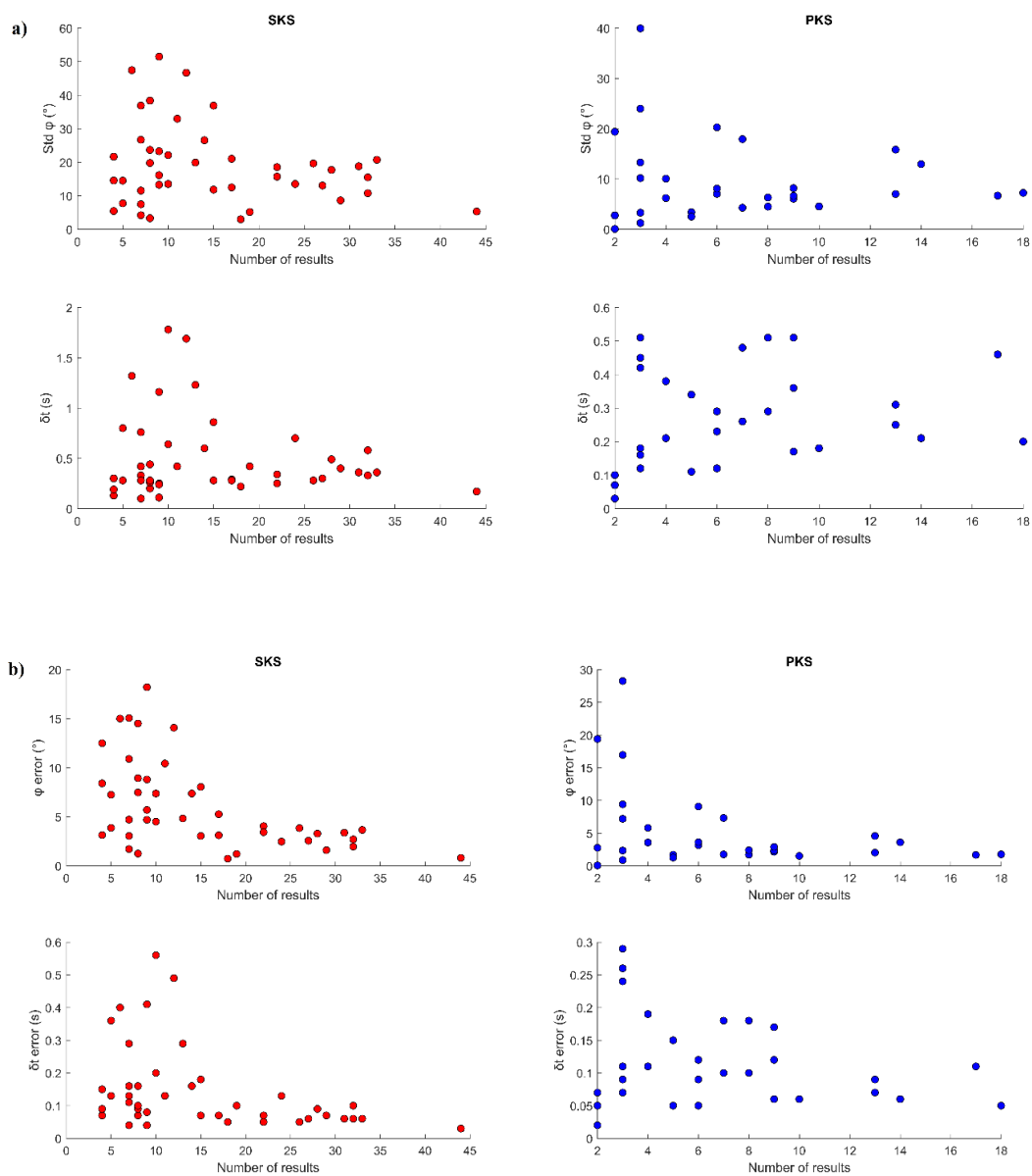


Figure 25: Variations of the Standard deviation (a) and the error (b) with the number of results for the SKS and the PKS phases.

The back-azimuthal coverage is not uniform and it is concentrated between 50°- 100° and 200° - 310° for both SKS and PKS phases, as presented in Figure 26. This phenomenon is due to limited back-azimuthal coverage of the available data for the SWS analysis. The observed gaps prevent the identification of possible complex anisotropic behavior beneath the stations. Considering this, it is more appropriate to adopt the simplest anisotropic model for the interpretation, the so-called “single layer”. The single layer hypothesis can be also justified by the homogenous behavior of the results, within the available back-azimuthal windows. The single layer assumption has also been adopted by previous studies in the Greek region (e.g. Evangelidis et al. 2011; Paul et al. 2014).

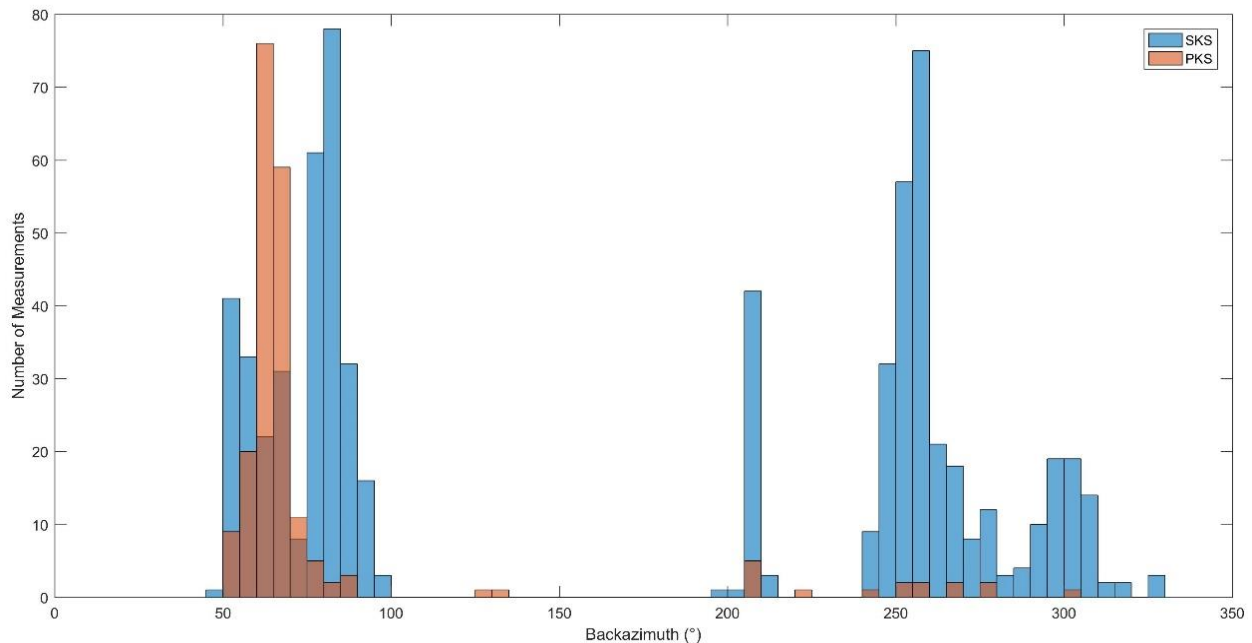


Figure 26: Back-azimuthal distribution of the successful measurements. There is a back-azimuthal gap between 100° - 200°. PKS results are mostly in the range 50°- 100°.

Although the fast polarizations directions and delay times are not uniform in the whole study area, certain patterns can be identified. In the Aegean Sea the ϕ directions present a clear NE-SW trend. They are slightly altered to NNE-SSW in the central and in the south Aegean and more specifically in the stations SMG, CHOS, APE and BLCB. The delay times smoothly decrease in the Aegean, from north to south, with the largest delay time in the LIA station (2.23 s) and the smallest in the APE station (0.80 s). The number of the available results in the specific area is satisfactory (>10 per station) and in some cases, such as the PRK station, the number of results exceeds 40. The high number of available results led to significantly low Std and error values, implying secure seismic anisotropy parameter's identification. Conspicuous behavior is presented by the BODT station, where the mean polarization direction changes to NW-SE, but with significantly smaller number of results (4), compared to other stations in the area.

In the island of Crete, the ϕ directions are in general normal to the trench with a variety of the observed parameters. In detail, in the westernmost part of the island the IMMV station presents NNE-SSW SKS and PKS polarization directions with a small mean delay time (0.78 s). In central Crete the SIVA station offers results only in PKS phases with N-S directions and with a higher mean delay time (1.25 s). The NPS station in the easternmost part shows NE-SW PKS and NW-SE SKS directions with completely different delay times in each case (0.66 s SKS - 1.15 s PKS). It is

important to point out that the stations in Crete offer smaller number of results, compared to the ones in the rest of the Greek region, fact that can be connected with the geological complexity of the area. In addition, in the vicinity of the Rhodos Transform Fault, regarding the ARG station, the polarization direction is also NE-SW parallel to the trench, with mean SKS delay time close to 1 sec. The results in south Turkey present approximately N-S SKS and PKS directions in the DALY station and NW-SE in the ELL station. Both cases present time delays close to 1 sec.

The area of Peloponnese includes four stations where seismic anisotropy measurements were performed, two in the north and two in the south. For the stations ITM and VLI only SKS results were obtained, with N-S and NW-SE directions, respectively, with satisfying number of results in each case (15-ITM, 9-VLI). In the northern part of Peloponnese (LAKA station), the directional behavior changes to NE-SW and is assimilated mostly with patterns that are present to the north. Specifically, in central Greece the stations PVO, ANX, AGG, KYMI present NE-SW ϕ directions, in an observed motif continuity that follows the Aegean's directional behavior, with the mean time delays being in the range of 0.89 – 1.66 s. Distinct exception are the stations AXAR and ATAL, where the fast polarization (close to NW-SE) differs from the area's anisotropic pattern. These stations exhibit only SKS results with seven available results in both cases.

The NW-SE is exhibited again further to the north, in the THL ($\delta t=2.21$ s) and FNA stations. More specifically, the FNA stations presents a difference between the PKS and SKS time delays and fast directions, with 1.86 s and 0.84 s respectively and a $\sim 20^\circ$ divergence. Results close to these directional and time delay observations are obtained for the stations LIT and PLG, with notable number of results (>10). In central Macedonia there is an alteration mainly in the fast polarization directions from the west to the south part, changing from NW-SE to NE-SW, forming a characteristic V shape. This alteration is sharp and is identifies between the PLG and the SOH stations. The cases of the KZN and XOR stations are peculiar, given that the high majority of the measurements are “good” and “fair” nulls. In addition, the station NEO exhibits significant number of null measurements.

Concerning western Greece, the directional behavior of the SWS results is interesting, based on their placement on the northern and on the southern Hellenides. The KEK and the JAN stations presents NNE-SSW ϕ directions, perpendicular to the subduction zone. In the vicinity of the Kefalonia Transform Fault the LKD2 station adopts an approximate N-S direction, regarding both SKS and PKS phases. However, the VLS station located few km to the southern presents a mean NEE-SWW direction, implying a rotation of the anisotropy direction (Fig. 27).

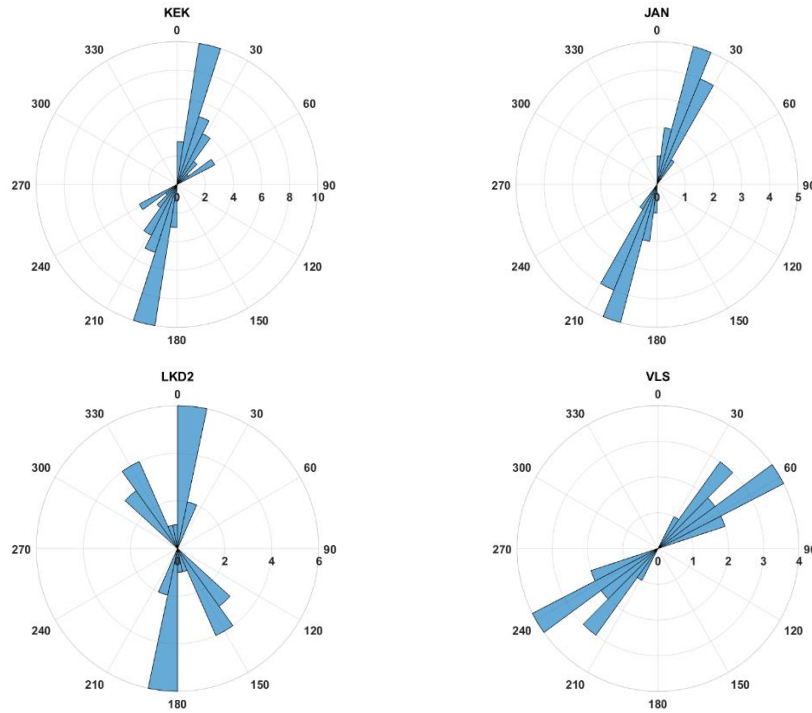


Figure 27: Rose diagrams for the KEK, JAN, LKD2 and VLS stations.

Table 1: Obtained SKS spitting parameters and calculated Standard Deviation (σ). The geographical coordinates of each station are also provided.

Station	Network	Events Analyzed	Latitude ($^{\circ}$ N)	Longitude ($^{\circ}$ E)	ϕ ($^{\circ}$ E)	σ_{ϕ} ($^{\circ}$ E)	dt (s)	σ_{dt} (s)	No of results
ATAL	HA	433	38.2401	21.9785	19.78	19.78	1.45	0.44	8
AXAR	HA	67	38.6926	23.0213	-15.09	36.91	1.17	0.76	7
LAKA	HA	143	38.7664	22.6590	-35.02	26.70	1.06	0.33	7
APE	HL	451	39.2456	26.2649	24.79	5.31	1.90	0.17	44
ARG	HL	369	41.3484	23.8651	20.71	20.71	1.21	0.36	33
IMMV	HL	432	39.8972	25.1805	27.19	15.50	2.23	0.58	32
ITM	HL	451	37.7042	26.8377	7.38	18.81	1.17	0.36	31
JAN	HL	458	40.3033	21.7820	-	-	-	-	29
KEK	HL	373	41.1450	25.5355	20.73	8.61	1.45	0.40	29
KYMI	HL	372	39.7127	19.7962	23.74	17.72	1.35	0.49	28
KZN	HL	460	37.0727	25.5230	19.86	13.05	0.80	0.30	27
LIA	HL	382	36.2135	28.1212	19.84	19.63	0.91	0.28	26
MHLO	HL	459	40.4709	25.5305	47.83	13.51	2.34	0.70	24
NEO	HL	386	37.8524	23.7942	-25.14	15.70	1.08	0.25	22
NPS	HL	371	39.6561	20.8487	16.54	18.55	0.90	0.34	22
NVR	HL	437	35.4606	23.9811	12.74	12.48	0.78	0.29	17
PLG	HL	470	37.1787	21.9252	3.83	36.89	1.25	0.86	15
PRK	HL	335	38.1768	20.5886	50.63	11.83	1.39	0.28	15
RDO	HL	423	36.6898	24.4017	15.23	26.57	1.68	0.60	14
SMG	HL	382	39.5646	22.0144	-9.93	19.91	2.21	1.23	13
SMTH	HL	336	40.3714	23.4438	-30.58	46.69	1.78	1.69	12
THL	HL	385	39.3056	23.2218	-53.13	13.51	2.40	1.78	10
VLI	HL	419	35.2613	25.6103	-24.97	51.51	0.66	0.25	9

VLS	HL	478	36.7180	22.9468	23.28	23.28	1.36	1.16	9
VLY	HL	194	38.6331	24.1001	60.21	14.51	1.66	0.28	5
ANX	HP	284	38.6167	21.5259	13.76	38.39	1.09	0.26	8
LTK	HP	192	38.5933	21.9202	21.09	11.53	0.89	0.42	7
PVO	HP	370	38.0228	22.9673	-37.88	5.44	1.03	0.30	4
AGG	HT	409	40.8957	26.0497	10.75	10.75	1.49	0.33	32
ALN	HT	414	38.3868	26.0506	5.15	5.15	1.97	0.42	19
CHOS	HT	393	38.7889	20.6578	21.03	21.03	2.03	0.28	17
FNA	HT	428	39.3660	23.1920	-	-	-	-	15
LIT	HT	393	40.1003	22.4893	-44.41	22.12	1.39	0.64	10
LKD2	HT	410	39.9363	23.6768	13.28	13.28	0.69	0.11	9
PAIG	HT	377	40.7818	21.3835	-49.43	23.67	0.84	0.20	8
SOH	HT	433	40.8206	23.3556	15.67	47.47	1.51	1.32	6
XOR	HT	408	39.0211	22.33600	14.56	14.56	1.43	0.13	4
AYDB	KO	184	40.6708	26.5132	22.44	2.99	1.77	0.22	18
BLCB	KO	179	38.3853	27.0420	20.06	32.98	1.17	0.42	11
BODT	KO	411	36.8162	28.6532	0.20	16.13	1.18	0.24	9
DALY	KO	204	40.3980	26.4742	30.62	3.30	1.91	0.28	8
ELL	KO	350	36.7483	29.9085	-16.32	7.47	1.04	0.10	7
ERIK	KO	169	40.3703	26.7593	36.61	4.19	1.57	0.28	7
GELI	KO	316	37.9467	27.8908	7.74	7.75	1.45	0.80	5
LAP	KO	322	37.0622	27.3103	-9.76	21.65	1.62	0.19	4

Table 2: Obtained PKS spitting parameters and calculated Standard Deviation (σ) for each station. The geographical coordinates of each station are also provided.

Station	Network	Events Analyzed	Latitude ($^{\circ}$ N)	Longitude ($^{\circ}$ E)	ϕ ($^{\circ}$ E)	σ_{ϕ} ($^{\circ}$ E)	dt (s)	σ_{dt} (s)	Number of results
LAKA	HA	115	35.0178	24.8102	-1.56	0.06	1.25	0.07	2
APE	HL	127	35.2613	25.6103	20.74	23.99	1.15	0.51	3
ARG	HL	134	35.4606	23.9811	26.80	20.28	0.81	0.23	6
IMMV	HL	126	36.2135	28.1212	19.11	12.96	1.16	0.21	14
JAN	HL	111	36.8162	28.6532	6.37	10.06	1.61	0.38	4
KEK	HL	142	37.0727	25.5230	13.37	17.93	1.04	0.26	7
KYMI	HL	136	37.7042	26.8377	8.72	7.24	1.17	0.20	18
LIA	HL	130	37.8524	23.7942	1.76	15.84	1.19	0.25	13
NEO	HL	102	37.9467	27.8908	14.54	10.17	0.72	0.18	3
NPS	HL	126	38.0228	22.9673	-5.01	3.40	1.29	0.11	5
PRK	HL	139	38.2401	21.9785	31.27	13.29	1.44	0.42	3
RDO	HL	60	38.3853	27.0420	5.42	1.24	2.00	0.12	3
SIVA	HL	127	38.3868	26.0506	8.86	6.19	1.93	0.21	4
SMG	HL	99	38.5933	21.9202	23.49	8.09	1.12	0.12	6
SMTH	HL	89	38.6167	21.5259	20.35	19.4	1.34	0.03	2
VLY	HL	56	38.6331	24.1001	48.56	2.76	1.77	0.10	2
ANX	HP	122	38.7889	20.6578	-4.03	7.05	1.40	0.29	6
LTK	HP	121	39.0211	22.3360	35.38	8.17	1.77	0.51	9
PVO	HP	141	39.2456	26.2649	29.98	4.54	2.21	0.18	10
AGG	HT	135	39.3056	23.2218	37.10	39.96	1.22	0.45	3
ALN	HT	126	39.6561	20.8487	20.13	7.00	1.02	0.31	13

CHOS	HT	123	39.7127	19.7962	22.72	6.08	1.84	0.17	9
FNA	HT	133	39.8972	25.1805	18.84	4.5	2.28	0.29	8
LKD2	HT	73	40.3980	26.4742	24.53	3.30	2.49	0.16	3
AYDB	KO	151	40.4709	25.5305	27.34	6.32	1.93	0.51	8
BLCB	KO	69	40.6708	26.5132	19.35	2.52	2.10	0.34	5
DALY	KO	108	40.7818	21.3835	-17.29	4.28	1.86	0.48	7
ERIK	KO	144	40.8957	26.0497	6.06	6.62	1.94	0.36	9
GELI	KO	145	41.1450	25.5355	16.72	6.69	1.79	0.46	17

In most cases, the SKS and the PKS phases provide similar SWS values regarding the determined shear-wave splitting parameters. The latter is justified by the almost identical up-going ray paths that they follow. The results of the fast polarization directions obtained by the analysis of the SKS and PKS phases differ significantly in the VLY and LTK stations, as evident in each station analytical plots that are presented in Figure 28.

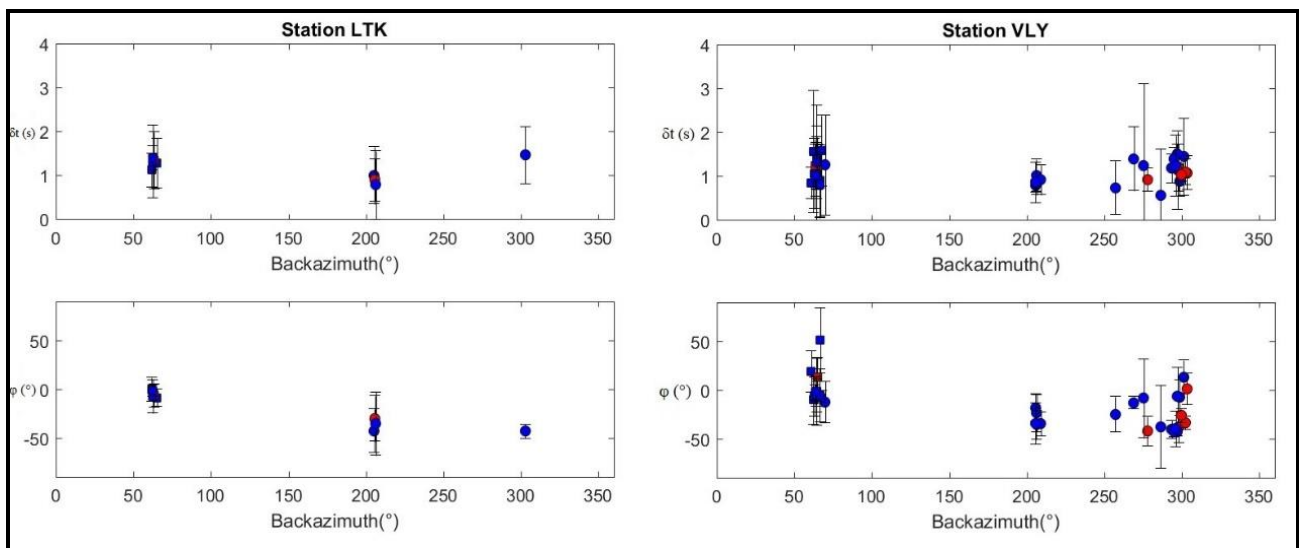


Figure 28: Analytical plots for the stations VLY and LTK, with the variations of delay times (a) and fast polarization-phi (b) compared to the back-azimuth. The circles depict the SKS and the squares the PKS results. The red color represents “good” and the blue for “fair” results.

2.7 Discussion

A major issue that needs to be resolved is the depth identification of the origin of seismic anisotropy, i.e. lithospheric, mantle lithospheric or asthenospheric. The latter will facilitate assessing the geodynamical interpretation of the determined SWS results. Generally, core phases (SKS/PKS/SKKS) that are usually incorporated in SWS studies offer poor analysis of the anisotropy distribution in depth, given the path-integrated nature of SWS results. This means that measurements performed on surface stations contain an accumulation of splitting information, which is acquired due to shear-waves propagating in the mantle and crust.

For the vast majority of cases, shallow anisotropic sources have been identified in the upper crust. In general, for the latter part of the Earth's interior, it is reported that the magnitude of anisotropy, defined by time-delay values, ranges between 2% and 4% (Barruol and Mainprice 1993). Endrun et al. (2011) determined lower crustal azimuthal anisotropy of around 1.8% regarding the North and 3.5% the Central and South Aegean Sea. On the other hand, according to their results regarding the lithospheric mantle, the azimuthal anisotropy is approximately 2% in the North and quite smaller (<1%) in the Central-South Aegean.

To estimate the expected theoretical time-delay (dt_T) from the source-receiver distance (r) we solve the equation of Wüstefeld et al. (2010) for dt_T :

$$A = \frac{V_{smean} * dt_T * 100}{r} \Rightarrow dt_T = \frac{A * r}{V_{smean} * 100}$$

where r is the source-receiver distance, V_{smean} a mean S-wave velocity and A the magnitude of anisotropy.

The crustal thickness in the Greek region ranges between 25-50 km, with the highest values in W. Greece (Karagianni et al. 2005; Mutlu and Karabulut 2011). Considering the largest source-receiver distance as the deepest crustal depth (50 km), the largest magnitude of anisotropy for Greece from literature (3.5%) and a V_{smean} value equal to 4.0 km/s, the maximum theoretical time-delay attributable to the crust is found equal to 0.44 s. Reliable results from local upper crust anisotropy studies for the Gulf of Corinth (Kapetanidis et al. 2015) present δt values in the range up to 0.19 s (Papadimitriou et al. 1999; Kaviris 2015; Kaviris et al. 2017; Kaviris 2018), consistent with the above values. The presence of a low velocity zone in the Aegean (e.g. Drakatos et al 1997; Karagianni et al. 2005; Salaün et al. 2012) is a sign of a thin lithosphere that cannot significantly contribute to the anisotropic observations, as also indicated by Paul et al. (2014). The Aegean Lithospheric-Asthenospheric boundary indeed can be placed conservatively in some cases in 40-50 km depths (Endrun et al. 2008), in contradiction to the results of Sodoudi et al. (2006) who suggest that the Aegean and African Lithosphere-Asthenosphere boundary can be traced in depths greater than 100 km. In either case, the lithosphere cannot offer the necessary circumstances in order to be considered the anisotropy source, taking into account that the average delay times in some cases, especially in northern Greece, exceed 2.0 s. Savage (1999) suggests that time delays that exceed 0.2-0.3 s are possibly related to upper mantle sources of anisotropy.

Anisotropy in the Aegean Sea is considered uniform. Regarding north Aegean and NW Turkey, SKS/PKS fast polarizations directions are approximately NE-SW and trench-normal, with time-delays that exceed 2.0 s. This trend changes to more NNE-SSW in the Central and the South Aegean, with a smooth decrease that reaches 1.0 s, in the values of time-delays. The latter results are consistent with the ones by Paul et al. (2014) and Confal et al. (2016), who have densely covered the North and the Central/South Aegean, respectively. A uniform pattern in North Aegean and NW Turkey is evident, based on these studies (Fig. 29).

Hatzfeld et al. (2001) first proposed the anisotropic nature of the lithosphere and possibly the asthenosphere in North Aegean. As it has already been mentioned, the high time-delay values in North Aegean (> 2.0 s) support the hypothesis of an anisotropic asthenosphere source. The smooth decrease in the delay times from the North Aegean towards the trench seems to support the suggestion of Evangelidis et al. (2011) that the observed anisotropy is caused by the mantle wedge flow. This decrease of time-delay values can be attributed to the reduction of the anisotropic material thickness from the North to the South Aegean, fact also supported by tomographic results regarding the mantle wedge (Piromallo and Morelli 2003). The determined time-delay observations are similar to the ones previously obtained in the area (e.g. Paul et al. 2014; Confal et al. 2016), with the exception of the study by Evangelidis et al. (2011), where delay time values are significantly smaller, as Confal et al. (2016) also noticed.

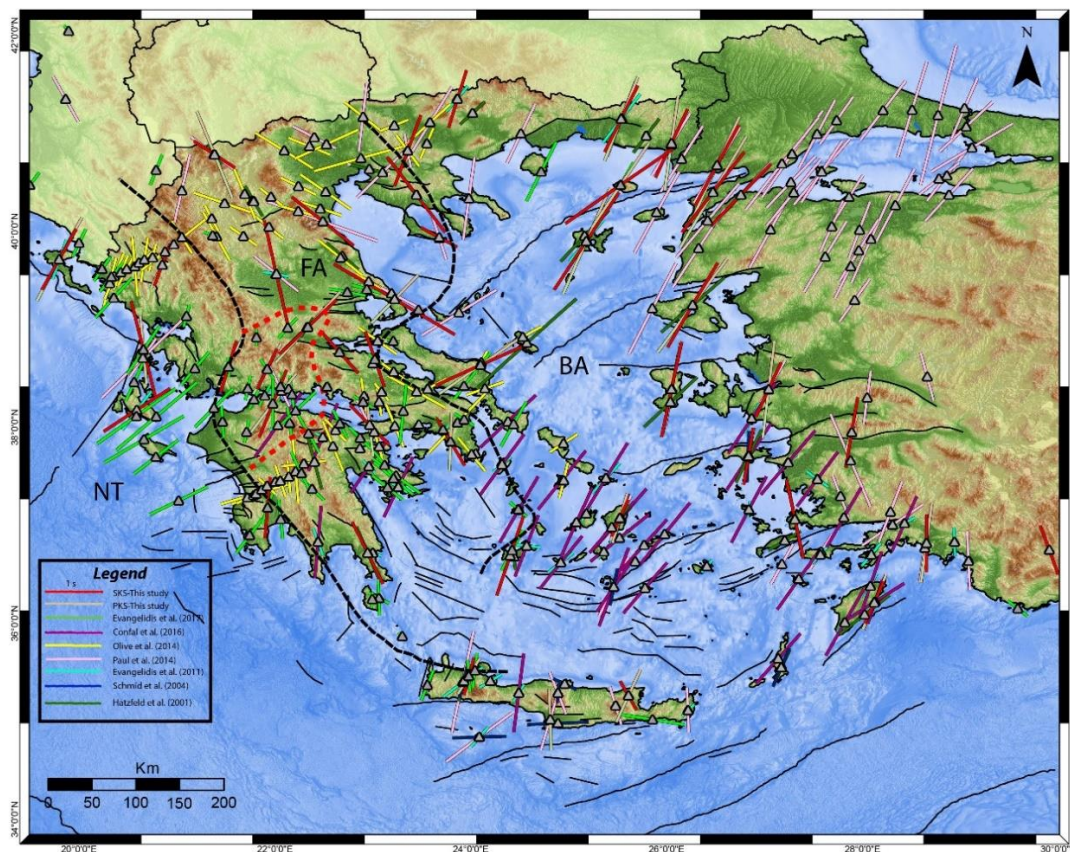


Figure 29: Station-averaged splitting results from the available SWS analysis studies in the Greek region by Hatzfeld et al. (2001), Schmid et al. (2004), Evangelidis et al. (2011), Olive et al. (2014), Paul et al. (2014), Confal et al. (2016), Evangelidis (2017) and the current study. The mean values at each station are represented with a different color for each study and indicate the fast direction (ϕ) and the time-delay (dt). The three anisotropic zones, according to Evangelidis (2017), are superimposed.

The principal idea related to the investigation of anisotropy directions is that they reflect asthenospheric flow and can be considered as an approximation to deduce the orientation of deformation regarding the upper mantle. Adopting this assumption, the flow of asthenosphere in the Aegean and NW Turkey exhibits almost constant NE-SW direction, turning to NNE-SSW in the Central Aegean.

The comparison between the SWS measurements and crustal deformation is a useful tool to evaluate the existence of a possible coupling/decoupling among the crust and the mantle. Figure 30 presents the obtained SKS/PKS results, superimposed by GPS velocity data, which reveal a counterclockwise rotational flow in the Middle East and Aegean regions, attributed to slab roll-back (Le Pichon and Kreemer 2010). However, the fast polarization directions are not consistent with the GPS results for the major part of the Greek region, with a possible exception in the south Aegean (Cyclades), where GPS and SKS/PKS results provide similar directions (Fig. 30). This phenomenon can be attributed to the thinner lithosphere in the central and southern Aegean (Karagianni et al. 2005; Salaün et al. 2012). Menant et al. (2016) investigated mantle flow in E. Mediterranean with 3D numerical modelling and suggested that the transmission is facilitated by the lithosphere which is thinner in the extensional domain. In addition, the fast polarization directions do not follow neither the strain rates directions, which trend ~N-S in the Aegean (Müller et al. 2013), nor the strike of the NAF, which is the major tectonic structure in the area.

Jolivet et al. (2013) proposed a strong decoupling of the mantle and crust, resulting in movement of the crust parallel to the CHSZ and to the NAF. This may explain the fact that anisotropy directions cannot trace the NAF, as well as the differences between the SKS/PKS and GPS directions. Even if the lithospheric extent of the NAF is still debated (Biryol et al. 2011; Salaün et al. 2012), it is almost certain that the NAF does not reach the depth of the anisotropic source. Mutlu and Karabulut (2011) performed an anisotropic Pn tomography study and traced a similar trend to the one obtained by SKS phases beneath the Aegean Sea, just below the Moho discontinuity. Endrun et al. (2011) revealed an N-S trend in the north Aegean and weaker anisotropy in the Cyclades. All the above suggest that, apart from the one between the lithospheric and the asthenospheric mantle, there is another differential contact zone among the lower crust and the uppermost part of the mantle, as Jolivet et al. (2013) claim. Therefore, the strict characterization of a specific decoupling zone is venturesome, due to the possible existence of more than one partly or strongly coupling/decoupling zones. Numerical modelling studies (Sternai et al. 2014; Menant et al. 2016) favor a lithosphere/asthenosphere coupling and that the strain in some extent is controlled by the asthenospheric flow. However, the shape of the asthenospheric flow does not seem to have a clear connection with the form of the crustal flow, implying a completely independent behavior.

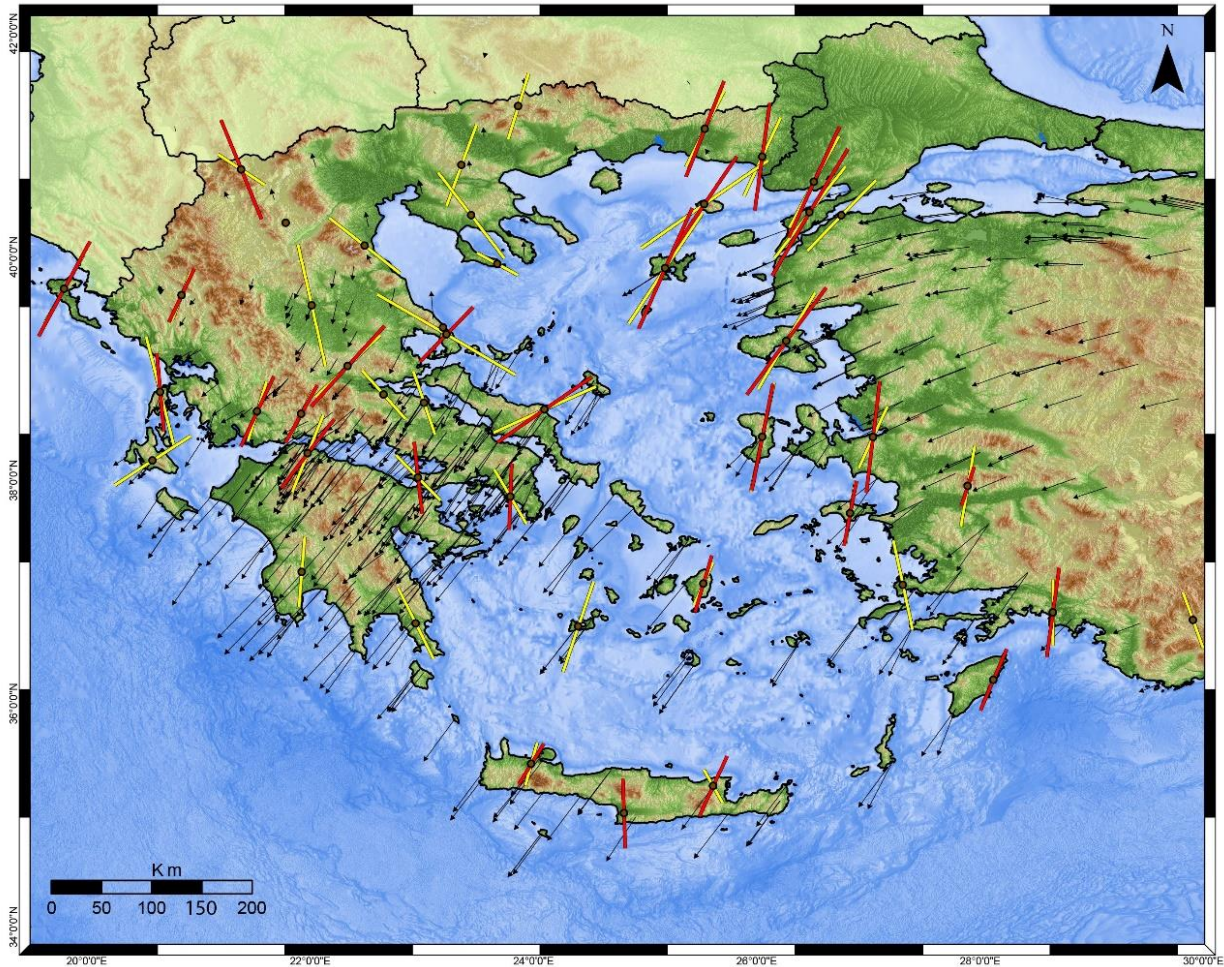


Figure 30: Station-averaged splitting results from the present SWS analysis, superimposed with GPS displacements vectors (Nyst and Thatcher 2004; Reilinger et al. 2006; Floyd et al. 2010; Chousianitis et al. 2013).

Three zones of anisotropic behavior in the Greek region, also adopted by Evangelidis (2017), were considered by Olive et al. (2014). The first (Fig. 29) is the near trench (NT) zone which is characterized by trench normal fast directions, the second one is the fore-arc (FA) domain with trench parallel directions and the third one is the back-arc (BA), where the Aegean Sea belongs, with also present oblique anisotropy directions. The specific zonation type in the Hellenic system is obvious and it is even more distinguishable when all available data in the Greek region are utilized (Fig. 29). The greater part of mainland Greece belongs to the FA domain with a general trend of fast parallel directions.

It is worth noting that most subduction zones worldwide are characterized by trench parallel anisotropy directions (Long and Silver 2008), except Cascadia (e.g. Currie et al. 2004) and the Hellenic subduction, with spatially stable trench normal directions in the near trench area. The main question in this case is whether the anisotropic signature in the NT originates from slab or sub-slab sources. Long and Silver (2008), who studied subduction systems globally, found no relation between slab age and thickness versus time-delays. The latter is a sign that the contribution of the slab is not primary, and the authors suggest that the observed signal has sub-slab sources with an entrained A-type LPO that is appropriate for the subduction system physical conditions. This simple type of active mantle flow is even supported by the numerical models of Faccenda and Capitanio (2013) that proposed an upper and a lower fabric domain with trench normal and trench parallel

directions, respectively. This A-type assumption is also valid for the BA region that exhibits the same behavior.

Exceptions regarding the trench normal behavior were identified in two parts, the eastern and the western, of the subduction zone. Regarding the eastern one, between E. Crete and the southwestern coasts of Turkey, close to Kos and Rhodes Islands, the fast polarization directions diverge from the trench normal pattern and convert to trench parallel. Similar behavior has also been identified by previous SKS studies for the same region (Olive et al. 2014; Evangelidis 2017), contradicting to a certain extent the previous A-type assumption for the NT area. The existence of slab tearing in the eastern Aegean is still debated, although an increasingly number of publications are in favor of the existence of a tear (Berk Biryol et al. 2011; Salaün et al. 2012). Superimposing the full dataset of SKS/PKS results for the area with the proposed slab tear geometry in E. Aegean, according to Bocchini et al. (2018), a specific pattern of asthenospheric flow can possibly be identified (Fig. 31). The trench parallel directions appear to go across the possible slab tear, indicating an escape of the asthenospheric flow towards the mantle wedge, imaging a toroidal flow that initiates from the eastern edge of the slab.

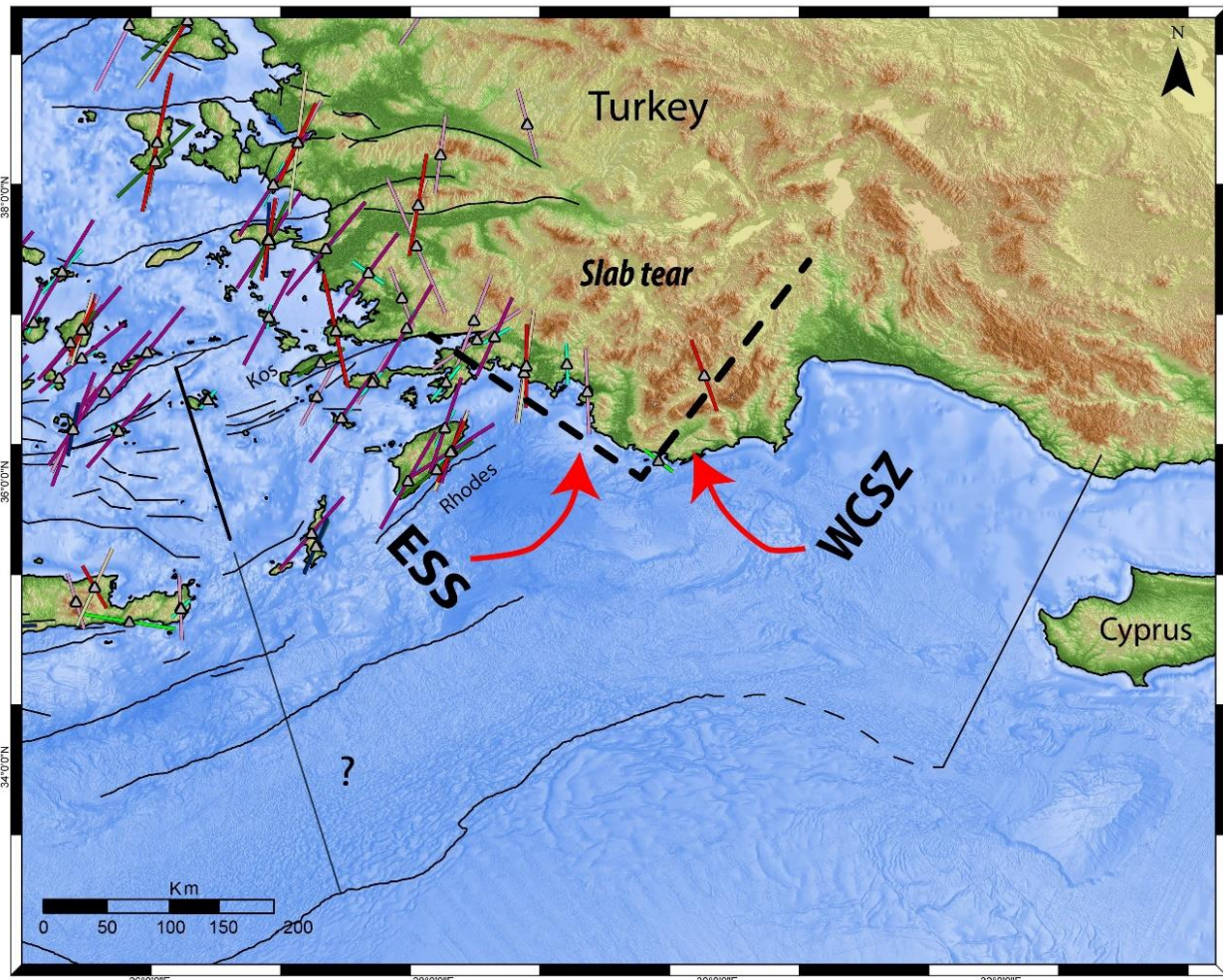


Figure 31: Proposed asthenospheric flow based on SWS results. Dotted lines indicate observed earthquake distribution discontinuities and continuous lines the boundaries between the western and eastern slab segments by Bocchini et al. (2018). WCSZ: Western Cyprus Subduction Zone; ESS: Eastern Slab Segment.

Faccenda and Capitanio (2013) concluded, through numerical modelling, that there is a possible trench-parallel core beneath the trench-normal fabric in the sub-slab area and that the lower fabric can be better expressed in the near edge areas. The proposed model satisfactory fits the results of the present study, especially in East Aegean, and could justify the observed trench parallel direction in the FA area. The nature and the behavior of this trench parallel core is debated due to the trench normal source-side directions (Evangelidis 2017). Nevertheless, source-side measurements, especially the ones with larger time-delays, could sample deeper regions compared to SKS. Thus, even an alteration of cores with different fabric behaviors is possible.

Trench parallel anisotropy directions can be produced by petrological conditions. Olive et al. (2014) proposed, aiming to interpret the directions in the FA zone, the existence of a thin serpentinitized layer above the subducted slab with a trench normal shear direction, instead of using more classical models (Jung and Karato 2001; Kneller and Van Keken 2008; Long and Silver 2009). These models, in contrast with the one of Olive et al. (2014), could not explain the lack of correlation in the FA region between the mantle wedge thickness and time-delay values. In addition, Evangelidis (2017), studying the fore-arc area, suggests that the observed trench parallel pattern has sub-slab origin (due to similar source-side splitting pattern) and that it is possibly created by a trench parallel sub-slab mantle flow.

The fore-arc domain exhibits time delay values of ~ 1.0 s and, thus, it is quite difficult to approximate the depth of the anisotropic source (sub or supra slab) based only on this characteristic. Following the thoughts of Olive et al. (2014), a thin layer of serpentine could produce these values of time-delays, given that, according to Jung (2011), it is a highly anisotropic mineral and can be formed if the mantle wedge is hydrated. It is certain, however, that a serpentine layer is not dominant beneath Greece. Regarding Peloponnese, the identification of a weak velocity contrast above the mantle wedge revealed impalpable signs of serpentinitization (Pearce et al. 2012). Halpaap et al. (2018) found small V_p/V_s values for the lower overriding crust-mantle wedge's cold corner, results that cannot be related to serpentines that present high V_p/V_s values. Halpaap et al. (2018) also noticed that the determined P velocities (higher than 8 km/s) are typical for mantle peridotites, also indicating dry mantle wedge corner. Abers et al. (2017) also support the dry nature of the Hellenic mantle wedge. All the above indicate that the existence of a serpentine layer of sufficient thickness as a source of anisotropy is highly unlikely and are in favor of an anisotropic signature that is originated in the sub-slab area.

Interpreting SWS considering a petrological aspect, the B-type consists the sole olivine fabric that can immensely change the connection of the mantle flow and the SWS observations (Jung and Karato 2001). The latter type is connected with high water level contents, high stresses and low temperatures (Karato 2008). B-type olivine may explain in mantle wedge terms the tilt from the trench normal (BA) to trench parallel (FA) and back to trench normal (NT) directions. However, the existence of an extensive B-type fabric in the Hellenic mantle wedge cannot be feasible, considering its dry nature. As a result, the hypothesis of an asthenospheric or petrological flow change above the slab is not highly possible.

Regarding the western part of the subduction and specifically in the broader region near the KTF, there is another observable deviation from the directions that are perpendicular to the trench. The fast directions remain constantly trench oblique to the north, regarding the JAN and KEK stations that are installed in the continental part of the subduction system. Near the KTF, the stations LKD2, in Lefkada, and VLS, in Kefalonia, demonstrate a clockwise rotation that becomes sub-parallel to the KTF. In order to acquire a better picture of the variation of the SWS parameters, all

measurements were projected to the ray piercing point in 200 km depth, considered as an average value of the expected anisotropic layer from literature (Savage 1999) and our observations. This projection offers a comprehensive view of the SWS measurements in the area dominated by the KTF, revealing a rotation of anisotropy directions from the northern to the southern segment.

The geometry of the Western Hellenic Subduction Zone (WHSZ) and the transition between these two segments, presented in Figure 32, are still debated and have been a scientific topic of intense investigation. Suckale et al. (2009) propose a trench-normal tear in the boundary of the oceanic and continental lithosphere that can cause an influx of the flow material in the mantle wedge. Royden and Papanikolaou (2011) are also in favor of the existence of segments in the WHSZ, in the KTF area, that results to dextral strike-slip movement. Pearce et al. (2012) suggest that a smooth ramp can be considered as the transition between the two segments, not fully rejecting though the tearing. However, Halpaap et al. (2018) propose the existence of a slab which is smoothly deformed. On the other hand, Guillaume et al. (2013) support the hypothesis of a tear fault, which is not fully subducted, with a newly formed tear window. According to our results, the SKS and PKS anisotropy directions indicate the possible existence of a toroidal cell (Fig. 32), initiating from the northern KTF segment. The existence of the toroidal cell presupposes the occurrence of a slab window, as initially proposed by Govers and Wortel (2005), but the age and the development condition of the tear cannot be approached by a SWS splitting study.

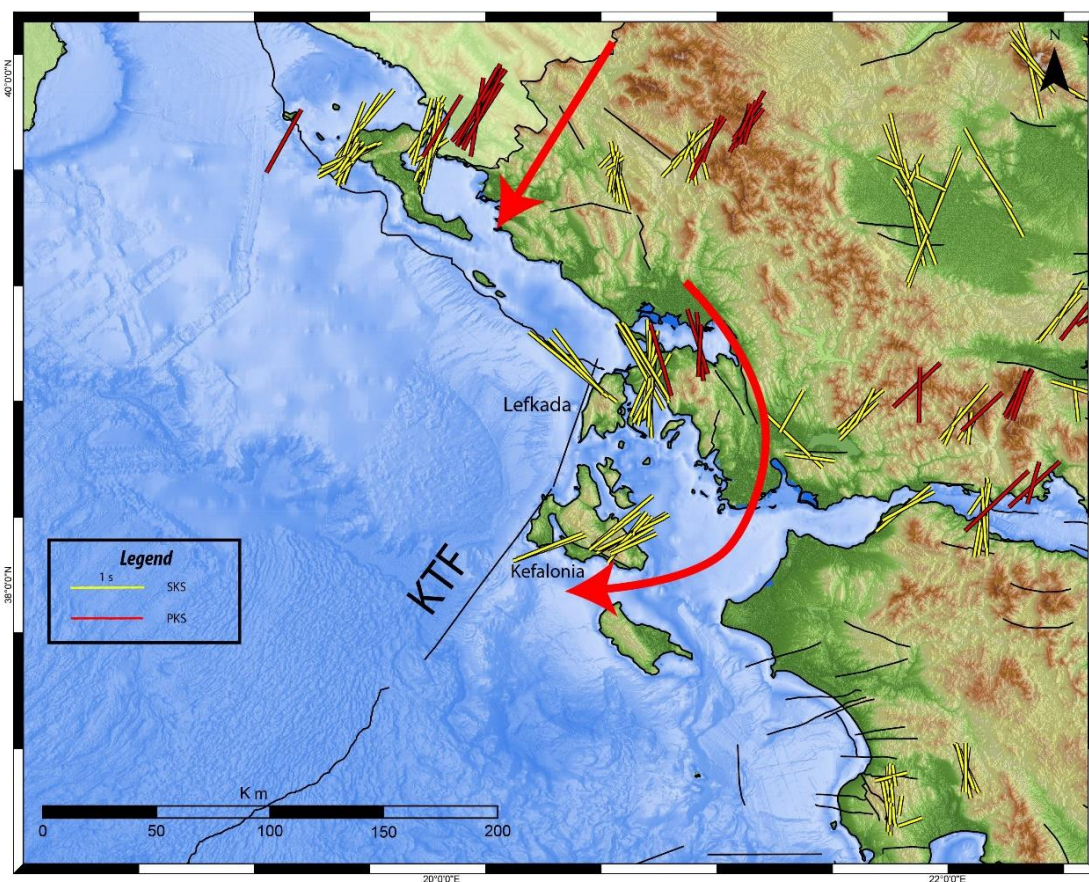


Figure 32: Map of SWS results at 200 km depth in the Western Hellenic Subduction Zone. Red arrows indicate the proposed asthenospheric flow.

There is no doubt that the upper mantle in the Greek region is in general highly anisotropic. However, SWS results obtained for certain stations indicate a completely different behavior with high number of null measurements. More specifically, stations KZN and XOR present exclusively null results, whereas the PLG and NEO stations also present significant number of nulls, compared to the total available results.

In general, nulls are identified if the shear wave (SKS/PKS) is not split. The lack of splitting can be attributed to various factors, such as fossil anisotropy, complex anisotropy and deformation in the lithospheric part of the mantle (Barruol et al. 1997). Regarding the KZN and XOR stations, the absence of seismic anisotropy is observed in all the available backazimuths, thus it is considered as relatively constrained. The latter leads to the rejection of the hypothesis that null measurements result from the parallelization of the initial polarization with the one caused by the anisotropic medium. Moreover, due to the backazimuthal gaps, we are not able to identify variations of the anisotropic parameters, which would be interpreted with the presence of two or more anisotropic layers. Stations that yield high number of null measurements are very close to the boundaries of the FA and the BA zone. Thus, assuming a simple asthenospheric flow, the stations related to null measurements can possibly be located on a transition zone between the FA and BA zones. Nevertheless, this assumption cannot be verified, due to lack of backazimuthal coverage. Another exception regarding the proposed zonation by Evangelidis (2017) is Central Greece and northern Peloponnese, where the polarization directions are trench parallel instead of trench normal. This area constitutes the transition from the northern to the southern Hellenides, possibly influencing the anisotropic signature due to the transition from the NT to the FA, or due to the slab window that is responsible for the inflow of material originating from the asthenosphere.

Chapter 3: P-Receiver Functions

2.1 Introduction

One of the most important quests in modern Seismology is the understanding of the Earth's interior, by using techniques that exploit information occurring "inside" the wave phases. In the previous chapter, the SKS and PKS phases were used in order to approach the kinematic behavior of the upper mantle in the Greek region, via a seismic anisotropy study. In the current chapter the Receiver Functions technique (from now RF) will be applied, for the purpose of the more thorough examination of the Earth's interior structure. The RF technique will be analyzed in more detail later in this chapter but from now we can set RF as time series that contain plethora of information regarding the Earth's structure beneath the recording station.

It is known from the Wave theory that when a wave is passing through a discontinuity inside the Earth, a wave conversion, among other phenomena, occurs. The type and the status of this conversion depends on the velocity contrast around the layer boundary. As a result, when a P or S wave plane strikes an interface along with the refraction/reflection, P to S or S to P conversion exists. Figure 33 presents a cartoon that imprints the ray propagation near the Moho boundary. The P plane wave strikes the layer boundary and produces a plethora of phase conversions. For the specific Moho example it is apparent that the Pp phase is recorded first in the seismograph, given that the P wave travels faster than the S, after that the Ps phase follows and then the other multiples.

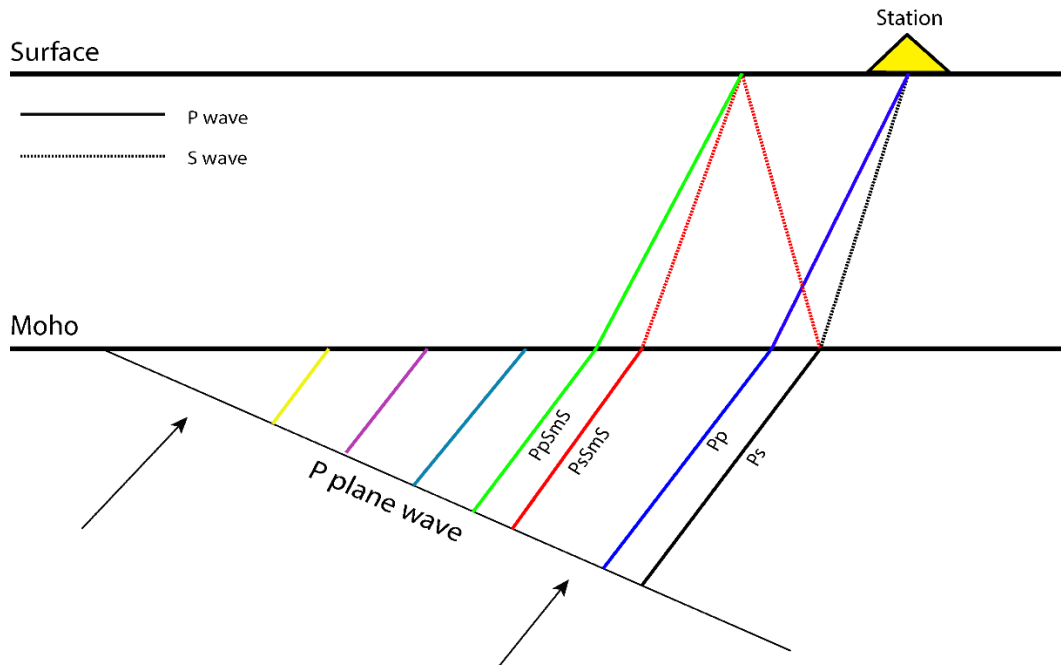


Figure 33: Ray diagram that represents the wave propagation phenomena near a layer boundary (Moho). Continuous lines represent the P waves and the dashed line the S waves. The "m" symbol concerns rays that have been reflected in the Moho discontinuity.

Vinnik's (1977) pioneer study was one of the first efforts to determine the depth of discontinuities, in the specific case within the mantle, based on the wave conversions that are produced. This thought has also been exploited previously by Phinney (1964), where a primal form of RF, using long-period P waves from distant earthquakes, was generated. Since Phinney's and Vinnik's studies, the determination of velocity boundaries inside the Earth using RF has been evolved to a great extent. Nowadays, the RF technique is one the most popular scientific tools, in order to study geodynamical and geological problems in general.

3.2 Receiver Functions theory

3.2.1 Rotation-Deconvolution

Receiver Functions (RF) are time series (or waveforms) that illustrate the response of the ground beneath the receiver. The response is originated from the wave propagation beneath the station, as previously described (Fig. 33). The computation of the RFs includes several steps that will be analyzed in this chapter.

The first vital step for the computation of the RF is the rotation of the components. The original instrument recordings are oriented in the ZNE (Vertical, North, East) coordinate system. The nature of this system does not allow a satisfying isolation of separate phases in each component, due to the fact that the system is not aligned with the station-earthquake axis. In order to isolate the energy of different phases in separate components, the rotation to another coordinate system is necessary. The most common system for rotation is the ZRT (Vertical, Radial, Tangential) local coordinate system (Fig. 34). For this purpose, a matrix multiplication will be applied:

$$A = \begin{bmatrix} \cos\varphi & \sin\varphi \\ -\sin\varphi & \cos\varphi \end{bmatrix}$$

Then we have

$$\begin{bmatrix} R \\ T \end{bmatrix} = A \cdot \begin{bmatrix} N \\ E \end{bmatrix}$$

In the rotation procedure the vertical component (Z) remains the same and the energy from the P-SV waves is mixed between the Z and the R components to a variable degree. The T component contains energy only from the SH waves. The back-azimuth of the incoming wave is the parameter φ . Another rotation that is commonly used is to the LQT (Latitudinal, SV direction, SH direction) system, but the knowledge of the incident angle of the wave is necessary.

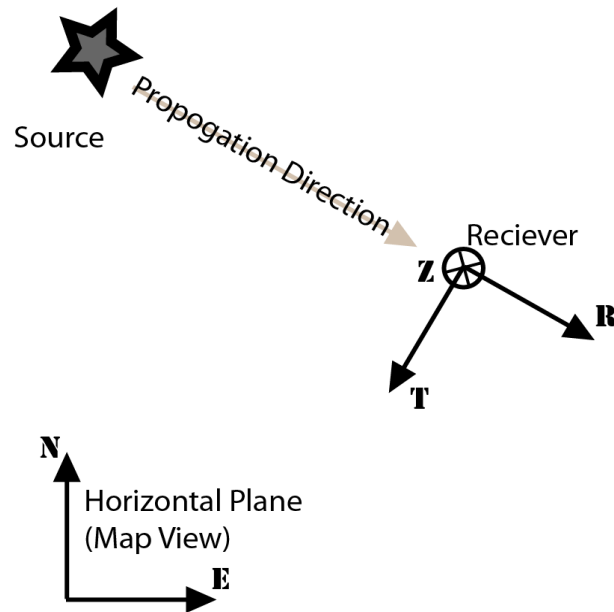


Figure 34: ZRT local coordination system and the relation between the propagation direction and the orientation of the components (Courtesy of IRIS).

The rotation is a vital part of the RF procedure in order to better isolate the energy of each phase. However, the most important step is the deconvolution process. The latter aims to reverse the effects of the convolution on the records, i.e. to remove parts of the recorded signal that do not contain important information regarding the structure. For the RF studies the deconvolution technique can be executed either in the frequency or in the time domain. As it was mentioned previously, Phinney (1964) was the first that produced a primal form of RF in the frequency domain. After that, Clayton and Wiggins (1976) also applied deconvolution in the frequency domain, introducing for the first time a minimum allowable threshold (Waterlevel) for the amplitude of the source, aiming to reduce the noise in the components and the errors, stabilizing the deconvolution procedure. Langston (1979) introduced a “P wave equalization procedure”, aiming to the removal of the source and propagation effects on the signal, using the deconvolution in a more “practical” way.

According to Langston (1979), an incoming to the station P wave plane generates a theoretical response (displacement). For example, the displacement can be characterized as “X” and is given by the functions:

$$X_Z(t) = I(t) * S(t) * E_Z(t)$$

$$X_R(t) = I(t) * S(t) * E_R(t)$$

$$X_T(t) = I(t) * S(t) * E_T(t),$$

where $I(t)$ is the instrument response, $S(t)$ the source time function and $E(t)$ the structure response in each of the components (Vertical, Radial and Tangential).

Langston (1979) noticed that the steeply incident P waves cause minor arrivals of conversions in the vertical component. Thus, the source function can be approximated by the relation $X_Z \approx S(t) * I(t)$. Moving into the frequency domain with Fourier transformation:

$$X_Z(\omega) = I(\omega) * S(\omega) * E_Z(\omega)$$

$$X_R(\omega) = I(\omega) * S(\omega) * E_R(\omega)$$

$$X_T(\omega) = I(\omega) * S(\omega) * E_T(\omega)$$

Assuming that $X_Z(t)$ behaves like a Dirac function and the instrument response is the same in all components, it is possible to determine the structural response with a simple division, producing the RF:

$$RF_R = \frac{X_R(\omega)}{X_Z(\omega)} = \frac{E_R(\omega)}{E_Z(\omega)} \quad (3.1)$$

Given the fact that $E_Z(\omega) \approx \delta(t)$ (Dirac delta function), then $RF_R \approx E_R(\omega)$. In this way, the Radial receiver function (RF_R) is generated (retransforming back to the time domain), containing information regarding the structural response from the Radial component. The characterization as “source equalization procedure” is totally justified by the fact that the source effects are completely removed by the signal by applying this method. In the same way, it is possible to acquire the tangential receiver function $RF \approx E_T(\omega)$. Trying to avoid division with a small number, Langston (1979) modified the (3.1) relation by importing the Waterlevel threshold by Clayton and Wiggins (1976). Rewriting the (3.1):

$$RF_R(\omega) = \frac{X_R(\omega)\bar{X}_Z(\omega)}{\varphi(\omega)},$$

where $\varphi(\omega) = \max\{X_R(\omega)\bar{X}_Z(\omega), c \max[X_R(\omega)\bar{X}_Z(\omega)]\}$ with c being the Waterlevel parameter.

In addition, a Gaussian filter is applied to reduce the high frequency noise effects in the RF:

$$RF_R(\omega) = \frac{X_R(\omega)\bar{X}_Z(\omega)}{\varphi(\omega)} G(\omega),$$

where $G(\omega) = \xi e^{\frac{-\omega^2}{4a^2}}$, with a being the width of the Gaussian pulse.

Except from the deconvolution in the frequency domain, this procedure can also be executed in the time domain. In the present study, the Iterative deconvolution will be applied. The latter is a technique for the computation of the RF, proposed by Ligorria and Ammon (1999). The mathematical basis for this method was adopted by Kikuchi and Kanamori (1982). Regarding the

Iterative deconvolution, the vertical component is cross-correlated with the radial component in order to estimate the lag of the first and largest spike in the RF. Following, the estimated RF is convoluted with the vertical component seismogram and is subtracted by the radial component. This procedure is repeated to determine time lag and amplitudes of other phases as well. The final iteration produces the complete form of the RF. These iteration (i) steps are briefly presented below:

1. Cross-correlation between the radial ($R^{(i-1)}$) and the vertical component (R^0 the original radial).
2. Determination of the time t_i in the cross-correlogram, for which the amplitude a_i' is maximum
3. Trace the coefficient a_i that minimize the: $C = |R^{(i)} - a_i Z * \delta(t - t_i)|^2$, where Z=vertical component, R=radial component, $\delta(t - t_i)$ time shift, * convolution and $a_i = a_i' / (Z.Z)$.
4. Addition of Dirac delta function of amplitude a_i at t_i time to the receiver function.
5. Calculation of the residual between the current and the previous form of the radial component: $R^{(i)} = R^{(i-1)} - a_i Z * \delta(t - t_i)$. Next iteration of the process.

In this method the RF is a linear combination between a Dirac delta function $\delta(t)$ that is shifted in time. Thus, the RF can be rewritten mathematically as: $RF = \sum_{i=1}^n a_i \delta(t - t_i)$.

3.2.2 Depth evaluation

The computed radial RF reveals the arrival times of a variety of phases based on the value of the amplitude. However, the acquired information concerns only the time. In order to “translate” the RF info into valuable results, the exact depth where the refraction occurs should be identified. As it was mentioned earlier, the velocity contrast near the Moho boundary causes P to S conversions. The most important conversion is the Ps phase that follows the P wave and in most cases is the signal with the largest amplitude after the P. Thus, in an ideal case of a RF, the Ps phase and its multiples (PpPs and PpSs+PsPs) should be clear and easy to identify in the signal. Based on that thought, Zhu and Kanamori (2000) created a stacking algorithm that computes the crustal thickness (H) and the average V_p/V_s ratio (κ) from the RF's.

The crustal thickness can be approached as a geometrical problem that concerns the propagation of a non-vertical Ps incident wave inside a medium with a specific thickness H. Zhu and Kanamori (2000) report that the observed time difference between the P and Ps phase can be used in depth (or thickness) calculations, based on the relation:

$$H = \frac{t_{ps}}{\sqrt{\frac{1}{V_s^2} - p^2} - \sqrt{\frac{1}{V_p^2} - p^2}} \quad (3.2)$$

Given that the arrival time of the Ps phase (t_{ps}) and the ray parameter (p) are known and there are assumed average V_p and V_s values, the crustal thickness can be estimated. Furthermore, other phases that follow the Ps can be used for the estimation:

$$H = \frac{t_{PpPs}}{\sqrt{\frac{1}{V_s^2} - p^2} - \sqrt{\frac{1}{V_p^2} - p^2}} \quad (3.3)$$

$$H = \frac{t_{PpSs+PsPs}}{\sqrt{\frac{1}{V_s^2} - p^2} - \sqrt{\frac{1}{V_p^2} - p^2}} \quad (3.4)$$

Zhu and Kanamori (2000) stated that the identification of the arrival time of these phases is a simple procedure, given the fact that a real signal contains noise that prevents a clear and safe picking of the arrival time. Thus, stacking of a great number of RFs could increase the signal/noise ratio (SNR). Stacking is defined as:

$$s(H, k) = w_1 r(t_1) + w_2 r(t_2) - w_3 r(t_3) \quad (3.5)$$

where w_i is the weight and t_i the predicted arrival time of each phase and r is the radial RF. The summation of the weighted factors should be 1 and the $s(H, k)$ reaches the maximum value when all the phases are “stacked coherently” through the gridding process.

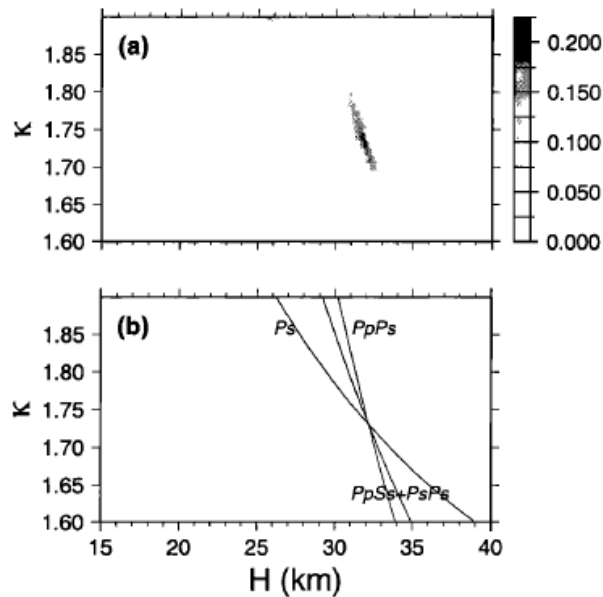


Figure 35: (a) The $s(H, k)$ reaches the maximum when the correct H and κ are used. (b) H - k relation for each phase (Zhu and Kanamori 2000).

3.3 Data selection and main processing

For the present P receiver functions study, seismic data from 49 stations belonging to the HUSN network have been analyzed. The selection of these stations is based on two criteria, the time-period of operation and the spatial distribution. The main aim is to ensure a satisfying distribution of stations in the Greek region with, at the same time, wide time range of recorded data. The selected stations are presented in Figure 36. along with the basic tectonic features of the Greek region.

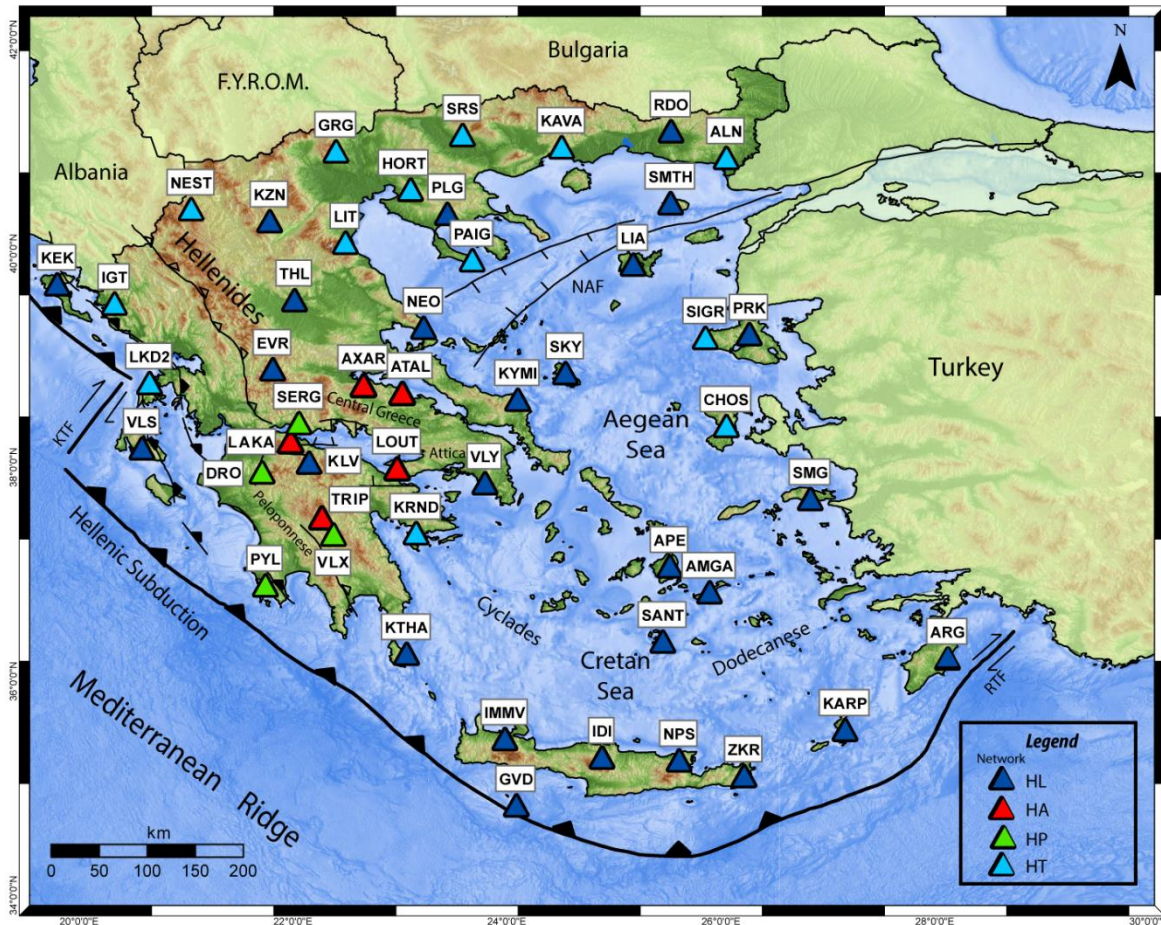


Figure 36: Schematic map of the tectonic settings of the broader Greek region based on Royden and Papanikolaou (2011) and stations of the HUSN network, whose recordings have been analyzed in the framework of the RF study.

Earthquake information for the time period January 2010 until July 2017 was obtained from the United States Seismological Survey (USGS) catalogue (<https://earthquake.usgs.gov/earthquakes/search/>). To ensure that the dataset comprises events suitable for the P-Receiver Functions study, a cut-off moment magnitude (M_w) of 6.0 and an epicentral distance window ranging between 30° and 90° was defined. The selected moment magnitude threshold ensures clear and impulsive arrival of the P-waves in most cases. Also, the specific epicentral distance range ensures that only direct P-wave arrivals are taken into account, having propagated through the Moho boundary. Events with distances larger than 95° from the

recording stations present weak amplitudes of P_{diff} phases (Lombardi et al. 2008). Thus, 362 teleseismic events fulfilled the above-mentioned criteria for the specific time period (Fig. 37).

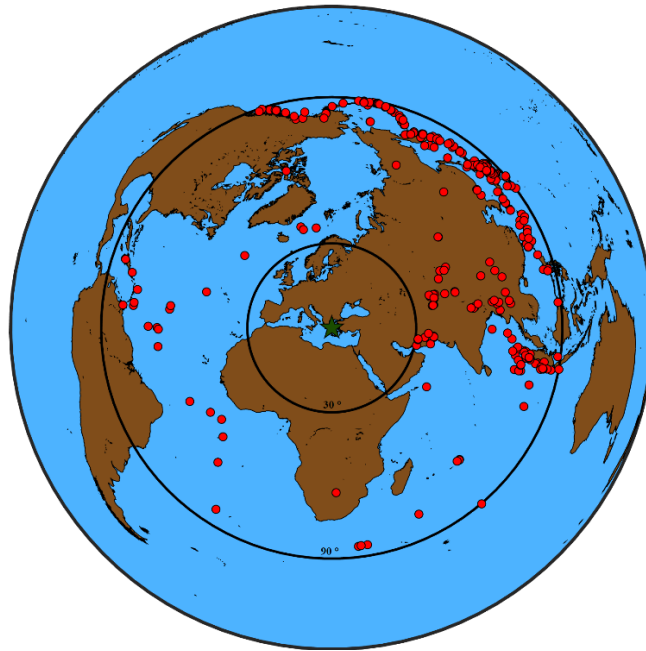


Figure 37: Spatial distribution of teleseismic events that have been used for the P-Receiver Function study. The map is centered on Greece. Minimum and maximum epicentral distances are also shown by black circles.

The waveforms that are used in the analysis were extracted from the continuous data using the events information and the IASP91 model. After the automatic extraction, the waveforms were visually checked for the first time for good signal to noise ratio and problematic data with anomalous signals, missing components or other problems were immediately discarded. Following that, P-wave picking was carried out using the SAC program (<https://ds.iris.edu/ds/nodes/dmc/software/downloads/sac/>) for the waveforms that have been evaluated as “suitable” for analysis after the first inspection. It should be mentioned that the data in this phase of the analysis remain unfiltered and raw (in counts).

Previously in this chapter, it has been mentioned that there is no need for instrument response removal from the selected dataset. The instrument response will be automatically removed together with the source effect afterwards during the application of the deconvolution technique. However, it is necessary to ensure that the gain in all three components is identical. For that purpose, the metadata of all the selected stations were carefully examined. In cases of ambiguities (ARG and THL stations), the instrument response was removed converting the counts to displacement (cm). The specific procedure is common and does not affect the quantity of the RFs. Xu et al. (2007) mention that even a small difference in gain does not affect significantly the RF.

The data preparation continues with the windowing of the desired part of the seismogram. The selected signals were cut 30 seconds before and 200 seconds after the P wave arrival (Fig. 38). There is not a reference time for the cutting window, given that the length of the signal is completely subjective, and can vary depending on the analyst.

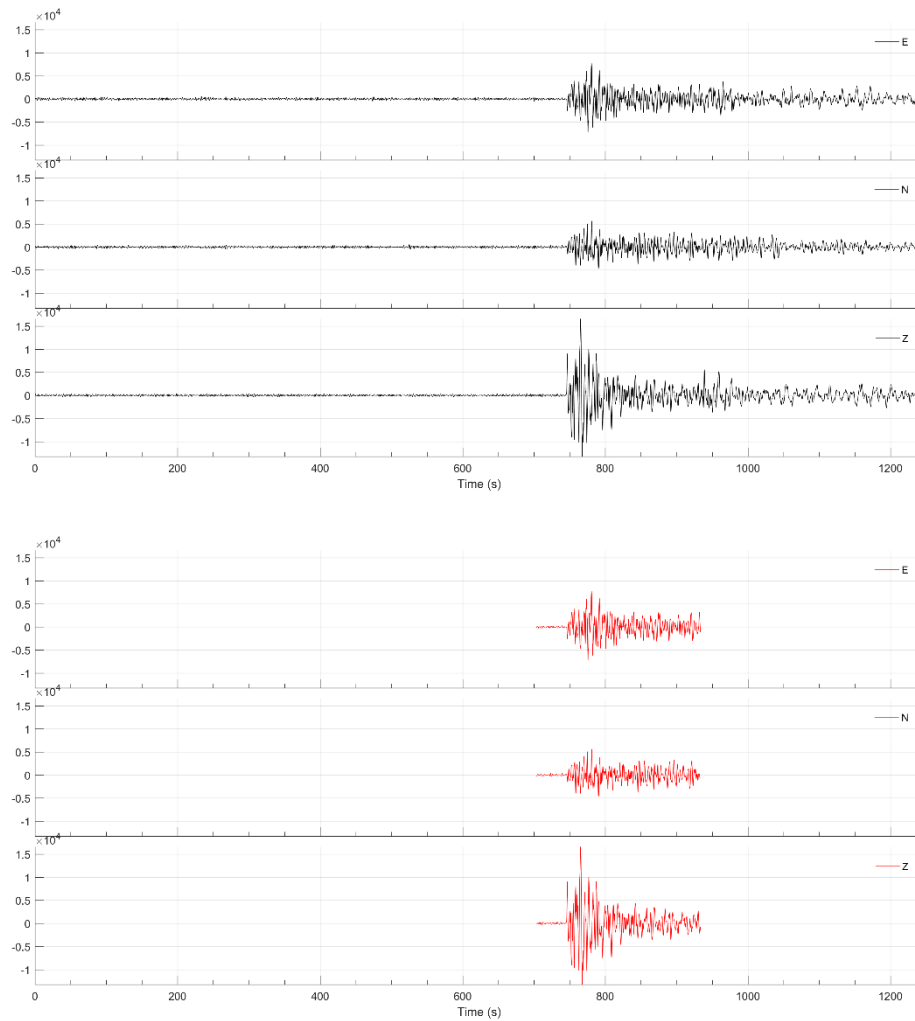


Figure 38: Waveforms from the station CHOS before (black) and after (red) the data windowing. The waveforms are in counts and in the ZNE system.

Proceeding with the data preparation, detrend and filtering was performed for each signal. The bandpass filter that was applied is characterized from low pass equal to 2 Hz and high pass 0.06 Hz. The specific filters allow the dismissal of the unnecessary noise, ensuring that the valuable information remains intact. After bandpass filtering, the signals are ready to be rotated in the ZRT system, as previously described (Fig. 39).

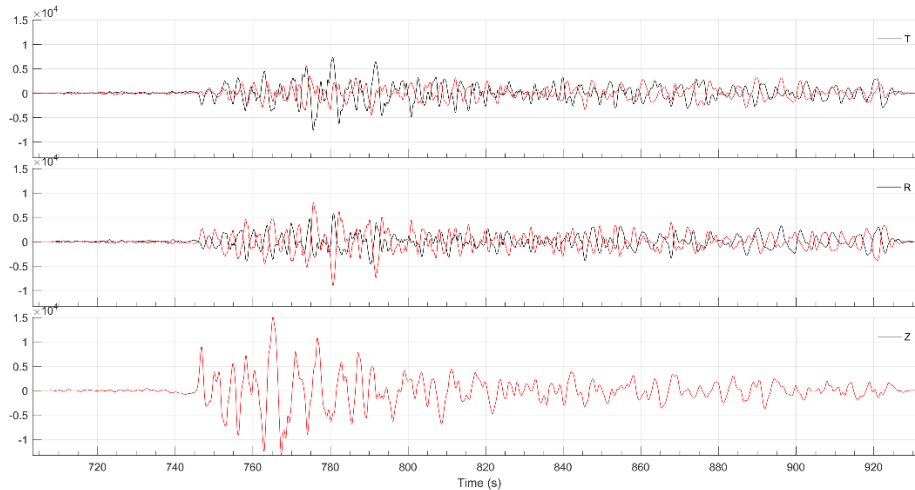


Figure 39: Waveforms from the station CHOS before (black) and after (red) the rotation from the ZNE to RTZ system.

The main objective of all previous steps was to prepare the waveforms for the deconvolution procedure that is the “key” procedure of the RF methodology. Following the rotation, the recordings were deconvoluted in the frequency (Waterlevel) and in the time (Iterative) domain. Results obtained by these two methods will be compared. In both cases (frequency and time domain), a Gaussian filter was applied in order to reduce the noise effects. The Gaussian width factor (G) was set in 1.5 rad/s after a trial-error testing. Values of G larger than 2.5 had as a result noisy RFs and values smaller than 1.0 rad/s provided smooth RFs, rendering the identification of heterogeneities impossible. In addition, an 1.5 rad/s width factor (G) is recommended by previous studies as ideal case (e.g. Ligorria and Ammon 1999). Regarding the Waterlevel deconvolution, a typical threshold was used ($\sigma=0.01$) and for the Iterative deconvolution the procedure was ended after 200 iterations for each event. Figure 40 presents RFs from CHOS station, revealing fluctuations that can be attributed to specific wave phases based on the wave theory.

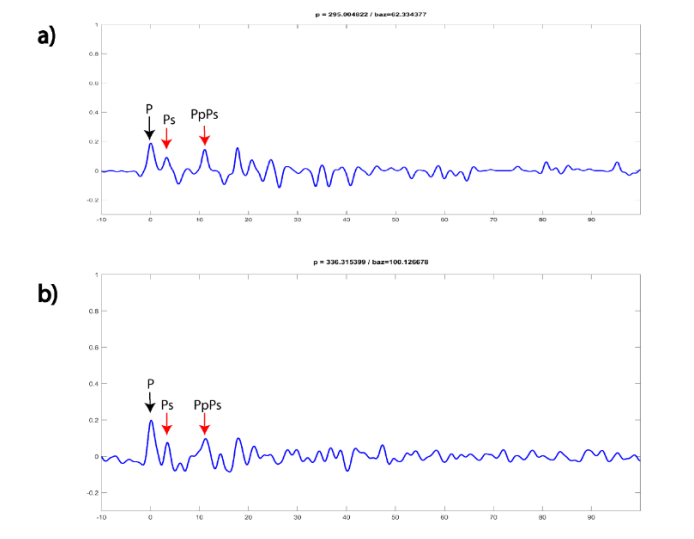


Figure 40: RF traces from the Iterative (a) and from Waterlevel (b) deconvolution. The red arrow indicates the arrival time of the P wave and the black arrows the Ps phase and its first multiple.

The red and the black arrows in Figure 40 indicate the arrival time of the P, Ps and PpPs phases. The identification of the phase arrivals is based on the velocity changes, which are imprinted in the amplitude changes of the RF. Positive amplitudes indicate velocity increase with depth, whereas negative amplitudes are related to velocity decrease with depth. Generated phases from boundaries with sharp velocity changes (e.g. Moho) are determined in the RF by their large amplitude (positive or negative). The length of the resulted RF is 110 seconds (10 sec before the P arrival and 100 sec after). The deconvolution process is completed when all RFs from each station are visually inspected from the analyst. Noisy traces with anomalous amplitudes were discarded, due to the fact that they imply unstable deconvolution.

The identification of the Ps phase and of its multiples is not always an easy task as in the previous example. There is a large number of RFs that present noisy effects, fact that undermines the clarity of the resulted RF. In order to overcome this problem, a linear or “simple” stacking technique will be applied in the traces of each station. The stacking technique involves summation of a specific group of records into one single trace. In this way, weak signals or phases can be upsized and identified more easily. It has been proven that the stacking technique can be helpful to acquire valuable information regarding the Earth’s interior, even without deconvolution (Kumar et al. 2010). Linear stacking is a common method in RF studies (e.g. Dugda et al. 2005; Pan and Niu 2011). Another issue that has to be mentioned is the moveout correction. The different incidence angle (or epicentral distance and focal depth) of each wave has as a result different arrival times of the converted phases (moveout phenomenon). The differential arrival times could be a destructive factor, especially during the interpretation of the stacked trace. However, the moveout for the Moho conversions (Ps) is insignificant and the signals could be stacked without any further concern if they are lined up in the P wave arrival time (Kind et al. 2012). Therefore the moveout correction could be skipped, given that the present study’s aim is to identify Moho signals (e.g. Ps). All records (Radial RF) of each station are stacked into a single trace (Fig. 41).

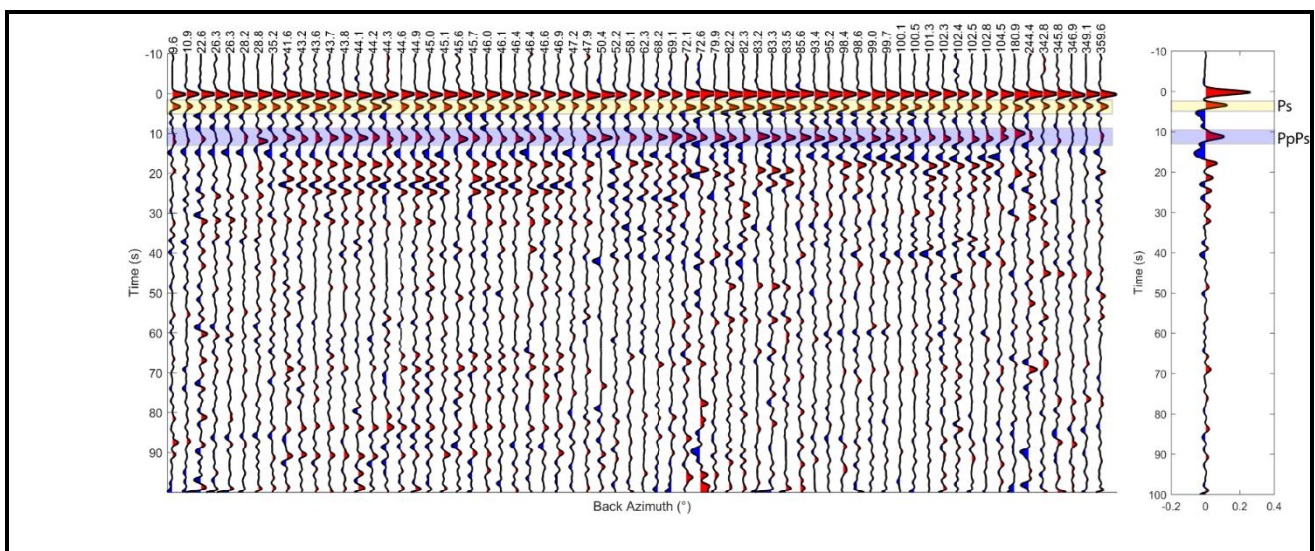


Figure 41: Radial RF (Iterative deconvolution) for the CHOS station, regularly spaced (left side). In the right panel the linear stacked trace is presented. Yellow and blue highlight colors indicate the Ps and the PpPs phase, respectively.

The reliable determination of the Moho converted phases arrival times is a vital step for the RF study. However, the ultimate goal is the depth determination, where the conversions occur. The H- κ stacking method (see 2.3) will be used. The grid search involves a range of crustal thicknesses (H) between 20 and 65 km, while the κ values range between 1.5 and 2.0. In addition, the methodology requires a stable V_p value. The average crustal velocity that was chosen for the procedure is $V_p=6.3$ for the Greek area, based on traveltimes (Papazachos and Nolet 1997; Mutlu and Karabulut 2011). The required weights for the H- κ procedure was set initially 0.6, 0.3 and 0.1 for the Ps, PpPs and PpSs+PsPs, respectively. These values are slightly changed in cases were some phases demonstrate weak amplitudes. In general, the weighting pattern is $w_1(\text{Ps}) > w_2(\text{PpPs}) > w_3(\text{PpSs+PsPs})$. The above mentioned grid search boundaries remained identical for the whole procedure to avoid the introduction of subjective interpretation of the results (Agostinetti and Amato 2009). Moreover, the Poisson ratio is calculated using the H- κ results (Christensen 1996):

$$\sigma = \frac{\kappa^2 - 2}{2(\kappa^2 - 1)} \quad (3.6)$$

Figure 42 presents a H- κ stacking plot that shows the energy variance for each phase in the crustal thickness - V_p/V_s ratio domain. The uncertainties for the optimal H- κ pair are shown in black ellipses, following the approach of Eaton et al. (2006).

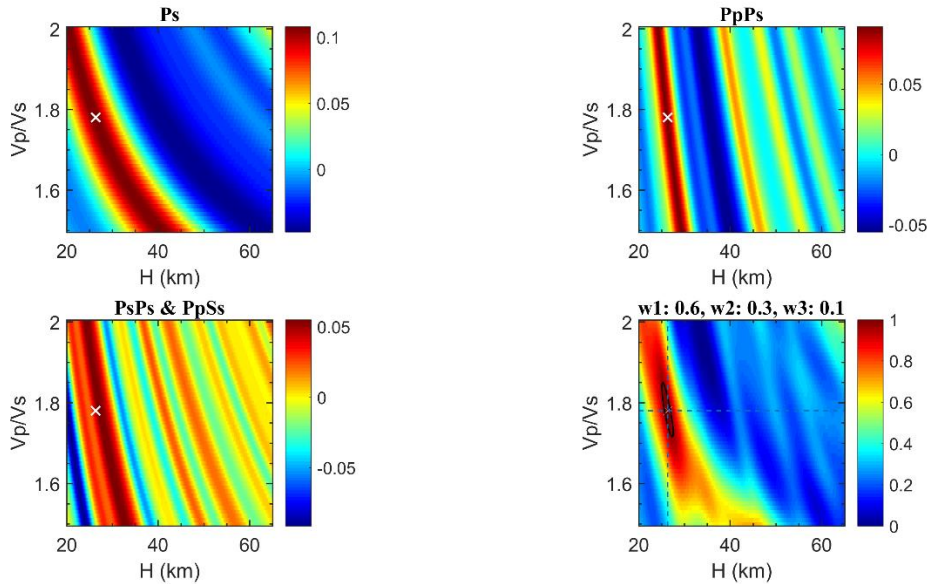


Figure 42: H- κ stacking example plots for each phase for the CHOS station. The lower-right plot constitutes the total plot, with the optimal (maximum) pair in the center of the ellipse. In each case the maximum value is indicated by the white “x” symbol.

3.4 Results

3.4.1 Stations quality

The analysis had as a result 2447 RF for 49 stations using the Iterative deconvolution method and 2330 RF from the Waterlevel deconvolution for 47 stations in the Greek region. The spatial distribution of the results is considered satisfactory, taking into account the available stations of the HUSN network. At this point, it is necessary to mention that the largest part of the analyzed stations provided high quality results/data. However, a more detailed quality assessment of the observations is required for scientific and practical purposes. For this reason, each station was categorized into one of three quality groups (A, B, C), based on the quality of the observable Moho phases. In more detail, the quality group A includes stations that present clear arrival signal of the Ps and the PpPs phases in their stacked signal. Correspondingly, the B quality group includes stations with clear Ps and poor PpPs arrival and the C quality group Ps and PpPs weak arrivals. In general, there is no clear correlation between the quality group of a station and its geographical location (Fig. 43, 44). It is more likely that the quality distribution is connected only with practical reasons which concern the functional conditions of the stations. However, it is worth noting that the Waterlevel method offer a slightly higher number of B quality stations compared to the Iterative.

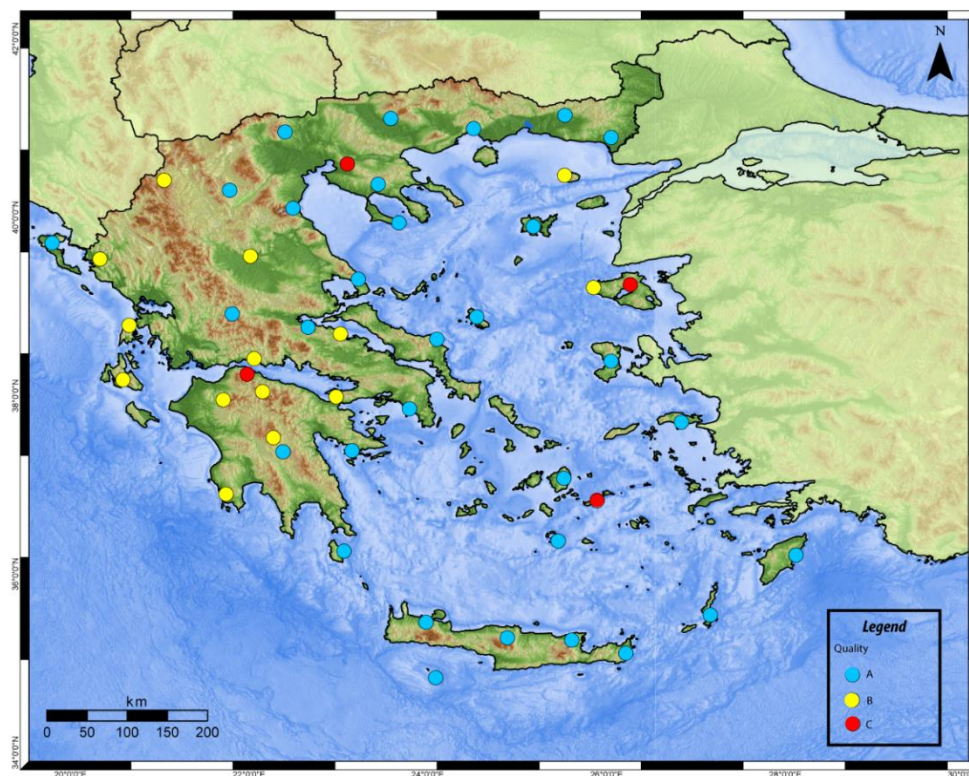


Figure 43: Stations quality groups - Iterative deconvolution.

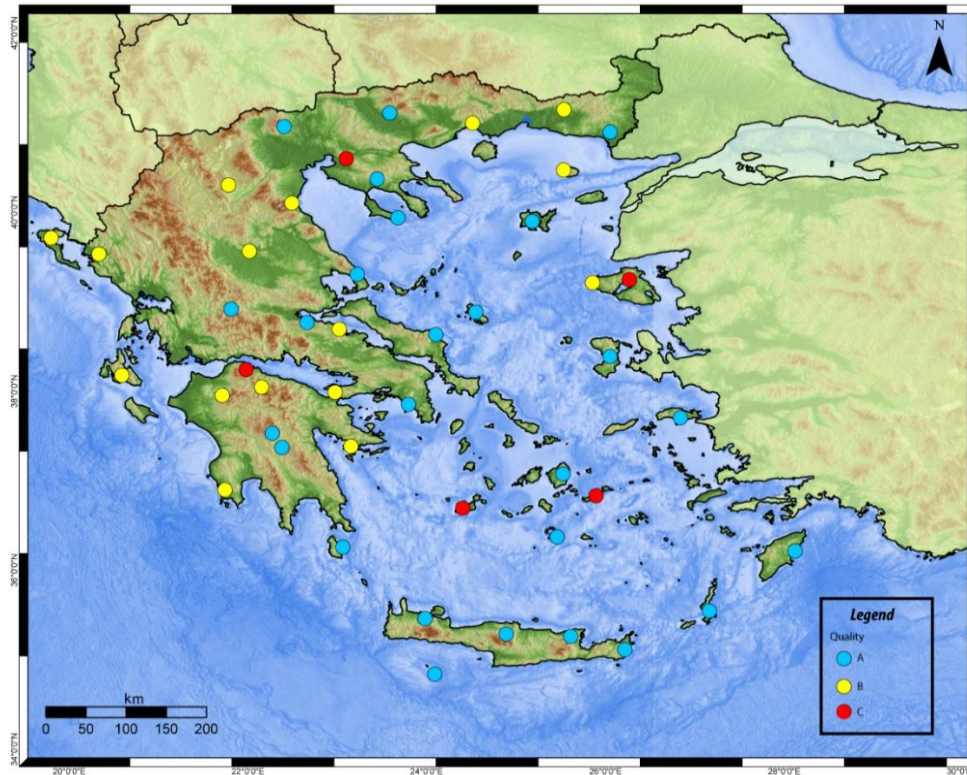


Figure 44: Stations quality groups -Waterlevel deconvolution.

3.4.2 Ps arrival times

3.4.2.1 Aegean Sea

The southern part of the Aegean Sea includes three analyzed stations, namely APE, SANT and AMGA. The APE station presents Ps arrivals ~ 3.1 sec after the P phase (0 sec) for the Waterlevel and ~ 2.8 sec regarding the Iterative deconvolution (Fig. 45). The arrival times for the PpPs are clear in both deconvolution methods, approximately 10.5 sec. The backazimuthal distribution of the successful analyzed events belongs mainly in the 0° - 110° degree window. The SANT station presents a more complicated signal compared to the APE station. The Ps arrivals are identified approximately at 3.9 sec (Waterlevel) and at 3.8 sec (Iterative) after the P wave arrival. The PpPs is also clear, 10.8 sec for the Waterlevel and quite later (13.9 sec) for the Iterative. The important fact for the SANT station is that there is also a clear Ps arrival from the subducted slab that arrives after (~ 11 sec) the Moho Ps phase. The complication of the SANT signal is due to the continuous succession of arrival phases during the first 20 sec. In contrast, the signals from the AMGA station are much simpler compared to the other cases. The Ps arrival times are ~ 2.3 sec for the Iterative and ~ 2.9 sec for the Waterlevel method. The latter mentioned times for the AMGA station are also the lowest arrival times in the whole Greek region. This is related to the Moho depth as it will be described in the Discussion section. However, it is worth noting that the number of the resulted RF is lower compared to other stations of the broader area.

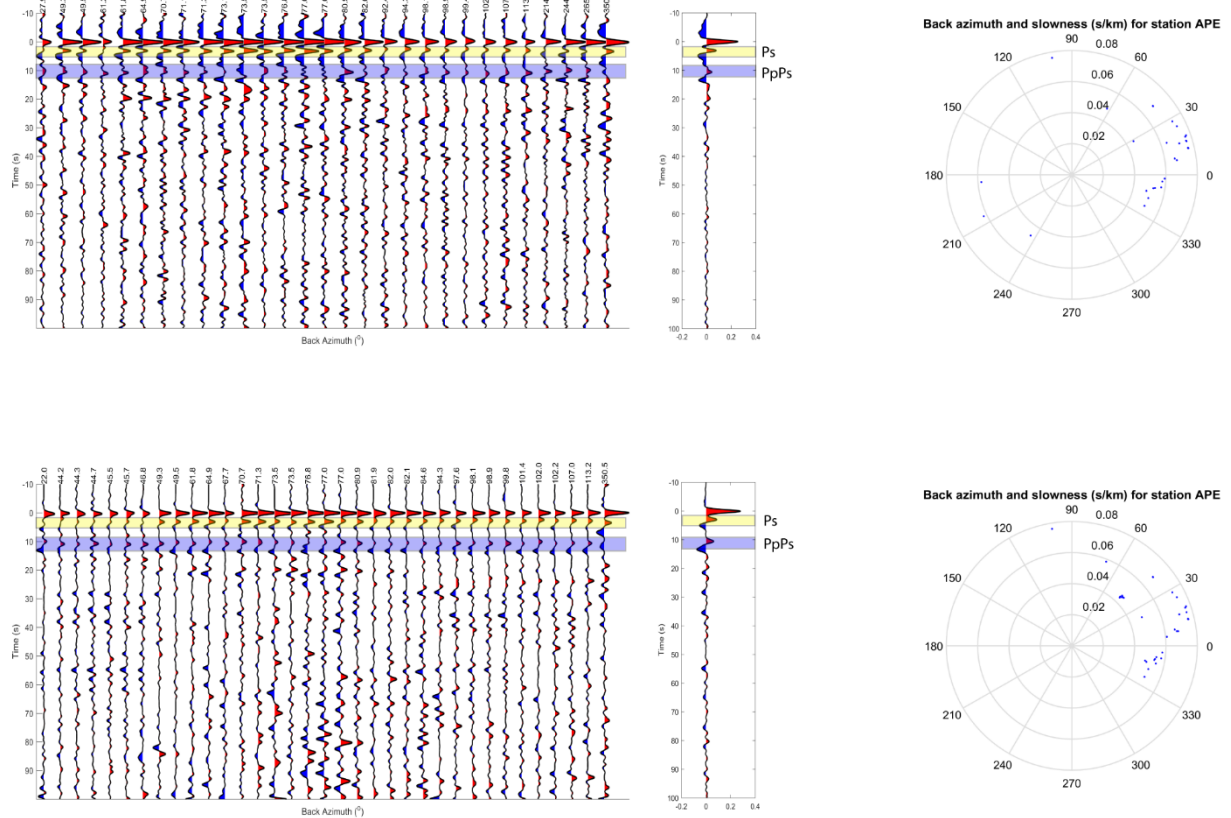


Figure 45: Radial RF for the APE station, regularly spaced (left side). In the upper panel the results from the Iterative deconvolution and in the lower from the Waterlevel together with the linear stacked trace. Yellow and blue highlight colors indicate the Ps and the PpPs phase, respectively. To the right the backazimuthal distribution of the RF for each method is presented.

In the central-eastern part of the Aegean Sea the stations SMG and CHOS provided RF results. In the case of the SMG station the Ps and the PpPs arrival times are close for both deconvolution methods (~ 3.3 sec and ~ 11 sec, respectively). However, the number of the resulted RF using the Iterative method is higher compared to the Waterlevel. A similar picture is also observable in the CHOS station, with the Ps and PpPs arrival times being ~ 3.4 sec and ~ 11.4 sec for the Iterative and ~ 3.2 sec and ~ 11 sec for the Waterlevel method. Both stations reveal in general a similar behavior in the arrival times of the Moho converted phases.

The analyzed stations in the north Aegean are SKY, SIGR, PRK, LIA and SMTH. All these stations, with the exception of the PRK, present high-quality RF results. Ps and PpPs signals in SKY station are close to 2.6 sec and to 10.4 sec for both deconvolution methods. The same similarity in arrival times for both methods is also identified in the LIA station, with 3.2 sec and 11.3 sec approximate arrival times for the Ps wave and its first multiple, respectively (Fig. 46). A slight difference between the two methods is presented in the Ps phase of the SMTH station that arrives ~ 3.3 sec for the Waterlevel and ~ 3.6 sec for the Iterative method. The PpPs phase arriving almost simultaneously ~ 9.8 sec for both methods. This difference (~ 0.3 sec) is very small and is probable connected to the different methodologies, given the fact that the backazimuthal distribution of the successful RF results is the same for the two methods. Last but not least, the station SIGR reveals Ps arrival times close to 3.3 sec and PpPs close to 10.3 sec, with hardly any differences between the two deconvolution methods concerning the observed times. Station SIGR was implemented to the analysis due to low quality RF results from the PRK station (quality C).

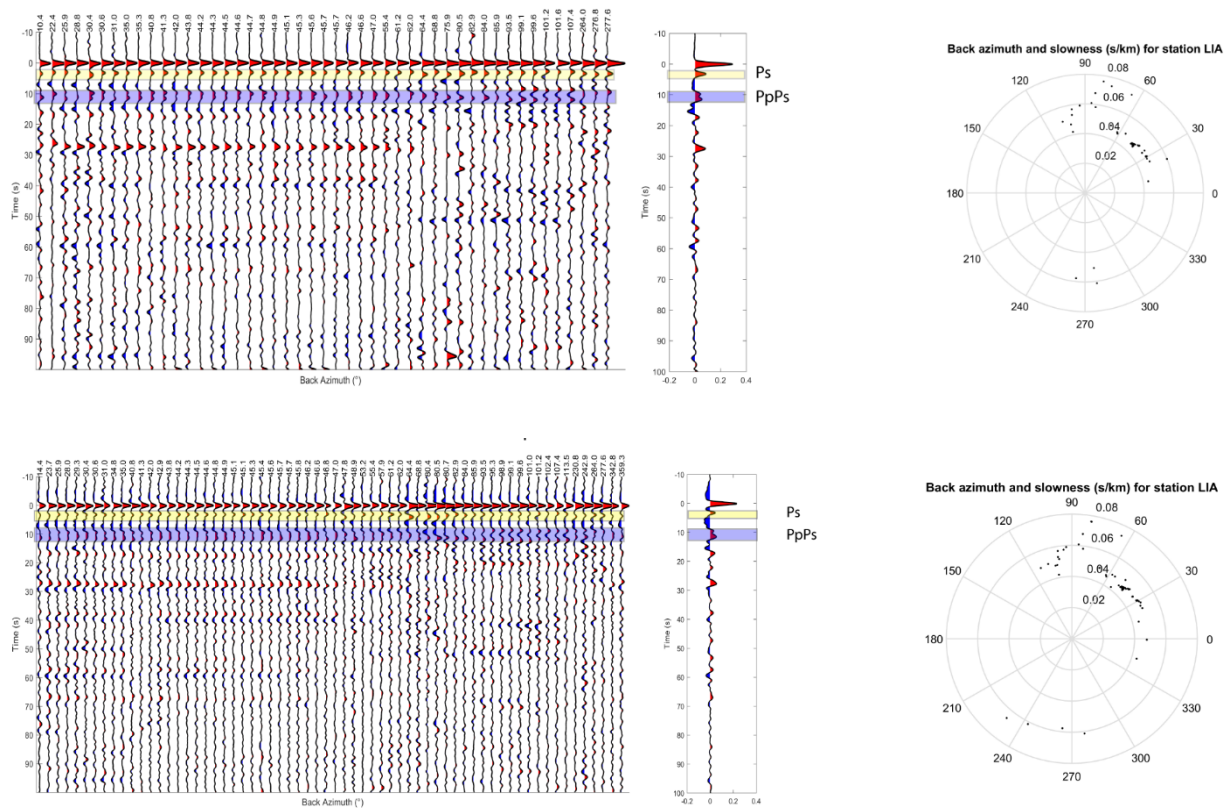


Figure 46: Radial RF for the LIA station, regularly spaced (left side). In the upper panel the results from the Iterative deconvolution and in the lower from the Waterlevel together with the linear stacked trace. Yellow and blue highlight colors indicate the Ps and the PpPs phase, respectively. To the right the backazimuthal distribution of the RF for each method is presented.

3.4.2.2 Subduction zone

Intentionally, the present P-RF study incorporates stations from over the entire Greek region. Special attention was given in the vicinity of the subduction zone and, as a result, 11 stations lying were analyzed. From the east to the west these stations are: ARG, KARP, ZKR, NPS, IDI, GVD, IMMV, KTHA, VLS, LKD2 and KEK.

The station ARG lies in the easternmost part of the Hellenic subduction zone. The stacked RF present, in both of the deconvolution cases, a positive pulse close to 7-8 sec and a negative one ~3.5 sec. This behavior (i.e. strong positive pulse after the 5 sec of the trace) appears also in the stations located in Crete (IDI, IMMV, NPS and ZKR), as well as in KTHA and KARP. In all the above-mentioned cases the stacked traces are dominated by a persistent negative pulse in the first seconds and a strong positive after the 5 sec. Considering that the RF in this region (near the subduction) should be dominated by a succession of positive pulses generated by the Aegean and the African Moho, these observations require further investigation. This phenomenon will be examined consistently in the next paragraphs of this chapter. Results of the IDI station are presented in Figure 47.

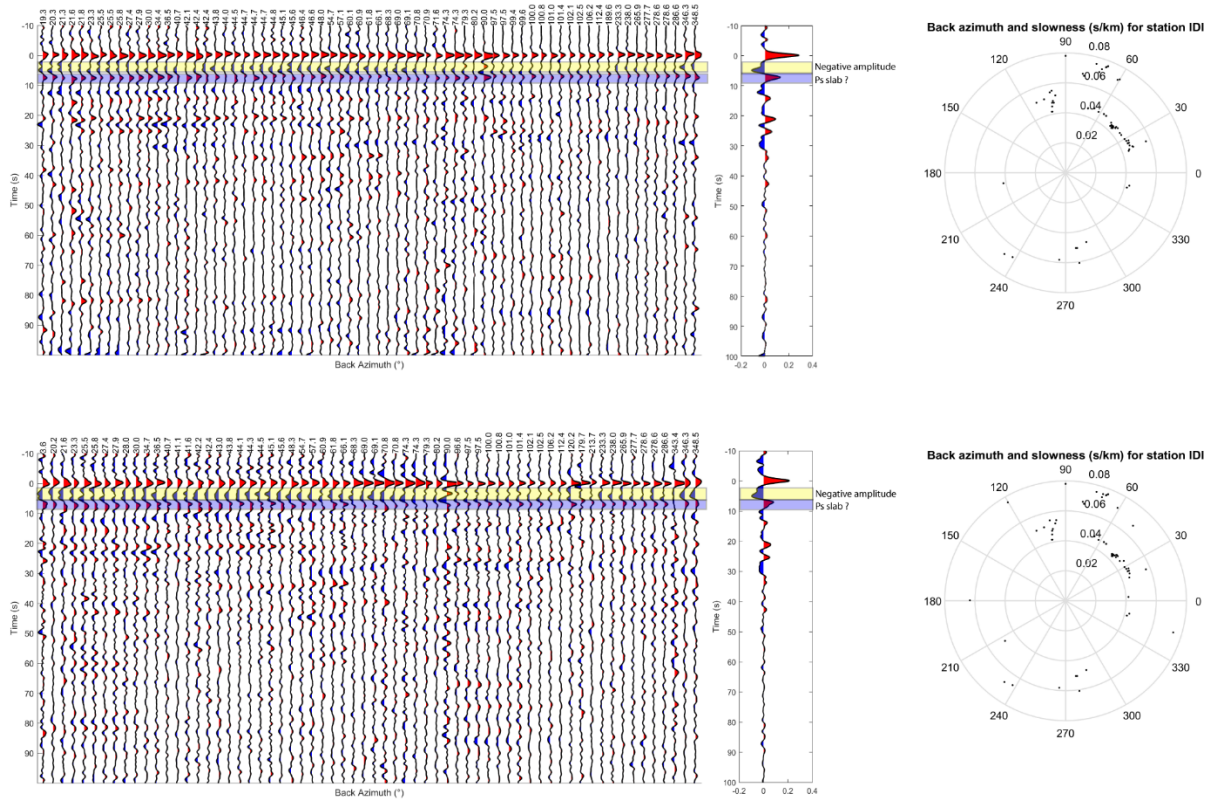


Figure 47: Radial RF for the IDI station, regularly spaced (left side). In the upper panel the results from the Iterative deconvolution and in the lower from the Waterlevel together with the linear stacked trace. Yellow and blue highlight colors indicate the Ps (?) and the PpPs phase, respectively. To the right the backazimuthal distribution of the RF for each method is presented.

In the eastern part of the subduction zone this phenomenon is fading out, with the stations VLS and LKD2 presenting three distinct positive pulses during the first 10 sec. In more detail, the station VLS reveals a first strong positive amplitude at ~ 3.7 sec for the Waterlevel and ~ 4.7 sec for the Iterative technique. The second positive pulse emerges at ~ 12.1 sec and ~ 11.8 sec for the above-mentioned methods, respectively. In addition, a third but much smaller pulse exists just before the second arrival, approximately at 8.7 sec (Fig. 48). For the station LKD2 the situation is more complicated, due to the fact that only the Iterative deconvolution resulted reliable RF. Similarly, the signal in the LKD2 station presents positive (weak) amplitudes at ~ 4.68 sec, ~ 8.7 sec and ~ 13.28 sec. The attribution of each arrival to a specific structure should be careful and will be discussed in detail later.

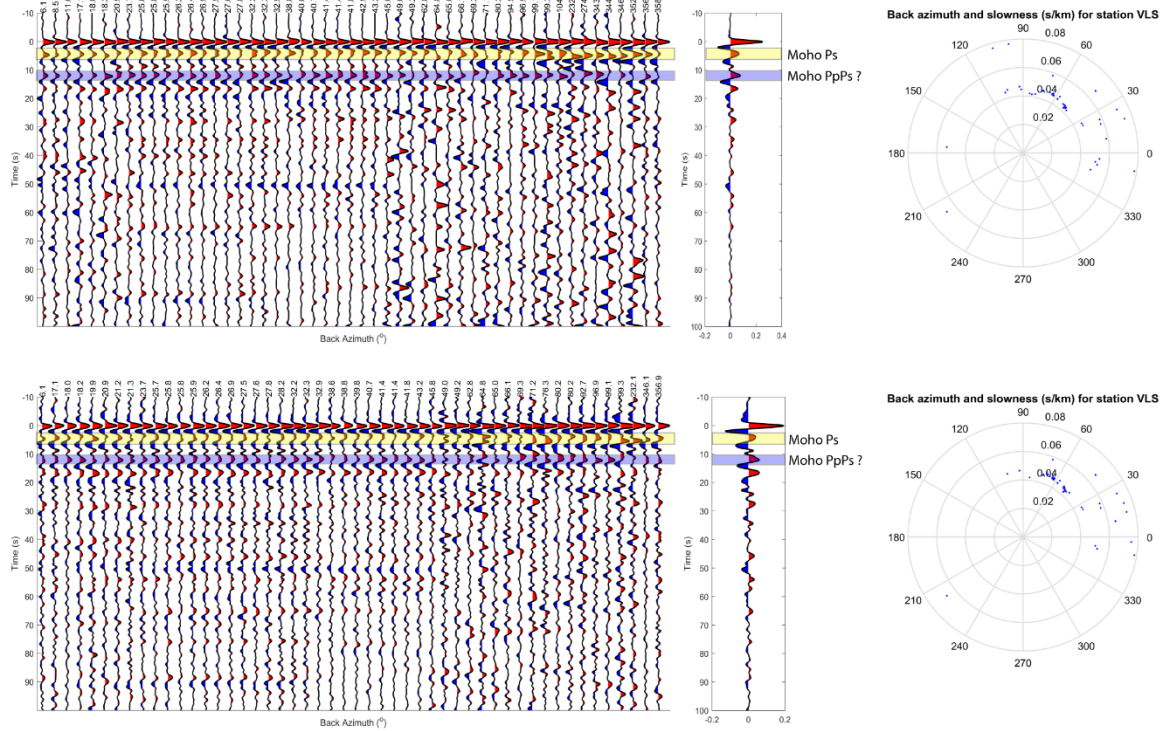


Figure 48: Radial RF for the VLS station, regularly spaced (left side). In the upper panel the results from the Iterative deconvolution and in the lower from the Waterlevel together with the linear stacked trace. Yellow and blue highlight colors indicate the Ps and the PpPs (?) phase, respectively. To the right the backazimuthal distribution of the RF for each method is presented.

3.4.2.3 Mainland Greece

The north part of the mainland Greece is characterized by a simple behavior of the RF, that will be described briefly in this paragraph. The station ALN, near the borders with Turkey, presents Ps arrival times approximately at 4.3 sec (in both methods). The arrival times in RDO and KAVA show a decrease of the Ps arrival times, being ~3.7 sec and ~3.5 sec, respectively. Arrival times larger than 4 sec are identified in SRS (Fig. 49), HORT and KZN stations, with NEST exceeding 5 sec in the Iterative deconvolution. In contrast, stations near the Aegean Sea (PAIG, PLG and LIT) present arrival times of the order of 3.0 - 3.8 sec. In general, this part of Greece is characterized by simple RF signals, exhibiting significant variations in the arrival time of the first Moho multiple. A possible connection of this phenomenon with the geodynamic features will be examined later.

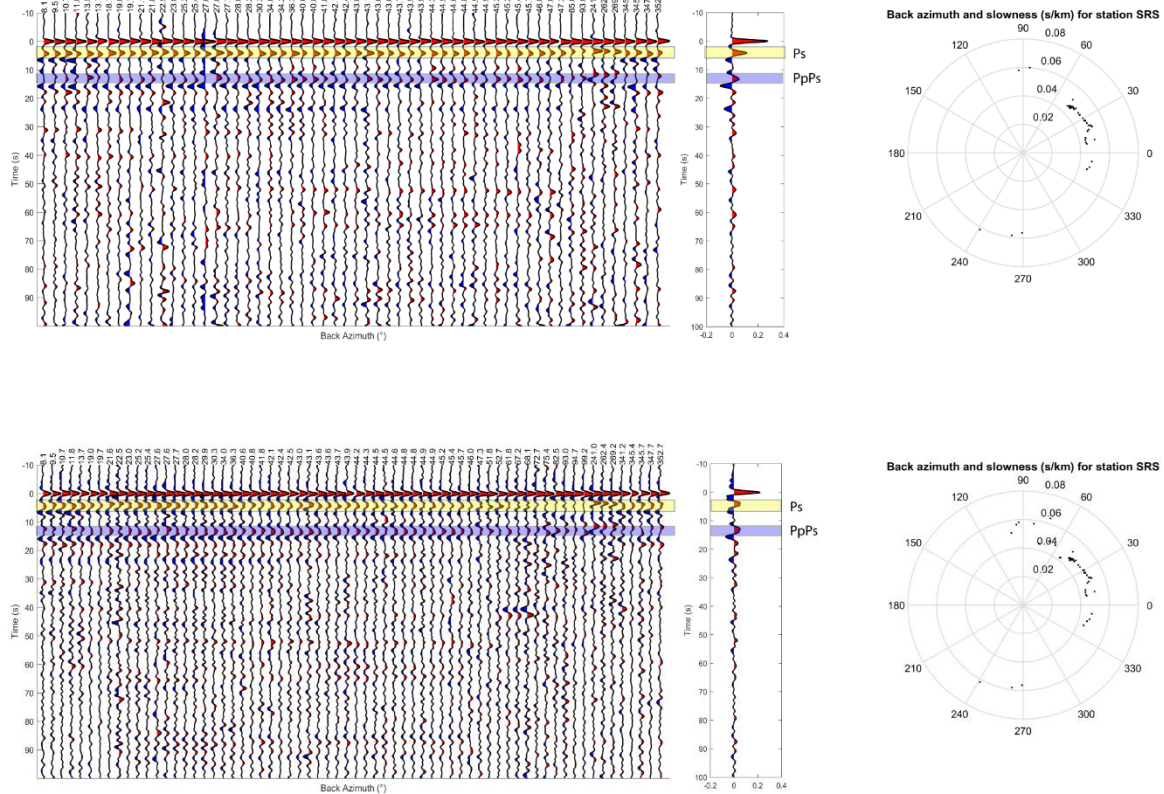


Figure 49: Radial RF for the SRS station, regularly spaced (left side). In the upper panel the results from the Iterative deconvolution and in the lower from the Waterlevel together with the linear stacked trace. Yellow and blue highlight colors indicate the Ps and the PpPs phase, respectively. To the right the backazimuthal distribution of the RF for each method is presented.

Notably, large Ps arrival times are also obtained in a major part of Central Greece. The stations THL, SERG and ATAL exceed by far the 4 sec and the station EVR reaches the 8 sec arrival times in both methods. The rest of the stations (AXAR, VLY, KYMI) present lower arrival times, in the range 3-3.5 sec. The spatial distribution of the stations that provided RF results in this part of Greece is not so satisfactory due to low data quality. However, the acquired observations are more than enough in order to approach the general Moho trends in this area. Stations in Peloponnese are also characterized by large Ps arrival time in both deconvolution methods. Stations such as TRIP, VLX and DRO need more than 7 sec in order to present the strongest positive pulse (Ps) in their stacked traces. The “large arrivals time trend” decreases moving away from the central part of Peloponnese, with the KRND and LOUT stations presenting arrival times slightly over 4 sec.

Observations in mainland Greece present the largest arrival times, compared to the Aegean Sea and the subduction zone. The specific phenomenon will be examined in detail later, but it is useful for now to identify a “large time” arrival trend that begins from the northern mainland Greece and ends up in the center of Peloponnese.

3.4.2.4 Moho depths from Ps times and H-k stacking

The estimated arrival times of the Ps and PpPs phases were picked manually from the linear stacked RF for each deconvolution method. The difference between these two methods in the arrival times are barely noticeable in most of the cases. As it is mentioned previously, the Ps arrival times can be converted to depths based on the relation (3.2). The specific approximation can certainly import significant errors. However, it is still a satisfactory approach, especially regarding the stations where the H-k method could potentially fail. For the conversion, stable (crustal average) velocity values of $V_p=6.3$ km/sec and $V_s=3.7$ km/sec (Papazachos and Nolet 1997; Mutlu and Karabulut 2011) for the Greek region were adopted. The depth approximation results are presented in Tables 3, 4 for the Waterlevel and the Iterative deconvolution, respectively.

Except from the Ps arrival times from the Moho boundary, in some cases arrival Ps times from the Hellenic slab (or African Moho) were also identified. The same conversion procedure with the Aegean Moho was applied in order to identify the slab depth beneath the stations. The results of this conversion are presented in Table 5. Signals that contain slab phases and multiples concern mainly stations close to the subduction zone, presenting depths 46-60 km. The slab depth increases moving away from the subduction, having as a result values that reach the 95 km in the station SANT.

Table 3: Arrival times of the Ps and PpPs phases for every analyzed station using the Waterlevel deconvolution method. Based on the Ps arrival times, the Moho depth has been calculated. In addition, the number of the resulted RF for every station is presented.

Station	Net	No. RF	TPs (s)	TPpPs (s)	H Moho (km)
ATAL	HA	22	4.32	9.61	37.06
AXAR	HA	39	3.34	13.60	28.75
LAKA	HA	46	3.04	8.35	26.45
LOUT	HA	14	4.01	12.15	34.03
TRIP	HA	66	7.39	17.05	64.29
AMGA	HL	17	2.89	9.72	25.03
APE	HL	29	3.08	10.67	26.79
ARG	HL	51	3.60	-	31.35
EVR	HL	50	8.04	14.58	69.94
GVD	HL	59	3.16	11.16	27.49
IDI	HL	64	4.60	-	39.77
IMMV	HL	106	3.25	-	28.18
KARP	HL	31	3.55	12.33	30.95
KEK	HL	26	3.20	12.62	27.66
KLV	HL	42	4.19	8.48	36.38
KTHA	HL	26	3.40	-	29.58
KYMI	HL	40	3.48	10.35	30.05
KZN	HL	67	4.59	14.66	39.93
LIA	HL	64	3.18	11.28	27.66
MHLO	HL	15	1.49	8.01	12.97

NEO	HL	66	3.19	11.44	27.70
NPS	HL	33	4.48	-	38.65
PLG	HL	75	3.73	9.00	32.39
PRK	HL	97	3.93	9.84	34.08
RDO	HL	95	3.70	9.43	32.19
SANT	HL	37	3.94	13.95	33.60
SKY	HL	40	2.63	10.44	22.86
SMG	HL	56	3.30	11.10	28.71
SMTH	HL	71	3.32	9.76	28.86
THL	HL	57	3.86	12.74	33.18
VLS	HL	50	3.72	12.13	32.36
VLY	HL	38	2.91	11.40	25.31
ZKR	HL	39	3.76	-	32.19
DRO	HP	49	7.00	19.12 (?)	60.97
PYL	HP	38	5.01	14.42	43.58
VLX	HP	30	7.34	16.18	64.04
ALN	HT	82	4.27	13.63	37.15
CHOS	HT	69	3.18	11.05	27.59
GRG	HT	56	3.78	14.09	32.81
HORT	HT	39	4.90	12.62	42.66
IGT	HT	18	4.54	13.32	38.82
KAVA	HT	79	3.57	10.42	30.96
KRND	HT	32	4.66	10.19	40.22
LIT	HT	34	3.46	10.38	30.10
PAIG	HT	66	3.21	10.44	27.79
SIGR	HT	44	3.31	10.42	28.80
SRS	HT	66	3.91	13.10	34.08

Table 4: Arrival times of the Ps and PpPs phases for every analyzed station using the Iterative deconvolution method. Based on the Ps arrival times the Moho depth has been calculated. In addition, the number of the resulted RF for every station is presented.

Station	Net	No. RF	TPs (s)	TPpPs (s)	H Moho (km)
ATAL	HA	31	4.63	9.69	40.03
AXAR	HA	36	3.39	13.26	29.30
LAKA	HA	46	2.98	8.10	25.92
LOUT	HA	16	4.13	11.95	35.58
TRIP	HA	50	7.13	16.96	62.02
AMGA	HL	19	2.29	8.07	19.89
APE	HL	35	2.76	10.52	24.01
ARG	HL	47	3.41	-	29.73
EVR	HL	66	8.10	14.62	70.46
GVD	HL	39	3.02	11.25	26.27
IDI	HL	69	4.66	-	40.38
IMMV	HL	77	3.24	-	28.18
KARP	HL	38	3.66	12.37	31.89
KEK	HL	28	3.35	12.35	29.02
KLV	HL	41	4.13	8.23	36.00

KTHA	HL	26	3.40	-	29.58
KYMI	HL	42	3.38	10.04	29.24
KZN	HL	67	4.36	13.07	37.93
LIA	HL	47	3.22	11.43	27.96
NEO	HL	67	3.31	11.11	28.79
NPS	HL	40	4.85	-	42.04
PLG	HL	75	3.80	9.00	33.06
PRK	HL	107	3.67	9.96	31.87
RDO	HL	64	3.73	9.31	32.45
SANT	HL	49	3.79	10.86	32.59
SKY	HL	39	2.56	10.36	22.27
SMG	HL	76	3.29	10.93	28.62
SMTH	HL	82	3.60	9.88	31.32
THL	HL	57	4.05	-	35.07
VLS	HL	51	4.57	11.79	39.75
VLY	HL	51	3.04	11.71	26.45
ZKR	HL	52	3.67	-	31.58
DRO	HP	63	7.00	19.47	61.27
PYL	HP	35	5.12	13.97	44.50
SERG	HP	30	4.60	14.72	40.02
VLX	HP	40	7.16	15.96	62.40
ALN	HT	58	4.30	12.27	37.40
CHOS	HT	66	3.46	11.40	30.04
GRG	HT	60	3.59	14.11	30.00
HORT	HT	58	4.67	12.19	40.71
IGT	HT	22	4.65	13.65	39.93
KAVA	HT	83	3.51	9.62	30.45
KRND	HT	32	4.89	10.23	42.44
LIT	HT	45	3.36	10.34	29.23
LKD2	HT	30	4.68	13.28	40.71
NEST	HT	25	5.29	17.21	46.02
PAIG	HT	68	3.09	10.57	26.00
SIGR	HT	44	3.38	10.22	29.44
SRS	HT	58	4.15	13.30	36.19

Table 5: Arrival times of the Ps phases, possibly attributed to the slab (African Moho) for the Iterative and the Waterlevel deconvolution. Based on the Ps arrival times the Moho depths has been calculated.

Station	Net	Waterlevel		Iterative	
		Slab (s) TPs	H slab (km)	Slab (s) TPs	H slab (km)
AMGA	HL	-	-	9.91	86.29
ARG	HL	5.33	46.41	5.02	43.77
GVD	HL	5.75	50.02	5.81	50.54
IDI	HL	7.08	61.21	7.20	62.38
IMMV	HL	6.47	56.10	6.63	57.66

KARP	HL	6.47	56.40	6.68	58.20
KTHA	HL	6.95	60.46	6.95	60.46
NPS	HL	7.68	66.26	7.68	66.57
SANT	HL	11.07	94.41	11.00	94.59
VLS	HL	8.70	75.54	8.68	75.51
ZKR	HL	6.72	57.54	6.66	57.31

The depth of the Moho boundary was also defined using the popular H-k stacking method. The procedure and the basic theory of the method was analyzed in detail in paragraph 2.2. The H-k stacking method was implemented successfully in similar P-receiver functions studies, in complicated geodynamical systems around the world, from subduction zones (e.g. Agostinetti and Amato 2009) to stable blocks (e.g. Li et al. 2014). Certainly, the application of this procedure in complicated systems, such as the Hellenic subduction zone, can be proved unreliable due to puzzling form of the RF. However, the effectiveness of this method in the Greek area is noteworthy and the analytical results are presented in the Tables 6, 7 along with the errors for each case.

In total, 31 from the initial 47 stations provided results for the H-k stacking method. The methodology of Zhu and Kanamori (2000) failed in cases where the signal was too complicated or presented weak phase amplitudes. In more detail, stations near the subduction zones did not offer credible results due to the presence of alternate phases that belong to the slab, which were interposed between the Moho phases. Also, in cases where the Moho phases were weak, the methodology was unable to successfully determine the optimal H-k pair due to unreasonably high errors. From the determined V_p/V_s , the Poisson ratio was also calculated using the relation (3.6) proposed by Christensen (1996).

Table 6: Depth and V_p/V_s approximations for each station from the H-k stacking (Iterative deconvolution). In addition, the errors of each quantity and the final quality of each station are presented.

Station	Net	V_p/V_s	V_p/V_s Error	Poisson Ratio (σ)	H (km) Moho	H Error
AXAR	HA	1.60	0.06	0.18	35.00	1.37
LOUT	HA	1.96	0.10	0.32	25.95	2.95
APE	HL	1.68	0.09	0.23	31.85	2.40
EVR	HL	1.88	0.10	0.30	57.00	3.40
GVD	HL	1.70	0.07	0.24	28.40	1.60
KEK	HL	1.62	0.10	0.19	32.90	4.33
KTHA	HL	1.92	0.06	0.31	45.80	2.20
KYMI	HL	1.90	0.12	0.31	23.30	3.08
KZN	HL	1.76	0.06	0.26	36.54	2.10
LIA	HL	1.72	0.06	0.24	27.95	1.32
NEO	HL	1.77	0.10	0.27	26.55	1.66
PLG	HL	1.78	0.06	0.27	29.70	1.45
RDO	HL	1.82	0.07	0.28	29.45	1.40
SKY	HL	1.65	0.08	0.21	26.05	1.78
SMG	HL	1.71	0.08	0.24	32.70	2.80

SMTH	HL	1.67	0.07	0.22	30.20	1.81
VLY	HL	1.58	0.07	0.17	31.00	2.20
PYL	HP	2.00	0.11	0.33	31.20	5.00
VLX	HP	1.89	0.07	0.31	51.35	2.81
ALN	HT	1.86	0.07	0.30	31.00	1.95
CHOS	HT	1.77	0.07	0.27	26.70	1.34
GRG	HT	1.64	0.08	0.20	35.10	1.68
IGT	HT	1.68	0.12	0.23	41.75	5.68
KAVA	HT	1.77	0.06	0.27	27.40	1.64
KRND	HT	2.00	0.05	0.33	28.25	1.23
PAIG	HT	1.80	0.09	0.28	24.90	2.19
SIGR	HT	1.92	0.14	0.31	23.15	3.78
SRS	HT	1.76	0.08	0.26	29.85	1.72

Table 7: Depth and Vp/Vs approximations for each station from the H-k stacking (Waterlevel deconvolution). In addition, the errors of each quantity and the final quality of each station are presented.

Station	Net	Vp/Vs Error	Error	Poisson Ratio (σ)	H (km) Moho	H Error
AXAR	HA	1.6	0.05	0.18	34.60	1.54
LOUT	HA	2.00	0.05	0.33	26.45	1.38
APE	HL	1.65	0.08	0.21	32.10	2.27
EVR	HL	1.88	0.05	0.30	56.65	3.20
GVD	HL	1.66	0.07	0.22	28.90	1.60
KEK	HL	1.65	0.07	0.21	31.20	2.34
KTHA	HL	1.96	0.04	0.32	44.90	1.80
KYMI	HL	1.90	0.09	0.31	23.70	1.52
KZN	HL	1.74	0.06	0.25	37.40	1.60
LIA	HL	1.72	0.07	0.24	27.85	1.53
NEO	HL	1.84	0.09	0.29	25.35	1.28
PLG	HL	1.80	0.05	0.28	28.55	1.15
RDO	HL	1.80	0.08	0.28	29.25	2.35
SKY	HL	1.67	0.08	0.22	25.40	1.58
SMG	HL	1.73	0.09	0.25	31.85	2.90
THL	HL	1.75	0.08	0.26	32.75	2.62
VLS	HL	1.99	0.06	0.33	25.85	1.50
VLY	HL	1.59	0.06	0.17	30.65	1.70
PYL	HP	2.00	0.11	0.33	31.55	5.41
SERG	HP	1.92	0.09	0.31	32.25	2.46
VLX	HP	1.90	0.05	0.31	51.00	2.45
ALN	HT	1.87	0.07	0.30	30.80	1.82
CHOS	HT	1.78	0.07	0.27	26.35	1.24
GRG	HT	1.64	0.06	0.20	35.20	1.26
IGT	HT	1.63	0.08	0.20	44.95	4.47
KAVA	HT	1.89	0.10	0.31	24.80	2.50

KRND	HT	2.00	0.02	0.33	27.95	0.63
NEST	HT	1.78	0.11	0.27	41.10	4.38
PAIG	HT	1.79	0.08	0.27	24.75	1.66
SIGR	HT	1.85	0.14	0.29	24.75	4.00
SRS	HT	1.85	0.08	0.29	30.05	2.19

3.4.3 Discussion

3.4.3.1 Crustal thickness in the Greek region

Based on the previous depth results, a Moho depth map was constructed using the Natural Neighbor interpolation tool from the commercial software ArcGIS. The Natural Neighbor algorithm uses geometrical relationships (Voronoi tessellation) in order to apply weights to the input dataset (Sibson 1981). The specific methodology provides a smoother result of the dataset's behavior compared to simpler interpolation methods, such as the IDW. The interpolated map is presented in Figure 50. The input dataset contains the defined depths from the H-k method and the depths by the Ps phases in the cases where the H-k failed to determine the Moho depth. In addition, this map incorporates only depths obtained from the Iterative deconvolution due to the fact that the latter are more stable and provide larger number of results with the H-k method.

The contour map reveals a general trend of Moho thickness increase from the eastern to western Greece. In more detail, the central and the northern Aegean exhibit Moho depths near or under 28 km. The depths slightly increase in the western part of the south Aegean, being close to 30 km. The eastern part of Crete is characterized by Moho depths that reach locally 40 km, which may possibly be an overestimated result. The Moho depths gradually increase, ending up to an extremely thick continental crust in western Greece that reaches 61 km. Large Moho depths (>40 km) dominate almost the entire part of the Peloponnese, a part of central Greece and a part of Macedonia. Three local crustal "maxima" (<50 km) can be determined, two in the Peloponnese and one in central Greece. The thick crust is terminated abruptly near the shoreline of western Greece and is reduced under 30 km near the western part of the subduction zone.

A relatively stable and flat Moho is present in the Aegean Sea. The Aegean Sea is described as a "back arc" region with notable geodynamical features. Due to the existence of these features, such as the continental crust and exhumation of high pressure rocks, Agostini et al. (2010) characterized the Aegean as an "atypical back arc". In general, the broader Aegean and Western Anatolian region is dominated by an extensive behavior. Many authors attempted to decode the extension in the Aegean Sea. McKenzie (1972) proposed that the extension can be justified by the Anatolia's escape to the west and by the collision of the Eurasian and African plates. Another scientific popular opinion comes from Pichon and Angelier (1979), who attribute this phenomenon to the slab retreat. No matter what, the extensional phenomena are reflected in the normal faulting (e.g. Chatzipetros et al. 2013), also evidenced by the focal mechanisms in the north and in the central Aegean (e.g. Kiratzi and Louvari 2003; Roumelioti et al. 2011). The regional extension in the Aegean Sea can be traced back approximately to Eocene-Early Miocene (Jolivet 2001). Since then,

there is an undergoing extensional deformation with no signs of oceanic crust until now. The current deformation pattern is in accordance with geodetic measurements. Plethora of geodetic studies support the existence of \sim N-S extension in the north Aegean (e.g. Floyd et al. 2010; Müller et al. 2013) and \sim NNE-SSW to \sim NE-SW in the central and south Aegean with strain free Cyclades (Kahle et al. 1998; Rontogianni 2010). The slow extending deformation has direct result the thinning of the crust that can be easily observed in the RF map for the whole Aegean region (Fig. 50).

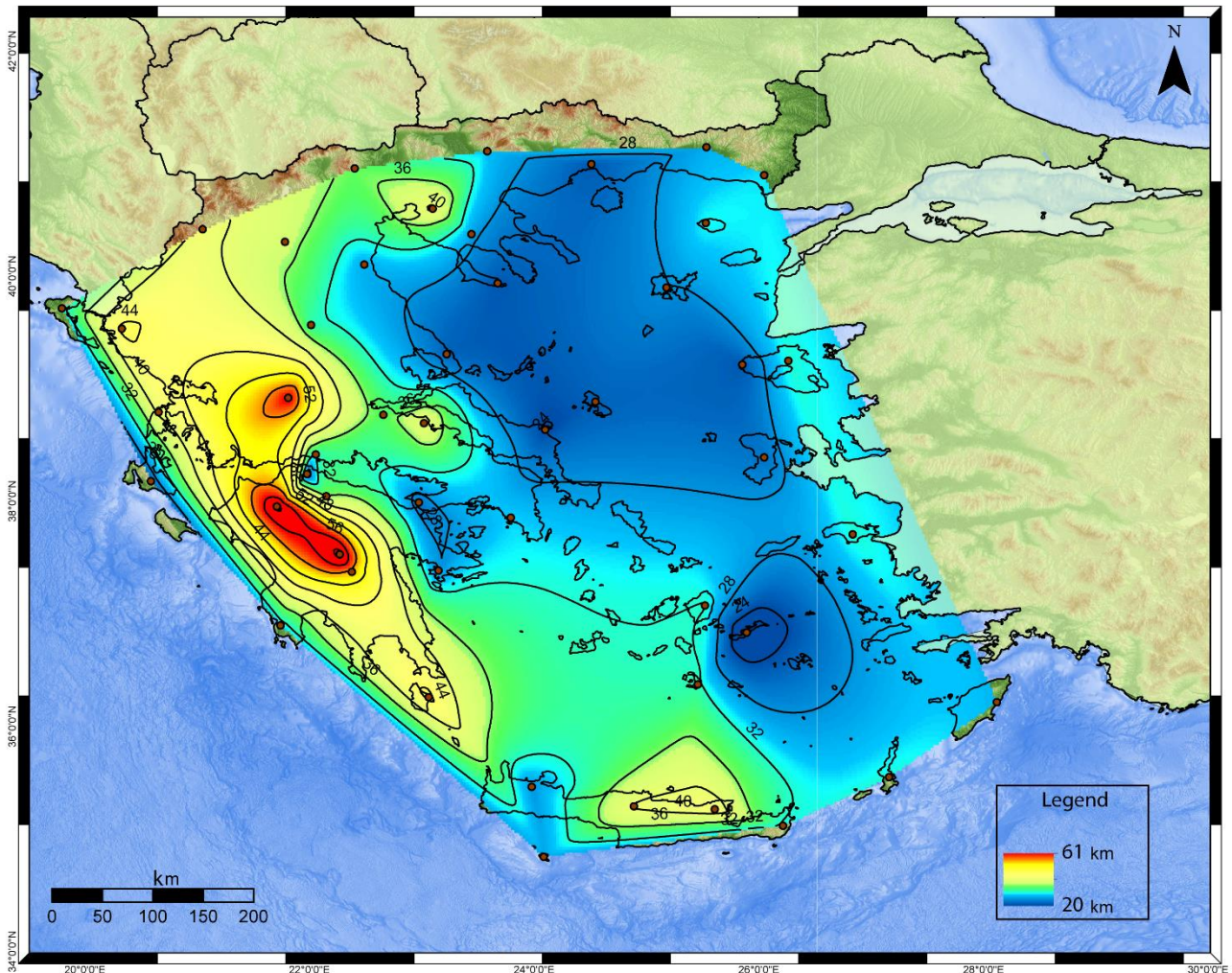


Figure 50: Crustal thickness of the Greek region based on the results obtained by the Iterative deconvolution.

In the southern part of the Aegean Sea and more precisely in the Crete Island there are wide variations from the previously described situation. The stations in Crete reveal a peculiar behavior of the observed RF, with the presence of negative amplitudes during the first 2-4 sec of the signal. Due to the proximity of Crete to the subduction zone, small Moho depths are expected. In contrast, the lack of positive conversions in the first seconds makes the hypothetic Moho depths unreasonably large. The specific phenomenon has been observed several times by previous RF studies in the same region. Li et al. (2003) reported the same “negative amplitudes” in two stations, one in the western and one in central Crete. They attribute this phenomenon to reversed velocity contrasts between the mantle and the crust due to hydration and serpetinization. Endrun et al. (2004), utilizing a dense network of stations in western Crete, also reported the negative phase in the first seconds. Along with a dispersion analysis, they interpreted this observation with the existence of a low-velocity material that flows and ejects from a channel in the subduction zone. Modelling the effects of Moho

topography to the RF in the region of Crete, Endrun et al. (2005) concluded that the negative phase could be in reality the Ps phase with a changed polarity due to special circumstances of the Moho's dip and the ray's incident angle.

In the present study the negative phase, except from the stations in Crete (IMMV, IDI, NPS and ZKR), is also identified in the station KTHA (Fig. 51). Therefore, the phenomenon is not limited in western Crete, as also noted by Sodoudi et al. (2006, 2015). Sodoudi et al. (2015) report a universality of this phenomenon in the Hellenic fore-arc area and support the serpentinization concept, similarly to the Cascadia area (e.g. Bostock 2013). Based on our results this is not exactly the case, taking into account that stations like KARP and GVD do not exhibit strong negative but weak positives phases (Fig. 51).

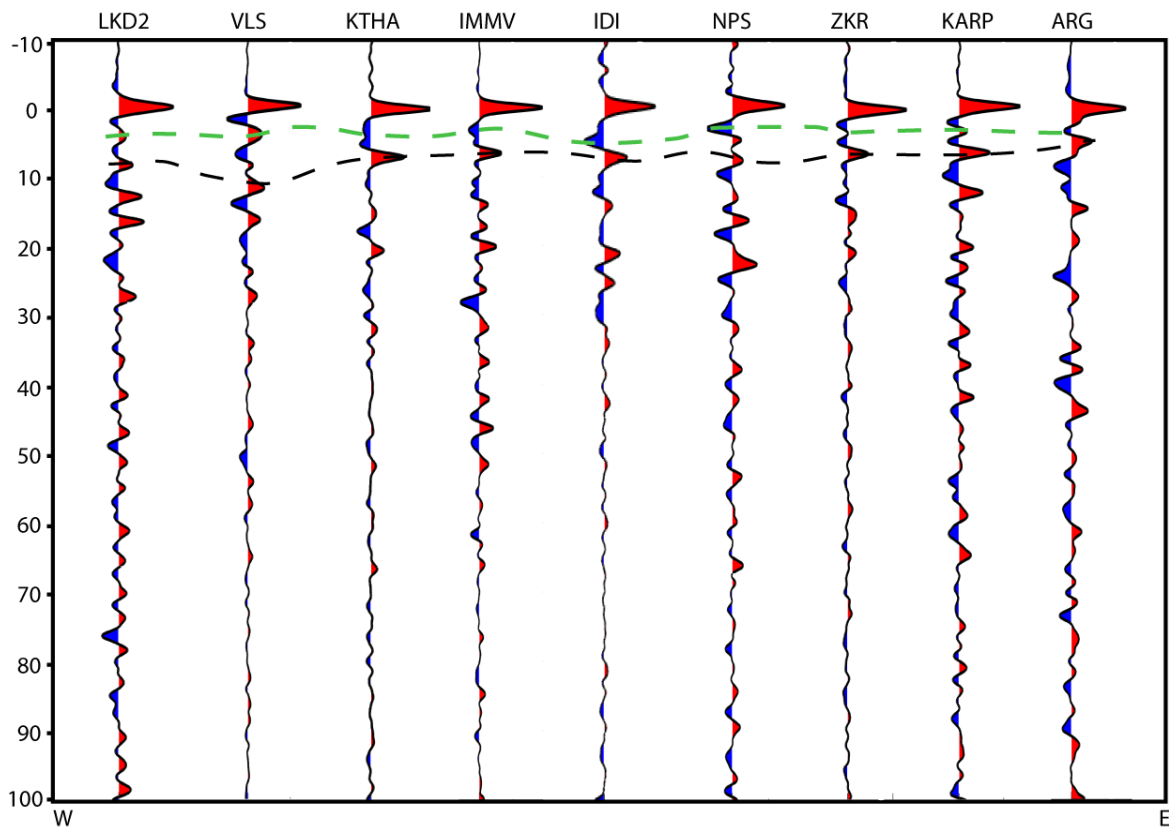


Figure 51: Stacked RF for the stations near the subduction zone from the east to the west, determined from the Iterative deconvolution. The green dashed line denotes the Moho Ps arrival time for each station, while the black dashed line the arrival of the Slab Ps phase.

The large time range availability of the present study's dataset allows a greater flexibility in the applied filters of the RF in contrast to Sodoudi et al. (2015) who applied stronger filters, affecting the RF's level of detail. In addition, both deconvolution methods are in agreement regarding the absence of negative phase observation in the KARP and GVD stations. At this point, any approach about the origin of the phenomenon that causes the negative phases is not supported by the study's data. However, this is not the case for the whole fore-arc region, having a more local and spatial limited character. For the GVD station, the linear stacked results for the Iterative and the Waterlevel deconvolution are presented in Figure 52. There are no signs of strong negative conversion, whereas

the signal presents two quite strong successive positive pulses in the first 4 sec, evidence of clear Moho boundaries signatures from the Aegean and the Slab. A part of the central and eastern Crete presents thicker crust compared to the western part. This diversification is not significant, but can partly be associated with a possible underestimation of the crustal thicknesses (western Crete) due to the above-mentioned complexity of the signals. Concluding, the interpretation of the Moho variations can possibly be connected with the characteristic uplift and the mass deficit in the western Crete (Snopek et al. 2007).

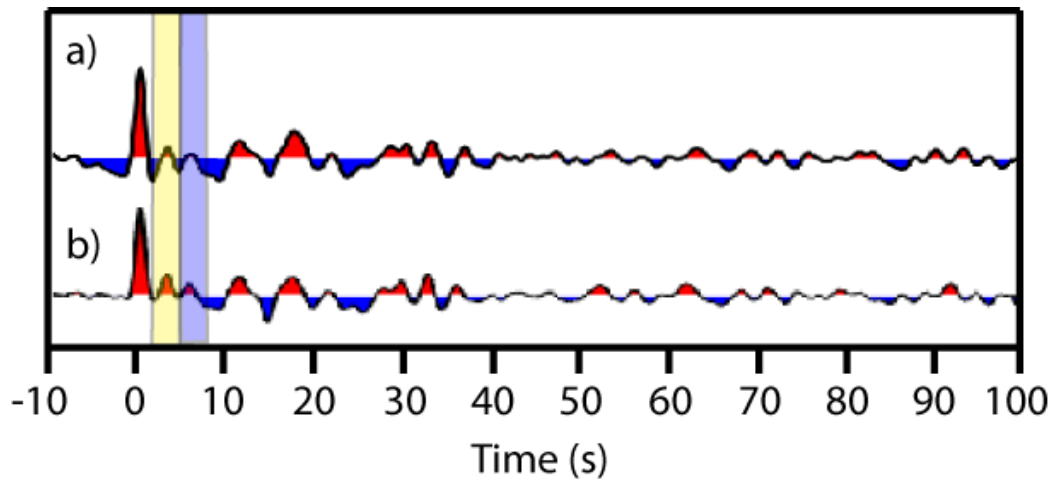


Figure 52: Stacked RF for the station GVD for the Waterlevel (a) and the Iterative deconvolution (b). Yellow and blue columns denote the possible positive conversions from the Aegean Moho and the Slab, respectively.

The crustal thickness in mainland Greece is significantly larger, compared to the Aegean and to the fore-arc region (Fig. 50). The Hellenides orogen is a part of the Alpine system. The Hellenides are separated into the northern and the southern part and they consist aftereffect of shortening by thrust stacking of paleogeographical units. In general, the southern Hellenides are characterized by lower topography compared to the northern, due to major extension from the Miocene (Burchfiel et al. 2008). A detailed explanation regarding the orogenic processes of the Hellenides system is beyond the scope of the present study. Readers are remit to other studies (e.g. Papanikolaou 2009; Papanikolaou 2013; Burchfiel et al. 2018) for more details about the specific scientific subject.

The current deformation situation in mainland Greece is characterized by extension in the largest part with quite a few rotations of the extensive directions. Extensional features (i.e. Amvrakikos, gulf of Corinth, Saronikos) constitute result of this extensional phenomenon (e.g. Drakatos et al. 2005a; Kassaras et al. 2016). The largest values of extension rates is observed in the western Gulf of Corinth, with also a discrete shear belt in the western Greece (Chousianitis et al. 2013, 2015). In case of Saronikos Gulf the crustal thinniking could be linked to paleo-volcanic activity (Drakatos et al. 2005b) The Moho depths present a significant increase in mainland Greece, reaching 50 - 60 km in certain parts of central Greece and the Pelopponese. The RF from these regions simply and clearly imprint the delay of the Ps phase. A typical example of delayed arrival of the Ps phase is presented in the Figure 53. Thus, the large Moho depths correlate very well with the surface topography of the Hellenides. The gradual increase of the crustal thickness from the Aegean to mainland Greece is separated by a transition zone with moderate Moho depths.

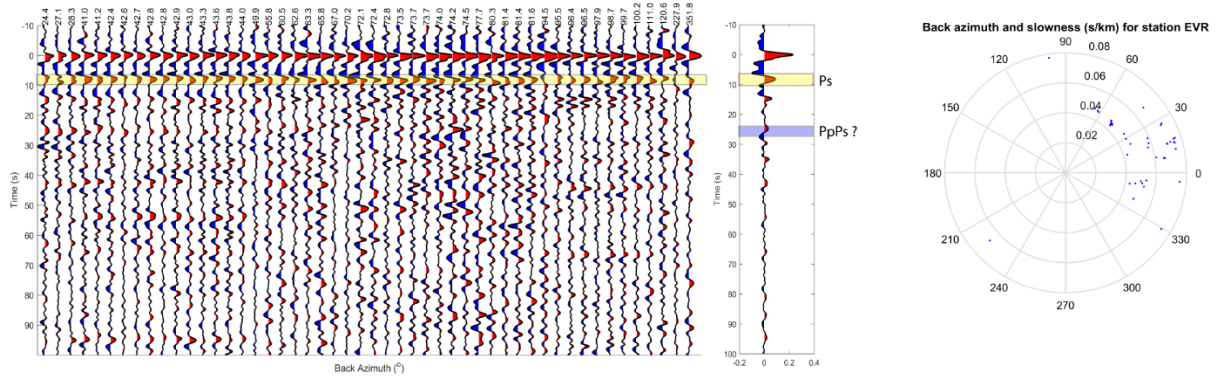


Figure 53: Radial RF for the EVR station, regularly spaced from the Waterlevel deconvolution with the linear stacked trace. Yellow and blue highlight colors indicate the Ps and the PpPs phase (?), respectively. To the right the backazimuthal distribution of the RF for each method is presented.

3.4.3.2 Crustal thickness - Comparison with previous studies

Moho depths have been determined by past studies using various geophysical methodologies. In this paragraph, Moho models from previous work will be compared with the presently obtained RF model. Studying the most recent bibliography, gravity data are often used for Moho models determination. Makris et al. (2013) approached the Moho depths distribution in the Greek region using gravity and seismic data. They determined a thick crust part in the northern Hellenides (Pindos Mountains) that in some parts exceeds 40 km. The thick crust “arrow” continues north to Albania and in the southern Hellenides with > 32 km thickness in the major part of Peloponnese. The Aegean domain preserves small depths (< 30 km) in the northern and in the southern part. Moho depths in Crete are close to 30 km. Moho depths are gradually increasing both in Turkey and the Hellenides region. Grigoriadis et al. (2016) from gravity data inversion reveal a similar picture. Important differences with the previously described model is the maximum Moho depth that exceeds the 45 km near the western Gulf of Corinth. Depths in the Aegean Sea are also smaller than 30 km and the thinnest crust is presented in the Cretan Sea (< 25 km).

A Moho depth map was produced by station delays from Pn tomographic inversion by Mutlu and Karabulut (2011). The specific approach displays major differences from the previously described models, mostly in western Greece, where the Moho depths increase continuously, uninterrupted by the subduction. The Hellenides exhibit depths around 40 km and the Aegean Sea lower than 30 km. The model by Mutlu and Karabulut (2011) is not characterized by extreme detail and can be used only for a generic view of the Moho distribution. Karagianni et al. (2005) and Karagianni and Papazachos (2007) determined the Moho depths in Greece using inversion of Rayleigh and joint inversion of Love and Rayleigh waves, respectively. In both cases, the visualized results are quite similar, with large Moho depths in western Greece (45-50 km) and smaller depths (22-25 km) in the Aegean Sea. A notable comment in their obtained maps is that the larger Moho depths are somewhat more to the west, compared with the results from gravity studies.

For the entire Greek area a 2-D Moho map using RF has been obtained only by Sodoudi et al. (2006). The same pattern with the previous studies is presented with thick crust in the Hellenides and thinner crust in the Aegean. There is an important difference in the quantitative part of observed depths, that are constantly below (in any region) from any other study, sign of a plausible under-

evaluation of the Moho. Nevertheless, the depth distribution patterns are similar with the rest of the studies. Except from Sodoudi et al. (2006), several RF studies were performed in smaller parts of Greece by Li et al. (2003), Meijde et al. (2003), Endrun et al. (2004), Cossette et al. (2016) and Sachpazi et al. (2016). These studies concerned mostly parts of the Aegean and the Peloponnese and exhibit results that are generally in agreement with our observations. Extremely important is to note that Sodoudi et al. (2015) displaying Moho depths in the Peloponnese area that reach 51 km, in contrast with their previous study according to which the maximum Moho depths were smaller than 40 km.

In general, the crustal thickness that has been determined in the present study is in a good agreement with the foregoing studies. Although, there are some significant differences in our Moho results that reveal maximum depths in the Hellenides that are in the range 50 - 60 km. A considerably similar case is observed in the northern Peloponnese by Sodoudi et al. (2015), reaching 51.5 km. A possible overestimation of few kilometers can be recognized, especially in cases that referenced models or relations like (3.2) are used.

3.4.3.3 Slab depths from RF Ps arrivals

Except from the Moho Ps arrivals, the RF signals also contain Ps arrivals from the slab, in cases where the rays propagate through the Hellenic slab. The identification of the slab Ps arrival was performed keeping in mind that the African Moho arrival is recorded few seconds after the Aegean Moho one. Both Ps phases usually display large amplitudes. As a result it is difficult to confuse them with the Aegean's Moho multiples. Table 5 contains all information regarding the arrival times and the determined depth of the slab for the stations where it was identified. The same results are also presented in Figure 54. The observed depths are generally in a good agreement with the superimposed isodepths. Serious deviation is observed in the AMGA station, possibly due to the low quality (C) of the obtained RF.

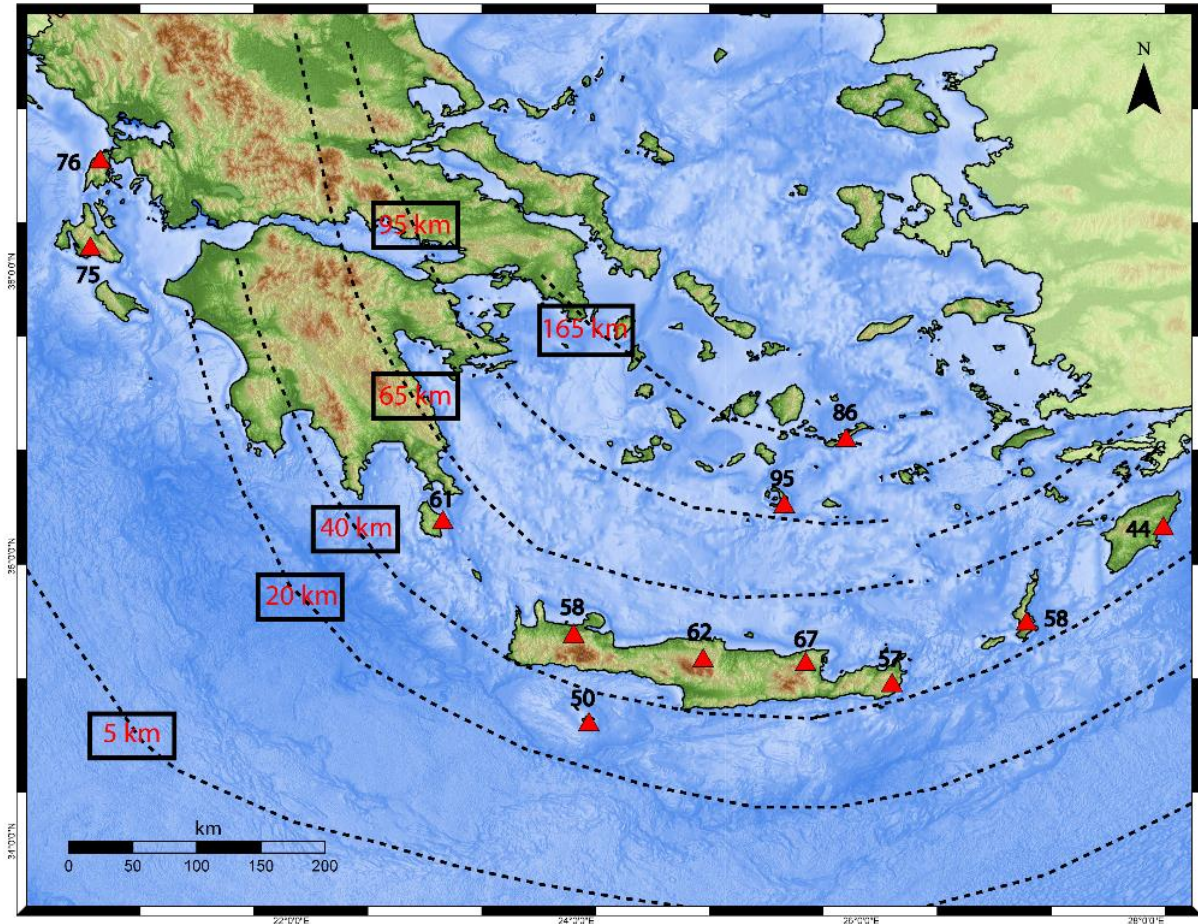


Figure 54: Depths of the African Moho from P RF. Red triangles denote station locations for which measurements were performed. Values of the determined depth is provided (check also table 5). The dashed lines symbolize the Hellenic slab isodepths from Bocchini et al. (2018).

3.4.3.4 V_p/V_s ratio

The spatial distribution of the V_p/V_s ratio based on the stacking method of Zhu and Kanamori (2000) is another important result of the present study. The V_p/V_s or the Poisson values (as determined from the relation) can lead to chemical and compositional approaches of the area beneath the station. Nevertheless, the V_p/V_s values from the RF are average values for the whole medium beneath the station. For that reason, it is appropriate to evaluate the results with caution. Figure 55 presents examples of the stacking method from three stations.

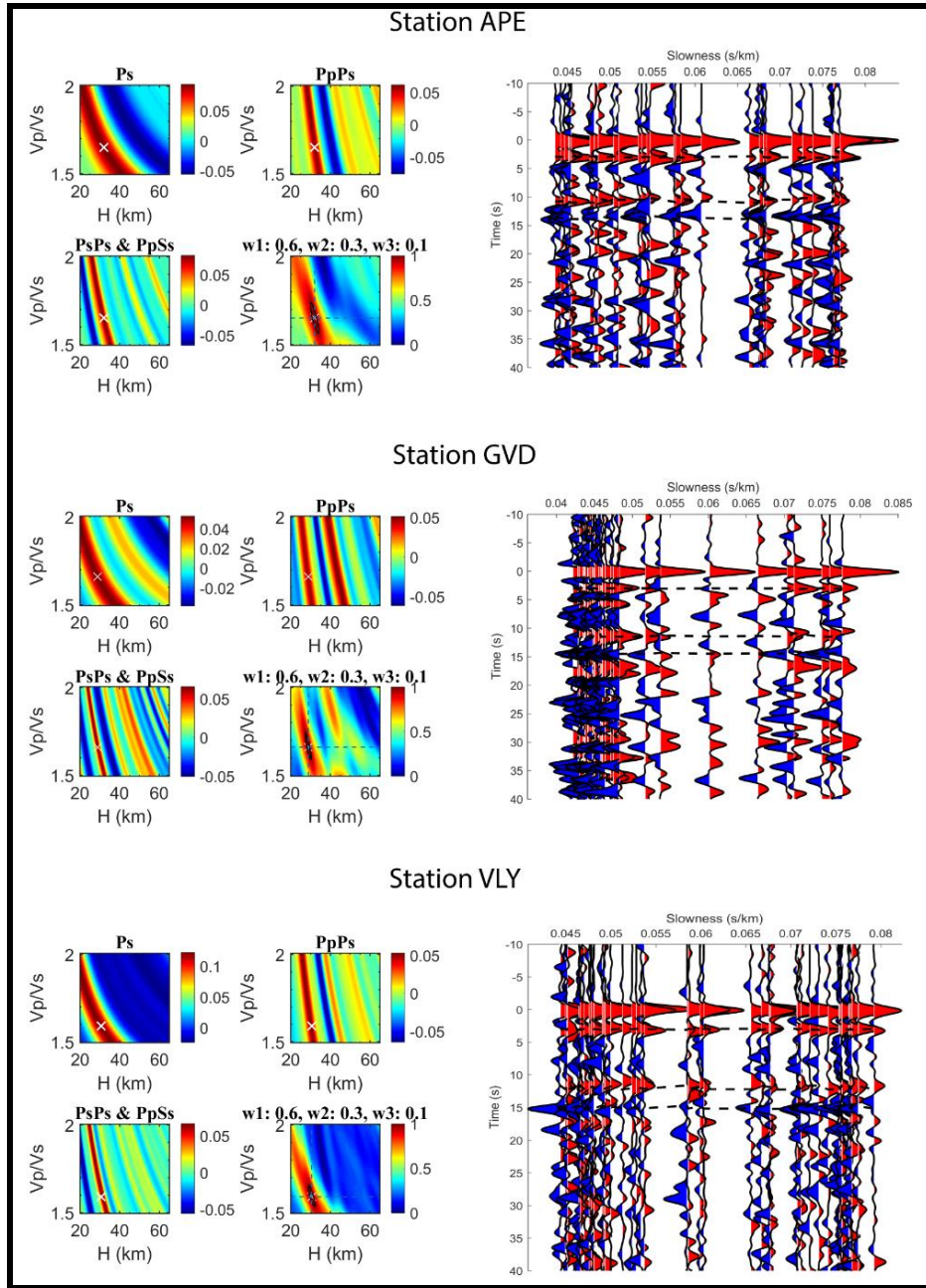


Figure 55: Results from the stacking method of Zhu and Kanamori (2000) from the stations VLY, APE and GVD. The left panel contains the depth and the Vp/Vs results while the right panel the assemblage of the RF with the predicted from the methodology arrival times of each phase (black dashed lines).

The Vp/Vs ratio results have been grouped into three categories and they are presented in the Figure 56. The largest part of the Greek region displays low and moderate ratios, except from the western part of Greece where high ratios were determined. The high ratios are indicator of possible partial melt in the crust (e.g. Christensen 1996). Our results are consistent with Sodoudi et al. (2015), in the overlapping examined areas, with some noticeable deviations. Sodoudi et al. (2015) applied the same method in the south Aegean and Peloponnesus. Compared to the current study Sodoudi et al. (2015) results reveal slightly lower ratios in the Peloponnesus. These deviations can possibly be connected to the different range of the available dataset, resulting to more robust result in our case. In addition, there is a possible correlation between the large Moho depths and the high Vp/Vs ratios. Halpaap et al. (2018) reports in the same area (Peloponnesus) high Vp/Vs ratios, especially in the

upper crust, with the existence of partial melting. A possible link between the increase of V_p/V_s ratios and the crustal thickness cannot be excluded, but a denser network is necessary for this approximation.

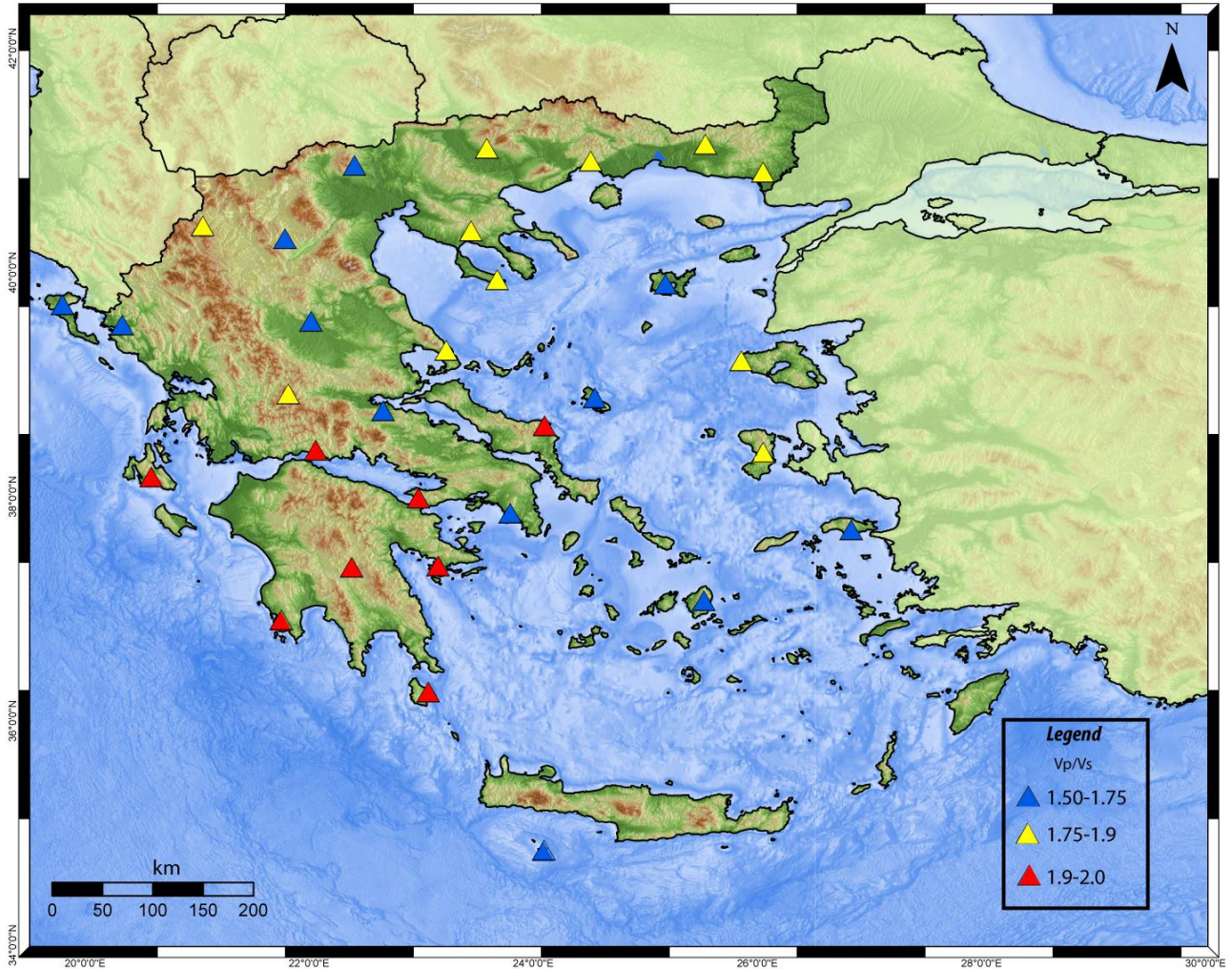


Figure 56: V_p/V_s ratio results for Greece. Blue triangles denote V_p/V_s range 1.50-1.75, yellow triangles 1.75-1.9 and red triangles 1.9-2.0.

Conclusions

The present study deploys two important methodologies in order to study in depth the geodynamic framework of the broader Greek region. The study of the shear-wave splitting phenomenon using the PKS and SKS phases had as a result a series of significant observations that are briefly summarized below:

- The plethora of the available measurements, verified the observations by Olive et al. (2014) and Evangelidis (2017) regarding the existence of an anisotropic zonation in the Greek region. This zonation is determined by the direction changes of the fast polarization axes (parallel or perpendicular to the trench).
- The observed zonation can be attributed to separate olivine layers with different polarization directions, similar to the proposed model by Faccenda and Capitanio (2013).
- Two possible slab windows (tears) have been identified, that cause significant changes in the mantle flow near the edges of the slab. The first tear is identified in the KTF and the other one near the RTF region. In both cases the inferred windows allow the mantle fabric to enter the mantle wedge area causing a significant toroidal flow (or inflow).
- SKS and PKS measurements yield similar results in most cases. Thus, the measurements are jointly interpreted.
- KZN and XOR stations resulted high number of null measurements. This phenomenon is attributed to the existence of a possible anisotropic transition zone.
- SKS/PKS results almost coincide with GPS measurements near the central-southern part of the Aegean Sea, due to plausible movement transmission from the mantle flow to crustal flow.

Significant results are also obtained by the application P-Receiver Function methodology which was performed using two different types of deconvolution methods, the Iterative and the Waterlevel one. The main conclusions of the RF study were:

- The determination of the crustal thickness in the Greek region. Large Moho depths were determined in the northern and southern Hellenides, with a gradual decrease towards the Aegean Sea. The observable depths are similar to previous geophysical studies that utilized seismic and gravity data.
- Both deconvolution methods produced satisfactory results but the most reliable ones concern the Iterative deconvolution.
- Except of the Ps arrival times from the Moho boundary, clear Ps arrivals from the African Moho were determined in stations in the vicinity of the subduction zone.
- Negative Ps conversions were identified in stations located near the subduction zone. This phenomenon concerns mostly the Crete island.
- Possible partial melting was identified in the Peloponnese peninsula, due to the high V_p/V_s ratio values. The rest of the Greek region presents a normal distribution of V_p/V_s ratio.

The present Master Thesis incorporates two different approaches in order to study parts of the broader geodynamical framework of the Greek region. However, these two independent methodologies can find common ground in specific scientific fields.

- The determined fast polarization directions coincide with the GPS directions only to a certain part of the central Aegean, where the Moho depths, determined by the RF technique, appear to be relative low, implying a possible intense coupling between the asthenosphere and lithosphere in the specific region. In other words, a possible direct movement transfer from the mantle to the crust exists. Forthwith, the rest of the lithospheric Greek region reveals a more independent behavior.
- As it is mentioned earlier, the anisotropy directions of the PKS/SKS phases appear to change orientation from trench perpendicular in the BA to trench parallel in the FA region. This change is accompanied by a high number of null measurements in stations XOR and KZN. In the same area the Moho depths rapidly increase towards the Hellenides. The specific anisotropical transitional area could be linked to the petrological alterations that follow the increasingly Moho depths. The accepted two layered fabric behavior by Faccenda and Capitanio (2013) may be related to this phenomenon. A development of the second layer fabric could take place in the specific area.

References

- Abramson EH, Brown JM, Slutsky LJ, Zaug J (1997) The elastic constants of San Carlos olivine to 17 GPa. *J Geophys Res* 102:12253. doi: 10.1029/97JB00682
- Abt DL, Fischer KM, Abers GA, Protti M, González V, Strauch W (2010) Constraints on upper mantle anisotropy surrounding the Cocos slab from SK(K)S splitting. *J Geophys Res Solid Earth* 115:1–16. doi: 10.1029/2009JB006710
- Agarwal NK, Jacoby WR, Berckhemer H (1976) Teleseismic p-wave traveltime residuals and deep structure of the Aegean region. *Tectonophysics* 31:33–57. doi: 10.1016/0040-1951(76)90166-9
- Agostinetti NP, Amato A (2009) Moho depth and Vp/Vs ratio in peninsular Italy from teleseismic receiver functions. *J Geophys Res* 114:1–17. doi: 10.1029/2008JB005899
- Agostini S, Doglioni C, Innocenti F, Manetti P, Tonarini S (2010) On the geodynamics of the Aegean rift. *Tectonophysics* 488:7–21. doi: 10.1016/j.tecto.2009.07.025
- Anderson DL (1961) Elastic wave propagation in layered anisotropic media. *J Geophys Res* 66:2953–2963. doi: 10.1029/JZ066i009p02953
- Anderson DL (1854) Theory of the Earth: Chapter 5. Anisotropy. *Notes Queries* s1–IX:89. doi: 10.1093/nq/s1-IX.222.89-a
- Armijo R, Meyer B, Hubert A, Barka A (1999) Westward propagation of the North Anatolian fault into the northern Aegean: Timing and kinematics. *Geology* 27:267–270. doi: 10.1130/0091-7613(1999)027<0267:WPOTNA>2.3.CO;2
- Baccheschi P, Margheriti L, Steckler MS (2008) SKS splitting in Southern Italy: Anisotropy variations in a fragmented subduction zone. *Tectonophysics* 462:49–67. doi: 10.1016/j.tecto.2007.10.014
- Baccheschi P, Margheriti L, Steckler MS, Boschi E (2011) Anisotropy patterns in the subducting lithosphere and in the mantle wedge: A case study - The southern Italy subduction system. *J Geophys Res Solid Earth* 116:1–15. doi: 10.1029/2010JB007961
- Backus G (1962) Long-Wave Elastic Anisotropy Produced by Horizontal Layering explained by vertical variations in isotropic. *67:4427–4440*
- Barruol G, Mainprice D (1993) A quantitative evaluation of the contribution of crustal rocks to the shear-wave splitting of teleseismic SKS waves. *Phys Earth Planet Inter* 78:281–300. doi: 10.1016/0031-9201(93)90161-2
- Barruol G, Silver PG, Vauchez A (1997a) Seismic anisotropy in the eastern United States: Deep structure of a complex continental plate. *J Geophys Res Earth* 102:8329–8348. doi: 10.1029/96jb03800
- Barruol G, Silver PG, Vauchez A (1997b) Seismic anisotropy in the eastern United States: Deep structure of a complex continental plate. *J Geophys Res* 102:8329. doi: 10.1029/96JB03800
- Behn MD, Conrad CP, Silver PG (2004) Detection of upper mantle flow associated with the African Superplume. *Earth Planet Sci Lett* 224:259–274. doi: 10.1016/j.epsl.2004.05.026

- Bellahsen N, Jolivet L, Lacombe O, Bellanger M, Boutoux A, Garcia S, Mouthereau F, Le Pourhiet L, Gumiaux C (2012) Mechanisms of margin inversion in the external Western Alps: Implications for crustal rheology. *Tectonophysics* 560–561:62–83. doi: 10.1016/j.tecto.2012.06.022
- Berens P (2009) Circular Statistics Matlab Toolbox. *J Stat Softw* 31:1–21
- Berk Biryol C, Beck SL, Zandt G, Özacar AA (2011) Segmented African lithosphere beneath the Anatolian region inferred from teleseismic P-wave tomography. *Geophys J Int* 184:1037–1057. doi: 10.1111/j.1365-246X.2010.04910.x
- Bianco F, Castellano M, Milano G, Vilardo G, Ferrucci F, Gresta S (1999) The seismic crises at Mt. Vesuvius during 1995 and 1996. *Phys Chem Earth, Part A Solid Earth Geod* 24:977–983. doi: 10.1016/S1464-1895(99)00145-3
- Bocchini GM, Brüstle A, Becker D, Meier T, van Keken PE, Ruscic M, Papadopoulos GA, Rische M, Friederich W (2018) Tearing, segmentation, and backstepping of subduction in the Aegean: New insights from seismicity. *Tectonophysics* 734–735:96–118. doi: 10.1016/j.tecto.2018.04.002
- Bostock MG (2013) The Moho in subduction zones. *Tectonophysics*
- Bowman JR, Ando MA (1987) Shear-wave splitting in the upper mantle wedge above the Tonga subduction zone. *Geophys J R A S* 88:24–41
- Burchfiel BC, Nakov R, Dumurdzanov N, Papanikolaou D, Tzankov T, Serafimovski T, King RW, Kotzev V, Todosov A, Nurce B (2008) Evolution and dynamics of the Cenozoic tectonics of the South Balkan extensional system. *Geosphere*. doi: 10.1130/GES00169.1
- Burchfiel BC, Royden LH, Papanikolaou D, Pearce FD (2018) Crustal development within a retreating subduction system: The Hellenides. *Geosphere*. doi: 10.1130/GES01573.1
- Chatzipetros A, Kiratzi A, Sboras S, Zouros N, Pavlides S (2013) Active faulting in the north-eastern Aegean Sea Islands. *Tectonophysics*. doi: 10.1016/j.tecto.2012.11.026
- Chevrot S (2000) Multichannel analysis of shear wave splitting. *J Geophys Res* 105:21,579–21,592
- Chousianitis K, Ganas A, Evangelidis CP (2015) *Journal of Geophysical Research: Solid Earth*. 3909–3931. doi: 10.1002/2014JB011762.
- Chousianitis K, Ganas A, Gianniou M (2013) Kinematic interpretation of present-day crustal deformation in central Greece from continuous GPS measurements. *J Geodyn* 71:1–13. doi: 10.1016/j.jog.2013.06.004
- Christensen NI (1996) Poisson's ratio and crustal seismology. *J Geophys Res Solid Earth* 101:3139–3156. doi: 10.1029/95JB03446
- Clayton RW, Wiggins RA (1976) Source shape estimation and deconvolution of teleseismic bodywaves. *Geophys J R astr Sos* 47:151–177
- Confal JM, Eken T, Tilmann F, Yolsal-Çevikbilen S, Çubuk-Sabuncu Y, Saygin E, Taymaz T (2016) Investigation of mantle kinematics beneath the Hellenic-subduction zone with teleseismic direct shear waves. *Phys Earth Planet Inter* 261:141–151. doi: 10.1016/j.pepi.2016.10.012
- Cossette É, Audet P, Schneider D, Grasemann B (2016) Structure and anisotropy of the crust in the Cyclades, Greece, using receiver functions constrained by in situ rock textural data. *J Geophys Res Solid Earth*. doi: 10.1002/2015JB012460

- Crampin S (1978) Seismic-wave propagation through a cracked solid: polarization as a possible dilatancy diagnostic. *Geophys J R Astron Soc* 53:467–496. doi: 10.1111/j.1365-246X.1978.tb03754.x
- Crampin S, Chastin S (2003) A review of shear wave splitting in the crack-critical crust. *Geophys J Int* 155:221–240. doi: 10.1046/j.1365-246X.2003.02037.x
- Crampin S, Volti T, Stefánsson R (1999) A successfully stress-forecast earthquake. *Geophys J Int* 138:. doi: 10.1046/j.1365-246X.1999.00891.x
- Currie CA, Cassidy JF, Hyndman RD, Bostock MG (2004) Shear wave anisotropy beneath the Cascadia subduction zone and western North American craton. *Geophys J Int* 157:341–353. doi: 10.1111/j.1365-246X.2004.02175.x
- Drakatos G, Drakopoulos J (1991) 3-D velocity structure beneath the crust and upper mantle of Aegean Sea region. *PAGEOPH* 135:3.
- Drakatos G, Karantonis G, Stavrakakis G (1997) P-wave crustal Tomography of Greece with use of an accurate 2-point ray tracer. *Annali di Geofisica* 1: 25 – 36.
- Drakatos G, Voulgaris N, Pirli M, Melis N, Karakostas B (2005a) 3-D crustal velocity structure in Northwestern Greece. *Pure and Applied Geophysics* 162. doi: 10.1007/s00024-004-2578-2
- Drakatos G, Karastathis V, Makris J, Papoulia J, Stavrakakis G (2005b) 3D crustal structure in the neotectonic basin of the Gulf of Saronikos (Greece). *Tectonophysics* 400: 55-65.
- Dugda MT, Nyblade AA, Julia J, Langston CA, Ammon CJ, Simiyu S (2005) Crustal structure in Ethiopia and Kenya from receiver function analysis: Implications for rift development in eastern Africa. *J Geophys Res Solid Earth* 110:1–15. doi: 10.1029/2004JB003065
- Eaton DW, Dineva S, Mereu R (2006) Crustal thickness and VP/VS variations in the Grenville orogen (Ontario, Canada) from analysis of teleseismic receiver functions. *Tectonophysics* 420:223–238. doi: 10.1016/j.tecto.2006.01.023
- Endrun B, Ceranna L, Meier T, Bohnhoff M, Harjes H (2005) Modeling the influence of Moho topography on receiver functions: A case study from the central Hellenic subduction zone. 32:1–5. doi: 10.1029/2005GL023066
- Endrun B, Lebedev S, Meier T, Tirel C, Friederich W (2011) Complex layered deformation within the Aegean crust and mantle revealed by seismic anisotropy. *Nat Geosci* 4:203–207. doi: 10.1038/ngeo1065
- Endrun B, Meier T, Bischoff M, Harjes H (2004) Lithospheric structure in the area of Crete constrained by receiver functions and dispersion analysis of Rayleigh phase velocities MY IN ST. *Geophys J Int* 592–608 . doi: 10.1111/j.1365-246X.2004.02332.x
- Evangelidis CP (2017) Seismic anisotropy in the Hellenic subduction zone: Effects of slab segmentation and subslab mantle flow. *Earth Planet Sci Lett* 480:97–106. doi: 10.1016/j.epsl.2017.10.003
- Evangelidis CP, Liang WT, Melis NS, Konstantinou KI (2011) Shear wave anisotropy beneath the Aegean inferred from SKS splitting observations. *J Geophys Res Solid Earth* 116:1–14. doi: 10.1029/2010JB007884
- Faccenda M, Burlini L, Gerya T V., Mainprice D (2008) Fault-induced seismic anisotropy by hydration in subducting oceanic plates. *Nature* 455:1097–1100. doi: 10.1038/nature07376

- Faccenda M, Capitanio FA (2013) Seismic anisotropy around subduction zones: Insights from three-dimensional modeling of upper mantle deformation and SKS splitting calculations. *Geochemistry, Geophysics Geosystems* 14:243–262. doi: 10.1002/ggge.20055
- Faccenna C, Becker TW, Auer L, Billi A, Boschi L, Brun JP, Capitanio FA, Funiciello F, Horvath F, Jolivet L, Piromallo C, Royden L, Rossetti F, Serpelloni E (2014) Mantle dynamics in the Mediterranean. *Rev Geophys* 52:283–332. doi: 10.1002/2013RG000444.Received
- Faccenna C, Jolivet L, Piromallo C, Morelli A (2003) Subduction and the depth of convection in the Mediterranean mantle. *J Geophys Res Solid Earth* 108: . doi: 10.1029/2001JB001690
- Floyd MA, Billiris H, Paradissis D, Veis G, Avallone A, Briole P, McClusky S, Nocquet JM, Palamartchouk K, Parsons B, England PC (2010) A new velocity field for Greece: Implications for the kinematics and dynamics of the Aegean. *J Geophys Res Solid Earth* 115:1–25. doi: 10.1029/2009JB007040
- Forsyth DW (1975) The Early Structural Evolution and Anisotropy of the Oceanic Upper Mantle. *Geophys J R Astron Soc* 43:103–162 . doi: 10.1111/j.1365-246X.1975.tb00630.x
- Fouch MJ, Rondenay S (2006) Seismic anisotropy beneath stable continental interiors. *Phys Earth Planet Inter* 158:292–320. doi: 10.1016/j.pepi.2006.03.024
- Fukao Y (1984) Evidence from core-reflected shear waves for anisotropy in the Earth's mantle. *Nature* 309:695–698. doi: 10.1038/309695a0
- Ganas A, Oikonomou IA, Tsimi C (2017) NOAfaults: a digital database for active faults in Greece. *Bull Geol Soc Greece* 47:518. doi: 10.12681/bgsg.11079
- Govers R, Fichtner A (2016) Signature of slab fragmentation beneath Anatolia from full-waveform tomography. *Earth Planet Sci Lett* 450:10–19. doi: 10.1016/j.epsl.2016.06.014
- Govers R, Wortel MJR (2005) Lithosphere tearing at STEP faults: Response to edges of subduction zones. *Earth Planet Sci Lett* 236:505–523. doi: 10.1016/j.epsl.2005.03.022
- Grigoriadis VN, Tziavos IN, Tsokas GN, Stampolidis A (2016) Gravity data inversion for Moho depth modeling in the Hellenic area. *Pure Appl Geophys*. doi: 10.1007/s00024-015-1174-y
- Guillaume B, Husson L, Funiciello F, Faccenna C (2013) The dynamics of laterally variable subductions: Laboratory models applied to the Hellenides. *Solid Earth* 4:179–200. doi: 10.5194/se-4-179-2013
- Halpaap F, Rondenay S, Ottemöller L (2018) Seismicity, Deformation, and Metamorphism in the Western Hellenic Subduction Zone: New Constraints From Tomography. *J Geophys Res Solid Earth* 0: . doi: 10.1002/2017JB015154
- Hatzfeld D, Karagianni E, Kassaras I, Kiratzi a., Louvari E, Lyon-Caen H, Makropoulos K, Papadimitriou P, Bock G, Priestley K (2001) Shear wave anisotropy in the upper mantle beneath the Aegean related to internal deformation. *J Geophys Res* 106:30737. doi: 10.1029/2001JB000387
- Helbig K (1984) Anisotropy and dispersion in periodically layered media. *Geophysics* 49:364–373. doi: 10.1190/1.1441672
- Hess H (1964) Seismic Anisotropy of the Uppermost Mantle under Oceans. *Nature* 203:629–631. doi: 10.1038/203629a0
- Hollenstein C, Müller MD, Geiger A, Kahle HG (2008) Crustal motion and deformation in Greece

- from a decade of GPS measurements, 1993-2003. *Tectonophysics* 449:17–40. doi: 10.1016/j.tecto.2007.12.006
- Ismail W Ben, Mainprice D (1998) An olivine fabric database: An overview of upper mantle fabrics and seismic anisotropy. *Tectonophysics* 296:145–157. doi: 10.1016/S0040-1951(98)00141-3
- Jackson J, McKenzie D (1984) Active tectonics of the Alpine–Himalayan Belt between western Turkey and Pakistan. *Geophys J R Astron Soc* 77:185–264. doi: 10.1111/j.1365-246X.1984.tb01931.x
- Jolivet L (2001) A comparison of geodetic and finite strain pattern in the Aegean, geodynamic implications. *Earth Planet Sci Lett* 187:95–104. doi: 10.1016/S0012-821X(01)00277-1
- Jolivet L, Brun JP (2010) Cenozoic geodynamic evolution of the Aegean. *Int J Earth Sci* 99:109–138. doi: 10.1007/s00531-008-0366-4
- Jolivet L, Faccenna C, Goffé B, Burov E, Agard P (2003) Subduction tectonics and exhumation of high-pressure metamorphic rocks in the Mediterranean orogens. *Am J Sci* 303:353–409. doi: 10.2475/ajs.303.5.353
- Jolivet L, Faccenna C, Huet B, Labrousse L, Le Pourhiet L, Lacombe O, Lecomte E, Burov E, Denèle Y, Brun JP, Philippon M, Paul A, Salaün G, Karabulut H, Piromallo C, Monié P, Gueydan F, Okay AI, Oberhänsli R, Pourteau A, Augier R, Gadenne L, Driussi O (2013) Aegean tectonics: Strain localisation, slab tearing and trench retreat. *Tectonophysics* 597–598:1–33. doi: 10.1016/j.tecto.2012.06.011
- Jolivet L, Menant A, Sternai P, Rabillard A, Arbaret L, Augier R, Laurent V, Beaudoin A, Grasmann B, Huet B, Labrousse L, Le Pourhiet L (2015) The geological signature of a slab tear below the Aegean. *Tectonophysics* 659:166–182. doi: 10.1016/j.tecto.2015.08.004
- Jung H, Karato SI (2001) Water-induced fabric transitions in olivine. *Science* (80-) 293:1460–1463. doi: 10.1126/science.1062235
- Jung H, Katayama I, Jiang Z, Hiraga T, Karato S (2006) Effect of water and stress on the lattice-preferred orientation of olivine. *Tectonophysics* 421:1–22. doi: 10.1016/j.tecto.2006.02.011
- Jung H, Mo W, Green HW (2009) Upper mantle seismic anisotropy resulting from pressure-induced slip transition in olivine. *Nat Geosci* 2:73–77. doi: 10.1038/ngeo389
- Kapetanidis V, Deschamps A, Papadimitriou P, Matrullo E, Karakonstantis A, Bozionelos G, Kaviris G, Serpetsidaki A, Lyon-caen H, Voulgaris N, Bernard P, Sokos E, Makropoulos K (2015) The 2013 earthquake swarm in Helike, Greece: Seismic activity at the root of old normal faults. *Geophys J Int* 202:2044–2073. doi: 10.1093/gji/ggv249
- Kahle HG, Straub C, Reilinger R, McClusky S, King R, Hurst K, Veis G, Kastens K, Cross P (1998) The strain rate field in the eastern Mediterranean region, estimated by repeated GPS measurements. *Tectonophysics*. doi: 10.1016/S0040-1951(98)00102-4
- Kaneshima S, Ito H, Sugihara M (1988) Shear-wave splitting observed above small earthquakes in a geothermal area of Japan. *Geophys J* 94:399–411. doi: 10.1111/j.1365-246X.1988.tb02263.x
- Karagianni EE, Papazachos CB (2007) Shear velocity structure in the Aegean region obtained by joint inversion of Rayleigh and Love waves. *Geol Soc London, Spec Publ* 291:159–181 . doi: 10.1144/SP291.8
- Karagianni EE, Papazachos CB, Panagiotopoulos DG, Suhadolc P, Vuan A, Panza GF (2005) Shear

velocity structure in the Aegean area obtained by inversion of Rayleigh waves. *Geophys J Int* 160:127–143. doi: 10.1111/j.1365-246X.2005.02354.x

- Karakonstantis A (2017) 3-D simulation of crust and upper mantle structure in the broader Hellenic area through Seismic Tomography. Dissertation, National and Kapodistrian University of Athens.
- Karakostas V, Papadimitriou E, Karakaisis G, Papazachos C, Scordilis E, Vargemezis G, Aidona E (2003) The 2001 Skyros, Northern Aegean, Greece, earthquake sequence: off-fault aftershocks, tectonic implications, and seismicity triggering. *Geophys Res Lett* 30:10–13. doi: 10.1029/2002GL015814
- Karakostas V, Papadimitriou E, Mesimeri M, Gkarlaouni C, Paradisopoulou P (2015) The 2014 Kefalonia Doublet (M_w 6.1 and M_w 6.0), Central Ionian Islands, Greece: Seismotectonic Implications along the Kefalonia Transform Fault Zone. *Acta Geophys.* 63: 1. doi: 10.2478/s11600-014-0227-4
- Karato S, Wu P (1993) Rheology of the Upper Mantle: A Synthesis. *Science* (80-) 260:771–778. doi: 10.1126/science.260.5109.771
- Karato S, Jung H, Katayama I, Skemer P (2008) Geodynamic Significance of Seismic Anisotropy of the Upper Mantle: New Insights from Laboratory Studies. *Annu Rev Earth Planet Sci* 36:59–95. doi: 10.1146/annurev.earth.36.031207.124120
- Karato S, Zhang S, Wenk H-R (1995) Superplasticity in Earth's Lower Mantle: Evidence from Seismic Anisotropy and Rock Physics. *Science* (80-) 270:458–461. doi: 10.1126/science.270.5235.458
- Karato S (2008) Deformation of earth materials: An introduction to the rheology of solid earth
- Kassaras I, Kapetanidis V, Karakonstantis A (2016) On the spatial distribution of seismicity and the 3D tectonic stress field in western Greece, *Physics and Chemistry of the Earth* 95: 50-72. doi: 10.1016/j.pce.2016.03.012.
- Kassaras I, Kapetanidis V (2018) Resolving the Tectonic Stress by the Inversion of Earthquake Focal Mechanisms. Application in the Region of Greece. A Tutorial. In: Sebastiano D' Amico (ed) *Moment Tensor Solutions: A Useful Tool for Seismotectonics*, 1st edn. Springer International Publishing AG, pp 405-452
- Kaviris G, Papadimitriou P, Kravvariti P, Kapetanidis V, Karakonstantis A, Voulgaris N, Makropoulos K (2015) A detailed seismic anisotropy study during the 2011-2012 unrest period in the Santorini Volcanic Complex. *Phys. Earth Planet. Inter.* 238: 51–88. doi: 10.1016/j.pepi.2014.11.002
- Kaviris G, Spingos I, Kapetanidis V, Papadimitriou P, Voulgaris N, Makropoulos K (2017) Upper crust seismic anisotropy study and temporal variations of shear wave splitting parameters in the western Gulf of Corinth (Greece) during 2013. *Phys Earth Planet Inter* 269:148–164. doi: 10.1016/j.pepi.2017.06.006
- Kaviris G, Millas C, Spingos I, Kapetanidis V, Fountoulakis I, Papadimitriou P, Voulgaris N, Makropoulos K (2018) Observations of shear-wave splitting parameters in the Western Gulf of Corinth focusing on the 2014 $M_w = 5.0$ earthquake. *Phys. Earth Planet. Inter.* 282: 60 – 76. doi: 10.1016/j.pepi.2018.07.005

- Katayama I, Hirauchi KI, Michibayashi K, Ando JI (2009) Trench-parallel anisotropy produced by serpentine deformation in the hydrated mantle wedge. *Nature* 461:1114–1117 . doi: 10.1038/nature08513
- Kendall J-M, Silver PG (1998) Investigating Causes of D" Anisotropy. *Core-Mantle Bound Reg* 97–118. doi: 10.1029/GD028p0097
- Kern H (1990) Laboratory seismic measurements: an aid in the interpretation of seismic field data. *Terra Nov* 2:617–628 . doi: 10.1111/j.1365-3121.1990.tb00127.x
- Kikuchi K, Kanamori H (1982) Inversion of complex body waves. *Bull. Seismol. Soc. Am.* 72: 491–506
- Kind R, Yuan X, Kumar P (2012) Tectonophysics Seismic receiver functions and the lithosphere – asthenosphere boundary. *Tectonophysics* 536–537:25–43. doi: 10.1016/j.tecto.2012.03.005
- Kiratzi A, Louvari E (2003) Focal mechanisms of shallow earthquakes in the Aegean Sea and the surrounding lands determined by waveform modelling: A new database. *J Geodyn* 36:251–274. doi: 10.1016/S0264-3707(03)00050-4
- Kneller EA, Van Keken PE (2008) Effect of three-dimensional slab geometry on deformation in the mantle wedge: Implications for shear wave anisotropy. *Geochemistry, Geophys Geosystems* 9:1-21. <https://doi.org/10.1029/2007GC001677>
- Kouskouna V, Makropoulos K, Tsiknakis K (1993) Contribution of historical information to a realistic seismicity and hazard assessment of an area. The Ionian Islands earthquakes of 1767 and 1769: historical investigation. In: Stucchi, M. (Ed.) *Historical Investigation of European earthquakes, Materials of the CEC project Review of Historical Seismicity in Europe*, 1:195–206
- Kouskouna V, Sakkas G (2013) The University of Athens Hellenic Macroseismic Database (HMDB.UoA): historical earthquakes. *J. Seismol.* 17 (4): 1253-1280.
- Kreemer C, Blewitt G, Klein EC (2014) A geodetic plate motion and Global Strain Rate Model. *Geochemistry, Geophys Geosystems* 15:3849–3889. doi: 10.1002/2014GC005407
- Kreemer C, Chamot-Rooke N, Le Pichon X (2004) Constraints on the evolution and vertical coherency of deformation in the Northern Aegean from a comparison of geodetic, geologic and seismologic data. *Earth Planet Sci Lett* 225:329–346. doi: 10.1016/j.epsl.2004.06.018
- Kumar P, Kind R, Yuan X (2010) Receiver function summation without deconvolution. *Geophys J Int* 180:1223–123 . doi: 10.1111/j.1365-246X.2009.04469.x
- Langston CA (1979) Structure Under Mount Rainer, Washington, Inferred From Teleseismic Body Waves. *J Geophys Res* 84.
- Lay T, Wallace T (1995) *Global Modern Seismology*. Elsevier.
- Levin V, Droznin D, Park J, Gordeev E (2004) Detailed mapping of seismic anisotropy with local shear waves in southeastern Kamchatka. *Geophys J Int* 158:1009–1023. doi: 10.1111/j.1365-246X.2004.02352.x
- Li X, Bock G, Vafidis A, Kind R, Harjes H, Hanka W, Wylegalla K, Meijde M Van Der, Yuan X (2003) Receiver function study of the Hellenic subduction zone: imaging crustal thickness variations and the oceanic Moho of the descending African lithosphere. 733–748
- Li Y, Gao M, Wu Q (2014) Crustal thickness map of the Chinese mainland from teleseismic receiver

- functions. *Tectonophysics* 611:51–60. doi: 10.1016/j.tecto.2013.11.019
- Ligorria P, Ammon CJ (1999) Iterative Deconvolution and Receiver-Function Estimation. *Bull Seismol Soc Am* 89, 5:1395–1400
- Liu KH, Gao SS (2013) Making reliable shear-wave splitting measurements. *Bull Seismol Soc Am* 103:2680–2693. doi: 10.1785/0120120355
- Lombardi D, Braunmiller J, Kissling E, Giardini D (2008) Moho depth and Poisson's ratio in the Western-Central Alps from receiver functions. *Geophys J Int* 173:249–264. doi: 10.1111/j.1365-246X.2007.03706.x
- Long MD (2009) Complex anisotropy in D'' beneath the eastern Pacific from SKS-SKKS splitting discrepancies. *Earth Planet Sci Lett* 283:181–189. doi: 10.1016/j.epsl.2009.04.019
- Long MD (2013) Constraints on subduction geodynamics from seismic anisotropy. *Rev Geophys* 51:76–112 . doi: 10.1002/rog.20008
- Long MD, Becker TW (2010) Mantle dynamics and seismic anisotropy. *Earth Planet Sci Lett* 297:341–354 . doi: 10.1016/j.epsl.2010.06.036
- Long MD, Silver PG (2009a) Shear wave splitting and mantle anisotropy: Measurements, interpretations, and new directions. *Surv Geophys* 30:407–461. doi: 10.1007/s10712-009-9075-1
- Long MD, Silver PG (2008) The subduction zone flow field from seismic anisotropy: A global view. *Science* (80-) 319:315–318. doi: 10.1126/science.1150809
- Long MD, Silver PG (2009b) Shear wave splitting and mantle anisotropy: Measurements, interpretations, and new directions. *Surv. Geophys.* 30:407–461
- Long MD, van der Hilst RD (2006) Shear wave splitting from local events beneath the Ryukyu arc: Trench-parallel anisotropy in the mantle wedge. *Phys Earth Planet Inter* 155:300–312. doi: 10.1016/j.pepi.2006.01.003
- Long MD, Wirth EA (2013) Mantle flow in subduction systems: The mantle wedge flow field and implications for wedge processes. *J Geophys Res Solid Earth* 118:583–606 . doi: 10.1002/jgrb.50063
- Louvari EŁ, Kiratzi AA, Papazachos BC (1999) The Cephalonia Transform Fault and its extension to western Lefkada Island (Greece). *Tectonophysics* 308:223–236
- Mainprice D (2007) Seismic Anisotropy of the Deep Earth from a Mineral and Rock Physics Perspective. In: *Treatise on Geophysics*. pp 437–491
- Makris J, Papoulia J, Yegorova T (2013) A 3-D density model of greece constrained by gravity and seismic data. *Geophys J Int*. doi: 10.1093/gji/ggt059
- Makropoulos K, Burton P (1984) Greek Tectonics and Seismicity. *Tectonophysics* 106: 275-304.
- Makropoulos K, Kaviris G, Kouskouna V (2012) An updated and extended earthquake catalogue for Greece and adjacent areas since 1900. *Nat Hazards Earth Syst Sci* 12:1425–1430. doi: 10.5194/nhess-12-1425-2012
- McKenzie D (1972) Active Tectonics of the Mediterranean Region. *Geophys J Int* 30:109–185. doi: 10.1111/j.1365-246X.1972.tb02351.x
- Meijde M Van Der, Lee S Van Der, Giardini D (2003) Crustal structure beneath broad-band seismic

stations in the Mediterranean region. 729–739

- Menant A, Sternai P, Jolivet L, Guillou-Frottier L, Gerya T (2016) 3D numerical modeling of mantle flow, crustal dynamics and magma genesis associated with slab roll-back and tearing: The eastern Mediterranean case. *Earth Planet Sci Lett* 442:93–107. doi: 10.1016/j.epsl.2016.03.002
- Menke W, Levin V (2003) The cross-convolution method for interpreting SKS splitting observations, with application to one and two-layer anisotropic earth models. *Geophys J Int* 154:379–392. doi: 10.1046/j.1365-246X.2003.01937.x
- Moore MM, Garnero EJ, Lay T, Williams Q (2004) Shear wave splitting and waveform complexity for lowermost mantle structures with low-velocity lamellae and transverse isotropy. *J Geophys Res Solid Earth* 109: . doi: 10.1029/2003JB002546
- Müller C, Bayer B, Eckstaller A, Miller H (2008) Mantle flow in the South Sandwich subduction environment from source-side shear wave splitting. *Geophys Res Lett* 35: . doi: 10.1029/2007GL032411
- Müller MD, Geiger A, Kahle HG, Veis G, Billiris H, Paradissis D, Felekis S (2013) Velocity and deformation fields in the North Aegean domain, Greece, and implications for fault kinematics, derived from GPS data 1993–2009. *Tectonophysics* 597–598:34–49. doi: 10.1016/j.tecto.2012.08.003
- Mutlu AK, Karabulut H (2011) Anisotropic Pn tomography of Turkey and adjacent regions. *Geophys J Int* 187:1743–1758. doi: 10.1111/j.1365-246X.2011.05235.x
- Nicolas, A;Christensen NI (1987) Formation of anisotropy in upperman- tle peridotites: a review, in *Composition, Structure and Dynamics of the Lithosphere–Asthenosphere System*. *Am Geophys Union Geo- Dyn Monogr Ser* 16:111–123 . doi: 10.1029/GD016
- Nijholt N, Govers R (2015) The role of passive margins on the evolution of Subduction-Transform Edge Propagators (STEPS). *J Geophys Res Solid Earth* 120:7203–7230. doi: 10.1002/2015JB012202
- Niu F, Perez AM (2004) Seismic anisotropy in the lower mantle: A comparison of waveform splitting of SKS and SKKS. *Geophys Res Lett* 31:1–4. doi: 10.1029/2004GL021196
- Nyst M, Thatcher W (2004) New constraints on the active tectonic deformation of the Aegean. *J Geophys Res Solid Earth* 109:1–23. doi: 10.1029/2003JB002830
- Olive JA, Pearce F, Rondenay S, Behn MD (2014) Pronounced zonation of seismic anisotropy in the Western Hellenic subduction zone and its geodynamic significance. *Earth Planet Sci Lett* 391:100–109. doi: 10.1016/j.epsl.2014.01.029
- Pan S, Niu F (2011) Large contrasts in crustal structure and composition between the Ordos plateau and the NE Tibetan plateau from receiver function analysis. *Earth Planet Sci Lett* 303:291–298. doi: 10.1016/j.epsl.2011.01.007
- Papadimitriou E, Sykes L (2001) Evolution of the stress field in the northern Aegean Sea (Greece). *Geophys. J. Int.* 146: 747–759.
- Papadimitriou E (2002) Mode of strong earthquake recurrence in the central Ionian islands (Greece): Possible triggering due to Coulomb stress changes generated by the occurrence of previous strong shocks. *Bull. Seismol. Soc. Am.*, 92(8): 3293–3308.

- Papadimitriou P, Kaviris G, Makropoulos K (1999) Evidence of shear-wave splitting in the eastern Corinthian Gulf (Greece). *Phys Earth Planet Inter* 114:3–13. doi: 10.1016/S0031-9201(99)00041-2
- Papadimitriou P, Kapetanidis V, Karakonstantis A, Kaviris G, Voulgaris N, Makropoulos K (2015) The Santorini Volcanic Complex: A detailed multi-parameter seismological approach with emphasis on the 2011–2012 unrest period. *J Geodyn* 85: 32–57. doi: 10.1016/j.jog.2014.12.004.
- Papadimitriou P, Kassaras I, Kaviris G, Tselentis G.-A, Voulgaris N, Lekkas E, Chouliaras G, Evangelidis C, Pavlou K, Kapetanidis V, Karakonstantis A, Kazantzidou-Firtinidou D, Fountoulakis I, Millas C, Spingos I, Aspiotis T, Moumoulidou A, Skourtsos E, Antoniou V, Andreadakis E, Mavroulis S, Kleanthi M (2018) The 12 th June 2017 $M_w = 6.3$ Lesvos earthquake from detailed seismological observations. *J. Geodyn.* 115: 23–42. doi: 10.1016/j.jog.2018.01.009
- Papanikolaou D (2009) Timing of tectonic emplacement of the ophiolites and terrane paleogeography in the Hellenides. *Lithos* 108:262–280 . doi: 10.1016/j.lithos.2008.08.003
- Papanikolaou D (2013) Tectonostratigraphic models of the Alpine terranes and subduction history of the Hellenides. *Tectonophysics*. doi: 10.1016/j.tecto.2012.08.008
- Papanikolaou D, Alexandri M, Nomikou P, Ballas D (2002) Morphotectonic structure of the western part of the North Aegean Basin based on swath bathymetry. *Mar Geol* 190:465–492. doi: 10.1016/S0025-3227(02)00359-6
- Papanikolaou DJ, Royden LH (2007) Disruption of the Hellenic arc: Late Miocene extensional detachment faults and steep Pliocene-Quaternary normal faults - Or what happened at Corinth? *Tectonics* 26. doi: 10.1029/2006TC002007
- Papadimitriou P, Kaviris G, Makropoulos K (1999) Evidence of shear-wave splitting in the eastern Corinthian Gulf (Greece). *Phys Earth Planet Inter* 114:3–13. doi: 10.1016/S0031-9201(99)00041-2
- Papazachos BC, Dimitriadis ST, Panagiotopoulos DG, Papazachos CB, Papadimitriou EE (2005) Deep structure and active tectonics of the southern Aegean volcanic arc The South Aegean Active Volcanic Arc: Present Knowledge and Future Perspectives. Elsevier.
- Papazachos BC, Karakostas VG, Papazachos CB, Scordilis EM (2000) The geometry of the Wadati-Benioff zone and lithospheric kinematics in the Hellenic arc. In: *Tectonophysics*. pp 275–300
- Papazachos C, Nolet G (1997) P and S deep velocity structure of the Hellenic area obtained by robust nonlinear inversion of travel times. *J Geophys Res* 102:8349–8367. doi: 10.1029/96JB03730
- Paul A, Karabulut H, Mutlu AK, Salaün G (2014) A comprehensive and densely sampled map of shear-wave azimuthal anisotropy in the Aegean-Anatolia region. *Earth Planet Sci Lett* 389:14–22. doi: 10.1016/j.epsl.2013.12.019
- Phinney RA (1964) Structure of the Earth ' s Crust from Spectral Behavior of Long-Period Body Waves. *J. Geophys. Res.*, 69: 2997—3017.
- Pichon X Le, Angelier J (1979) The hellenic arc and trench system: A key to the neotectonic evolution of the eastern mediterranean area. *Tectonophysics* 60:1–42 . doi: 10.1016/0040-1951(79)90131-8
- Piromallo C, Morelli A (2003) *P* wave tomography of the mantle under the Alpine-Mediterranean

area. *J Geophys Res Solid Earth* 108:1–23. doi: 10.1029/2002JB001757

- Reilinger R, McClusky S, Vernant P, Lawrence S, Ergintav S, Cakmak R, Ozener H, Kadirov F, Guliev I, Stepanyan R, Nadariya M, Hahubia G, Mahmoud S, Sakr K, ArRajehi A, Paradissis D, Al-Aydrus A, Prilepin M, Guseva T, Evren E, Dmitrotsa A, Filikov S V., Gomez F, Al-Ghazzi R, Karam G (2006) GPS constraints on continental deformation in the Africa-Arabia-Eurasia continental collision zone and implications for the dynamics of plate interactions. *J Geophys Res Solid Earth* 111:1–26. doi: 10.1029/2005JB004051
- Restivo A, Helffrich G (1999) Teleseismic shear wave splitting measurements in noisy environments. *Geophys J Int* 137:821–830 . doi: 10.1046/j.1365-246X.1999.00845.x
- Rontogianni S (2010) Comparison of geodetic and seismic strain rates in Greece by using a uniform processing approach to campaign GPS measurements over the interval 1994-2000. *J Geodyn.* doi: 10.1016/j.jog.2010.04.008
- Rosenbaum G, Gasparon M, Lucente FP, Peccerillo A, Miller MS (2008) Kinematics of slab tear faults during subduction segmentation and implications for Italian magmatism. *Tectonics* 27:1–16. doi: 10.1029/2007TC002143
- Roumelioti Z, Kiratzi A, Benetatos C (2011) Time-Domain Moment Tensors for shallow ($h \leq 40$ km) earthquakes in the broader Aegean Sea for the years 2006 and 2007: The database of the Aristotle University of Thessaloniki. *J Geodyn.* doi: 10.1016/j.jog.2010.01.011
- Royden LH, Papanikolaou DJ (2011) Slab segmentation and late Cenozoic disruption of the Hellenic arc. *Geochemistry, Geophys Geosystems* 12:1–24. doi: 10.1029/2010GC003280
- Russo RM, Silver PG (1994) Trench-Parallel Flow Beneath the Nazca Plate from Seismic Anisotropy. *Science* (80-) 263:1105–1111 . doi: 10.1126/science.263.5150.1105
- Sachpazi M, Laigle M, Charalampakis M, Diaz J, Kissling E, Gesret A, Becel A, Flueh E, Miles P, Hirn A (2016) Segmented Hellenic slab rollback driving Aegean deformation and seismicity. *Geophys Res Lett.* doi: 10.1002/2015GL066818
- Salauin G, Pedersen HA, Paul A, Farra V, Karabulut H, Hatzfeld D, Papazachos C, Childs DM, Pequegnat C, Afacan T, Aktar M, Bourova-Flin E, Cambaz D, Hatzidimitriou P, Hubans F, Kementzetzidou D, Karagianni E, Karagianni I, Komec Mutlu A, Dimitrova L, Ozakin Y, Roussel S, Scordilis M, Vamvakaris D (2012) High-resolution surface wave tomography beneath the Aegean-Anatolia region: Constraints on upper-mantle structure. *Geophys J Int* 190:406–420 . doi: 10.1111/j.1365-246X.2012.05483.x
- Savage MK (1999) Seismic anisotropy and mantle deformation: what have we learnt from shear wave splitting? *Rev Geophys* 37:65–106 . doi: 10.1029/98RG02075
- Savage MK (1998) Lower crustal anisotropy or dipping boundaries? Effects on receiver functions and a case study in New Zealand. *J Geophys Res Solid Earth* 103:15069–15087. doi: 10.1029/98JB00795
- Savage MK, Peppin WA, Vetter UR (1990) Shear wave anisotropy and stress direction in and near Long Valley caldera, California, 1979-1988. *J Geophys Res* 95:11,111-165,177. doi: 10.1029/JB095iB07p11165
- Shearer P (1999) *Introduction to Seismology*. Cambridge University Press.
- Schmid C, van der Lee S, Giardini D (2004) Delay times and shear wave splitting in the Mediterranean region. *Geophys J Int* 159:275–290 . doi: 10.1111/j.1365-246X.2004.02381.x

- Şengör AM., Tüysüz O, İmren C, Sakıncı M, Eyidoğan H, Görür N, Le Pichon X, Rangin C (2005) THE NORTH ANATOLIAN FAULT: A NEW LOOK. *Annu Rev Earth Planet Sci* 33:37–112. doi: 10.1146/annurev.earth.32.101802.120415
- Sibson R (1981) A Brief Description of Natural Neighbour Interpolation. In: *Interpreting multivariate data*.
- Silver PG, Chan WW (1991) Shear Wave Splitting and Sub continental Mantle Deformation. *J Geophys Res* 96:429–454 . doi: 10.1029/91JB00899
- Silver PG, Savage MK (1994) The Interpretation of Shear Wave Splitting Parameters In the Presence of Two Anisotropic Layers. *Geophys J Int* 119:949–963 . doi: 10.1111/j.1365-246X.1994.tb04027.x
- Snopek K, Meier T, Endrun B, Bohnhoff M, Casten U (2007) Comparison of gravimetric and seismic constraints on the structure of the Aegean lithosphere in the forearc of the Hellenic subduction zone in the area of Crete. *J Geodyn*. doi: 10.1016/j.jog.2007.03.005
- Sodoudi F, Brüstle A, Meier T, Kind R, Friederich W (2015) Receiver function images of the Hellenic subduction zone and comparison to microseismicity. *Solid Earth*. doi: 10.5194/se-6-135-2015
- Sodoudi F, Kind R, Hatzfeld D, Priestley K, Hanka W, Wylegalla K, Stavrakakis G, Vafidis A, Harjes HP, Bohnhoff M (2006) Lithospheric structure of the Aegean obtained from P and S receiver functions. *J Geophys Res Solid Earth* 111: . doi: 10.1029/2005JB003932
- Song TRA, Kawakatsu H (2013) Subduction of oceanic asthenosphere: A critical appraisal in central Alaska. *Earth Planet Sci Lett* 367:82–94. doi: 10.1016/j.epsl.2013.02.010
- Soto GL, Ni JF, Grand SP, Sandvol E, Valenzuela RW, Speziale MG, González JMG, Reyes TD (2009) Mantle flow in the Rivera-Cocos subduction zone. *Geophys J Int* 179:1004–1012. doi: 10.1111/j.1365-246X.2009.04352.x
- Stein S, Wysession M (2003) *An introduction to Seismology*. Oxford Blackwell Science.
- Stucchi M, Rovida A, Gomez Capera A, Alexandre P, Camelbeeck T, Demircioglu M, Gasperini P, Kouskouna V, Musson R, Radulian M, Sesetyan K, Vilanova S, Baumont D, Bungum H, Fäh D, Lenhardt W, Makropoulos K, Martinez Solares J, Scotti O, Živčić M, Albini P, Batllo J, Papaioannou C, Tatevossian R, Locati M, Meletti C, Viganò D, Giardini D (2013) The SHARE European Earthquake Catalogue (SHEEC) 1000-1899. *J. Seismol.* 17: 523–544. doi: 10.1007/s10950-012-9335-2
- Suckale J, Rondenay S, Sachpazi M, Charalampakis M, Hosa A, Royden LH (2009) High-resolution seismic imaging of the western Hellenic subduction zone using teleseismic scattered waves. *Geophys J Int* 178:775–791 . doi: 10.1111/j.1365-246X.2009.04170.x
- Tommasi A, Mainprice D, Cordier P, Thoraval C, Couvy H (2004) Strain-induced seismic anisotropy of wadsleyite polycrystals and flow patterns in the mantle transition zone. *J Geophys Res Solid Earth* 109:1–10 . doi: 10.1029/2004JB003158
- Tommasi A, Tikoff B, Vauchez A (1999) Upper mantle tectonics: Three-dimensional deformation, olivine crystallographic fabrics and seismic properties. *Earth Planet Sci Lett* 168:173–186. doi: 10.1016/S0012-821X(99)00046-1
- Tselentis GA, Melis N, Sokos E, Beltas P (1997) The winter 1991-1992 Earthquake sequence at Cephalonia island, Western Greece. *Pure and Applied Geophysics* 150(1): 75-89.

- Tzani A, Vallianatos F, Makropoulos K (2000) Seismic and electrical precursors to the 17-1-1983, M7 Kefallinia Earthquake, Greece: Signatures of a SOC system. *Phys. Chem. Earth* 25:281-287.
- Vecsey L, Plomerová J, Babuška V (2008) Shear-wave splitting measurements - Problems and solutions. *Tectonophysics* 462:178–196 . doi: 10.1016/j.tecto.2008.01.021
- Vinnik LP (1977) Detection of waves converted from p to sv in the mantle. *Phys Earth Planet Inter* 15:39–45
- Vinnik LP, Kind R, Korasev GL, Makeyeva LI (1989) Azimuthal anisotropy in the lithosphere from observations of long period S-waves. *Geophys J Int* 99:549–559
- Voulgaris, N., Parcharidis, I., Pahoula, M., Pirlis, E., 2004. Correlation of tectonics, seismicity and geothermics of Lesbos Island using remote sensing data and Geographical Information Systems. *Bull. Geol. Soc. Greece XXXVI*, 938-947.
- Walker KT, Nyblade AA, Klemperer SL, Bokelmann GHR, Owens TJ (2004) On the relationship between extension and anisotropy: Constraints from shear wave splitting across the East African Plateau. *J Geophys Res Solid Earth* 109: . doi: 10.1029/2003JB002866
- Wolfe CJ, Silver PG (1998) Seismic anisotropy of oceanic upper mantle: Shear wave splitting methodologies and observations. *J Geophys Res Solid Earth* 103:749–771. doi: 10.1029/97JB02023
- Wüstefeld A (2007) Methods and applications of Shear Wave Splitting: The east European Craton. Phd
- Wüstefeld A, Bokelmann G (2007) Null detection in shear-wave splitting measurements. *Bull Seismol Soc Am* 97:1204–1211. doi: 10.1785/0120060190
- Wüstefeld A, Bokelmann G, Zaroli C, Barruol G (2008) SplitLab: A shear-wave splitting environment in Matlab. *Comput Geosci* 34:515–528. doi: 10.1016/j.cageo.2007.08.002
- Xu L, Rondenay S, van der Hilst RD (2007) Structure of the crust beneath the southeastern Tibetan Plateau from teleseismic receiver functions. *Phys Earth Planet Inter* 165:176–193. doi: 10.1016/j.pepi.2007.09.002
- Zhang S, Karato S (1995) Lattice preferred orientation of olivine aggregates deformed in simple shear. *Nature* 375:774–777. doi: 10.1038/375774a0
- Zhu L, Kanamori H (2000) Moho depth variation in southern California from teleseismic receiver functions, *J. Geophys Res* 105:2969–2980 . doi: 10.1029/1999JB900322

